Northumbria University
NEWCASTLE

DEVELOPMENT OF AN INTEGRATED PLATFORM FOR PROBE MICROSCOPY-BASED MECHANOBIOLOGY EXPERIMENTS

CHRISTOPHER MARKWELL

PhD

2023

DEVELOPMENT OF AN INTEGRATED PLATFORM FOR PROBE MICROSCOPY-BASED MECHANOBIOLOGY EXPERIMENTS

CHRISTOPHER MARKWELL

A thesis submitted in partial fulfilment of the requirements of the University of Northumbria at Newcastle for the degree of Doctor of Philosophy

Faculty of Engineering and Environment

September 2023

Abstract

Utilising Atomic Force Microscopy to probe the mechanical properties of biological elements is crucial for comprehending cellular microenvironments and gaining deeper insights into surface morphology. This work primarily aims to explore the effects of acousto-mechanical stimulation on dermal fibroblasts by examining proliferation rates and mechanical properties.

Additionally, AFM serves as an important tool for examining the morphology of materials, complementing its use in testing the mechanical properties of cells. This study investigates changes in the morphology of silica-based antiviral surfaces and bacterial cellulose using AFM.

Exploring the effects of acousto-mechanical stimulation on dermal fibroblasts is achieved through experimental investigations using Surface Acoustic Wave (SAW) devices. These devices generate regular periodic waves directed into a chamber containing cells. To accomplish this, four devices are employed, each with S11 frequencies ranging from 9.5MHz to 27MHz. The findings from this study demonstrate an increase in the proliferation of Normal Human Dermal Fibroblasts (NHDF) and an enhancement in cell stiffness, with the maximum proliferation observed across all powers and devices reaching 241% above the control.

After the final stimulation, stiffness values were measured for both the stimulated cells and the control cells, the latter growing under the same circumstances without stimulation. Blunted pyramidal cantilever tips were employed for the atomic force microscopy (AFM)-based measurements. Stimulated cells exhibited increased average effective Youngs' modulus of between 64% and 106% with a broader distribution. The widening distribution in stiffness values indicates the non-uniform effect of acousto-mechanical excitation.

Contents

List of Figures

List of Tables

Abbreviations

AFM	Atomic Force Microscope
BC	Bacterial Cellulose
BSA	Bovine Serum Albumin
BslA	Biofilm-surface layer protein A
CN	Carbon Nanotube
CBM	Carbohydrate Binding Domain
COOH	Carboxylic Acid
DAPI	4',6-diamidino-2-phenylindole
DMT	Derjaguin-Müller-Toporov
DF	Dilution Factor
DNA	Deoxyribonucleic acid
DSMO	Dimethyl Sulfoxide
DMEM	Dulbecco's Modified Eagle Medium
ECM	Extracellular Matrix
FA	Focal Adhesion
FD	Force Displacement
FDM	Fused Deposition Modelling
GUI	Graphical User Interface
IDT	Interdigital Transducer

IF	Immunofluorescence
IgG	Immunoglobulin
InvOLS	Inverted Optical Lever Sensitivity
JKR	Johnson-Kendall-Roberts
NHDF	Normal Human Dermal Fibroblasts
PBS	Phosphate Buffered Saline
PCR	Polymerase chain reaction
PDMS	Polydimethylsiloxane
PEI	Polyethyleneimine
PID	Proportional/Integral/Derivative
PLA	Polylactic acid
PVD	Physical Vapour Deposition
QP	Quadrant Photodiode
RMS	Root mean squared
RNA	Ribonucleic acid
SAW	Surface Acoustic Wave
SEM	Scanning Electron Microscopy
SCOBY	Symbiotic Culture of Bacteria and Yeast
SMFS	Single-Molecule Force Spectroscopy
SSc	Systemic Sclerosis
SWNT	Single-walled nanotubes
TAZ/WWTR1	WW domain-containing transcription regulator also known as TAZ
TGF-β1	Transforming growth factor beta 1
WCA	Water Contact Angle
YAP	Yes Associated Protein 1
ZnO	Zinc Oxide

List of Publications

List of journal papers;

- Dawson, F., Yew, W. C., Orme, B., **Markwell, C.**, Ledesma-Aguilar, R., Perry, J. J., Shortman, I. M., Smith, D., Torun, H., Wells, G., & Unthank, M. G. (2022). Self-Assembled, Hierarchical Structured Surfaces for Applications in (Super)hydrophobic Antiviral Coatings. *Langmuir*. https://doi.org/10.1021/ACS.LANGMUIR.2C01579,
- Zahertar, S., Torun, H., Sun, C., **Markwell , C.**, Dong, Y., Yang, X., & Fu, Y. (2022). Flexible Platform of Acoustofluidics and Metamaterials with Decoupled Resonant Frequencies. *Sensors* 2022, Vol. 22, Page 4344, 22(12), 4344. https://doi.org/10.3390/S22124344
- Gilmour, K. A., Aljannat, M., **Markwell, C.**, James, P., Scott, J., Jiang, Y., Torun, H., Dade-Robertson, M., & Zhang, M. (2023). Biofilm inspired fabrication of functional bacterial cellulose through ex-situ and in-situ approaches. *Carbohydrate Polymers*, 304, 120482. https://doi.org/10.1016/J.CARBPOL.2022.120482

List of conference and Special Interest Group (SIG) meeting presentations;

- Oral Presentation, AFM BioMed Conference 2019, 2^{nd}-6^{th} September, Fürstbischöfliches Schloss Münster, Münster, Germany.
- Oral Presentation, Single-Molecule Sensors and nanoSystems international conference 2020, 9^{th}-11^{th} November 2020, Virtual Conference, Barcelona, Spain.
- Flash Presentation, Acoustofluidics 2021, 25^{th}-27^{th} August 2021, Virtual Conference.

List of book chapters;

- Torun, H., Agrawal, P., **Markwell, C.**, Fu, Y., Todryk, S., & Moschos, S. A. (2023). Engineering Approaches for Cellular Therapeutics and Diagnostics. Emerging Drug Delivery and Biomedical Engineering Technologies, 157–169. https://doi.org/10.1201/9781003224464-10

Acknowledgements

I express my sincere gratitude to my principal supervisor Dr Hamdi Torun for continuous support, patience, and guidance and for encouraging my personal development as a postgraduate researcher as well as the opportunity to study a PhD. In addition to all of my supervision team, Prof. Richard Fu and Prof. Stephen Todryk, without whom, I would haven't been as well-rounded a researcher with skills I never anticipated gaining in my PhD studies.

I am also grateful for the support of other people at Northumbria University who have helped me during my PhD including; Dr Ran Tao who pushed me in completing experiments, Dr. Davina de Camargo Madeira Simoes Vogiatzis for teaching me about tissue culture and a lot of the biological basis for my work, and Dr Steven O'Reilly. Many thanks also to all of the support provided by the technical teams at Northumbria.

I owe my fellow postgraduate students a great deal of gratitude for supporting me personally and professionally in all things, especially when undertaking unfamiliar work, in particular; Jethro Vernon, Gina Elsayed, Sophia Quigley, Nicola Cowely and Luke Haworth.

I am eternally grateful for the support and love my family and girlfriend has shown me throughout my studies, providing the motivation to complete this task and giving me the passion to pursue this subject.

Declaration

I declare that the work contained in this thesis has not been submitted for any other award and that it is all my own work. I also confirm that this work fully acknowledges opinions, ideas and contributions from the work of others.

Any ethical clearance for the research presented in this thesis has been approved. Approval has been sought and granted by the *Faculty Ethics Committee* on *29/08/2019*.

I declare that the Word Count of this thesis is 25,938 words.

Name: Christopher Markwell

Date: 22 September 2023

Chapter 1

Introduction

1.1 Background and challenges

Environmental and external physical factors regulate various bodily functions, from cellular production to organ and tissue function. Among these, mechanical cues and cell responses to them play a crucial role in homeostasis through inter and intra-cellular communication. Cellular responses to mechanical cues lead to the regulated expression of proteins, changes in proliferation rates, and cell differentiation. These processes provide a framework for other cells to reside and control overall tissue stiffness, playing a crucial role in wound healing processes through the remodelling of the extracellular matrix (ECM) and tissue.

Each cell's response to these stimuli regulates various biological processes according to the nature of the applied forces and the cell's inherent programming. In the context of tissue repair, fibroblasts, which exhibit mechanical sensitivity, are pivotal in repairing tissue structure. Fibroblasts play a crucial role in producing matrix components such as collagen-1 in connective tissue to support wound healing (Sorrell and Caplan, 2004) and overall tissue structure (Martin, 1997).

The mechanosensing characteristics of fibroblasts have been extensively studied using various methods, including mechanical stretching (Kuang et al., 2015), fluid shear (Malek et al., 1993), electrical stimulation (Chen et al., 2019), and pressure application (Chang et al., 2008). A convenient method for applying mechanical stimuli involves using a flexible and stretchable substrate on which cells are grown. Typically, large transducers are employed to generate the necessary strain,

limiting their integration into cell incubators for long-term operation.

This study proposes a novel micromachined acoustofluidic platform with an integrated transducer within a sample holder to investigate the effects of mechanical excitation on eukaryotic cells in vitro. The transducer can generate periodic acoustic waves along the substrate's surface, with amplitudes reaching several hundred nanometers and a frequency range spanning tens of kilohertz to several hundreds of megahertz, depending on the transducer's design (Fu et al., 2010).

The transducer employed is a surface acoustic wave (SAW) device, which, upon the application of an alternating current field to the interdigital transducer (IDT) designed on a piezoelectric substrate, generates a mechanical wave propagating across the surface away from the IDTs. This class of devices has been widely studied in sensing applications due to their high sensitivity to various external factors and substrate loading. SAW can also be applied to microfluidics, where mechanical waves interact with liquids to create internal streaming—a mechanism that underlies our acousto-mechanical stimulation of eukaryotic cells.

The platform is designed with a small footprint to operate inside a conventional cell incubator for long-term cell stimulation. We have employed this method to study a case study involving Normal Human Dermal Fibroblasts (NHDF), characterizing their viscoelastic properties and cell proliferation rates.

1.2 Aims and Objectives

The work contained in this thesis aims to develop an integrated platform for probe microscopy-based mechanobiology experiments. This is a

- Develop a platform that integrates AFM and SAW for investigating acousto-mechanical stimulation.
- Investigate the impact of acousto-mechanical stimulation on cellular responses by combining cell counting with AFM.
- Explore the use of AFM for imaging, addressing challenges and characterizing diverse samples.

1.3 Outline of the thesis

This thesis is divided into five chapters;

The first chapter serves as an introduction to the aims and objectives of this research, providing a clear outline of the thesis's scope and the contributions it brings to the field. It delineates the boundaries within which the study operates, introducing the research questions and hypotheses that guide the entire thesis.

The second chapter, delves into a review of current literature, focusing on cell biology, Atomic Force Microscopy (AFM), and Surface Acoustic Waves (SAW). This exploration provides context and equations necessary for the subsequent chapters, shedding light on the principles and research that underpinning this thesis.

The third chapter looks into the use of Atomic Force Microscopy (AFM) for imaging, addressing the challenges it presents and offering strategies for overcoming them. This chapter is dedicated to the characterisation of three distinct sample types: antiviral surfaces, coated bacterial cellulose, and single-walled nanotubes. Furthermore, Chapter Three extends its focus to the application of AFM in imaging eukaryotic cells, providing insights into its potential in studying cellular dynamics. This chapter gives the necessary tools to navigate AFM challenges while deepening our understanding of diverse samples, and practice for the following chapter.

The fourth chapter is dedicated to investigating the effects of acousto-mechanical stimulation on cellular responses. This chapter combines cell counting with Atomic Force Microscopy (AFM), to investigate the subject. Through quantitative cell counting, we gather essential data on cellular proliferation, while AFM offers a view of mechanical changes. This chapter provides an insight into how cells perceive and adapt to external mechanical stimuli.

The fifth chapter presents the conclusion of the research, looking at the key findings and implications. This chapter also offers some suggestions for future research, allowing for expansion of the knowledge contained in this thesis.

Chapter 2

Literature Review

This chapter reviews the current literature relevant to the context of this thesis, providing foundational knowledge and identifying gaps where this research contributes. The literature review begins with an introduction to cell biology, followed by an exploration of Atomic Force Microscopy and its applications in probing cellular mechanics. Lastly, we delve into the literature on Surface Acoustic Waves and their potential as both actuators and sensors in biological contexts.

2.1 Cell biology

2.1.1 Overview

Cells provide a fascinating area of study for most fields of science; they take on many roles, even with some cells taking on specialities within the whole.

The cells' roles are undertaken at many scales, with the molecular machines operating within the cell to maintain the cell, the cells operating within the broader tissue to maintain that tissue and then the tissues functioning to maintain the organism within which they are contained.

It is easy to observe the functions of tissues within an organism and determine their intended function. However, challenges exist when breaking this down into constituent parts to observe the individual roles that specialised cells play within those tissues because most cells require observation with microscopes.

Further, seeing the constituent components of cells requires another level of complexity, often by

using florescent molecular markers to allow observations of the locations of proteins within the cell, with the vast majority of eukaryotic cells containing both cytoplasm and a nucleus. Localisation of proteins can be achieved through various methods; the two most common ones are using confocal microscopy and western blotting, where quantification of proteins can be obtained.

Cells are seemingly infinitely adaptable to whatever conditions are imposed upon them by external factors with solutions to problems. Many extraordinary abilities are exhibited by cells with different responses to each one of them they can detect.

2.1.2 Fibroblasts

Fibroblasts are the primary focus of the work contained in this thesis. Fibroblasts are the most common cell type found within connective tissues throughout the body. It is well-known for its production of the Extracellular Matrix (ECM) and connector proteins of these connective tissues (Kendall and Feghali-Bostwick, 2014).

The production of ECM is especially crucial in wound healing, where fibroblasts will occupy space in the wound post-wound inflammation, proliferate and create the ECM proteins, including Collagen I-IV, XVIII. Collagen provides a scaffold for the replacement of the appropriate cell types in the remodelling phase of wound healing (Reinke and Sorg, 2012; Bainbridge, 2013).

2.1.3 Mechanosensing

Cells respond to various environmental and external physical factors that regulate functions within the body, from cellular production, organ function, tissue function and cell apoptosis. The most common form of cell stimuli is through various chemical factors, where receptors on the exterior of the cell can be activated through various chemical inputs such as G-protein-coupled receptors and cytokines. Chemical or protein inputs can also be mediated through the transportation of molecules through the cell membrane.

Various sources in the body can apply forces on cells and tissues from the extension/contraction of muscle tissue and increased localised pressure from blood, resulting in the stretching of artery walls, among many others. These mechanical cues and the responses of cells to these play a crucial role in homeostasis through inter- and intra-cellular communication.

Integrins are a mechanism by which cells can sense and transmit intracellular forces, extracellular forces, and contractile forces generated by myosin motor proteins. These forces then activate various signalling pathways, which mediate the cell's response (Schwartz, 2010).

The Hippo pathway is an intracellular signalling pathway using the transcriptional regulators Yes-associated protein 1 and TAZ (known also as WWTR1). These transcriptional regulators can bind to several transcription factors, which then act to convert or transcribe Deoxyribonucleic acid (DNA) into RNA. The generated Ribonucleic acid (RNA) can then be read and increased protein content produced. YAP/TAZ signalling is activated by multiple cues, including TGF-β (Miranda et al., 2017) and tissue stiffening.

Each cell's function in response to these stimuli regulates various biological processes according to the nature of the forces applied according to the cell's 'programming'. The responses of the cell to mechanical cues lead to regulated expression of proteins, changes in proliferation rates and cell differentiation. These provide a framework for other cells to reside and control overall tissue stiffness, which is crucial in wound healing through remodelling the extracellular matrix (ECM) and tissue. Specifically, in the case of tissue repair, one of the significant proponents of repairing tissue structure are fibroblasts which show mechanical sensitivity. Fibroblasts play a crucial role in producing matrix components such as collagen-I in connective tissue to support wound healing (Sorrell and Caplan, 2004) and overall tissue structure (Martin, 1997).

The mechanosensing characteristics of fibroblasts are well studied using various methods such as mechanical stretching (Kuang et al., 2015), applying fluid shear (Malek et al., 1993), electrical (Chen et al., 2019) and pressure (Chang et al., 2008). A convenient method for applying mechanical stimuli is using a flexible and stretchable substrate on which the cells are grown. The substrate is usually stretched and deformed controllably to apply mechanical strain on the cells; the forces applied are detected through the focal adhesion (FA) points and translated into chemical responses through integrin-related signalling (Mohammed et al., 2019).

2.1.4 Bacterial cellulose

Cellulose is a structural polysaccharide consisting of a linear chain of d-glucose molecules, typically found in the cell walls of plants. In these plant walls, the cellulose fibres are cross-linked by other polysaccharides and lignin found within the cell wall's matrix.

Cellulose provides a crucial structural component of many elements in the environment, namely found in the cell walls of plants, with cellulose being used as a fuel source, building materials and clothing; plants such as cotton containing up to 90% (Hsieh, 2007) cellulose and wood containing around 45% (Rowell et al., 2012) among many others.

It has been found that some species of bacteria can generate cellulose to form biofilms; this bacterial cellulose was first described by Brown (1886) when investigating the fermentation of acetic acid with the mother of vinegar pellicule consisting of bacteria-derived cellulose. In work by Brown (1886), the pellicule is described as varying in thickness from an invisible film to that of stout paper.

A famous example of bacteria-secreted cellulose is in the formation of the symbiotic culture of bacteria and yeast (SCOBY), which is used in the creation of kombucha tea (Laavanya et al., 2021). An example of consumption of bacteria derived cellulose is found in *Nata de coco* (translated from the Spanish as cream of coconut), which is created via the fermentation of coconut water using the bacterium *Komagataeibacter xylinus* creates a translucent foodstuff (Budhiono et al., 1999).

Bacteria-secreted cellulose has a multitude of different advantages when compared to its plant-based counterpart. Typically BC has a finer structure with smaller fibres ($\sim$100nm in diameter), higher surface area, increased water absorption (100+ times its weight) and better mechanical strength (15-18 GPa) (Chawla et al., 2009; Gorgieva and Trček, 2019). The work by Xiang et al. (2017) has used the increased mechanical strength of bacterial cellulose to enhance the tensile index of paper sheets with a 5 to 25% increase in the tensile index at low concentrations of additional BC with higher concentrations yielding a 40% increase in tensile index.

Bacterial cellulose has been explored as a potential bio-scaffold for tissue regeneration (Meng et al., 2019). In work by Cherng et al. (2021), BC scaffolds were used on full-thickness wounds in rats; full-thickness wounds consist of a cut which extends into the subcutaneous tissue below both the epidermis and the dermis. The scaffolds showed *in vivo* compatibility, promoting keratinocyte differentiation and aiding in the repair of the epidermis of the skin.

BC provides an excellent platform for functionalising other molecules onto its surface, and this can be used to significant effect in increasing bio-compatibility and adjusting surface properties. This can be achieved because of the significant number of available hydroxyl groups located on

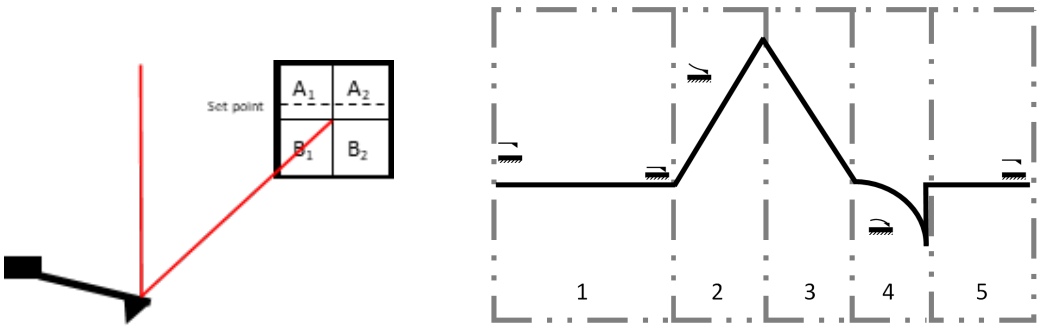

(a) (b)

Figure 2.1: a) Schematic showing deflection on a cantilever and its subsequent measurement on a quadrant photodiode. There are three key parameters; The vertical deflection (vertical deflection $= A_1 + A_2 - B_1 - B_2$), the horizontal deflection (horizontal deflection $= A_1 + B_1 - A_2 - B_2$) and the set point. b) Schematic of a force curve with specific binding and orientation of cantilever of different stages split into different regions.

the surface of the BC; this helps in water retention, as mentioned previously but also as a potential place to attach molecules (Liebner et al., 2016).

BC is very hydrophilic, which results in a low water contact angle (WCA) of approximately 30° (Da Silva et al., 2015). BC's hydrophilic nature is helpful when used as a bio-scaffold in wound healing or as a foodstuff such as *nata de coco*. The hydrophilic properties limit uses in further applications where water absorption is not required but retaining the mechanical properties of BC proves helpful. In order to overcome these shortcomings of BC, the BC surface can be functionalised or otherwise altered to increase its hydrophobicity.

In work by Krishnamurthy et al. (2020), the WCA was increased from 34.5° to 102.1°, taking the BC from being on a macroscopic level from hydrophilic (WCA<90°) into a hydrophobic (WCA>90°) surface. The method utilised to create such a significant change in water contact angle involved a large variety of different chemical processes.

2.2 AFM based-microrheology

2.2.1 AFM theory

Atomic force microscopy (AFM) is an incredibly versatile platform with applications in most physical sciences. AFM was built on the back of the scanning tunnelling microscope (Binnig et al., 1986) which used a tunnelling current requiring the sample to be conductive. In contrast,

AFM uses the atomic interactions between the tip of the cantilever and the sample under investigation.

Figure 2.1a shows how this is achieved; a laser beam is directed to the tip of the cantilever, which deflects the laser beam onto a quadrant photodiode (QP). The location of the laser spot can then be converted into force through careful calibration of the system by measuring the deflection sensitivity and the cantilever's spring constant using a simple hookian spring model (2.1).

$$F = kSV \tag{2.1}$$

Where F is the force (N), k is the spring constant of the cantilever (N/m), S is the measured deflection sensitivity (m/V), and V is the voltage measured on the QP (V). Figure 2.2a, shows the predominant geometries of cantilevers, with most cantilevers consisting of either a triangular or a rectangle geometry.

Using this deflection conversion to force, measurements of some material properties become a matter of actuating a cantilever against a surface and measuring the deflection. In a simple force-spectroscopy experiment (Figure 2.1b), The cantilever first approaches the surface (Region 1); upon adhesive contact with the surface, the cantilever presses into the surface (Region 2), the cantilever then retracts from the surface (Region 3); however, the cantilever bends down due to attractive forces arising (Region 4) from the tip-sample interaction once this adhesive force is broken then the cantilever moves away from the surface and back to the zero deflection line (Region 5). Various parameters can be controlled through the measurement of the tip-sample interaction, which can be used to set up the system into different measurement modes for imaging surface topology; contact (DC) and non-contact (AC) modes. These modes can then provide further details about the surface, examples of these are: Magnetic Force Microscopy (AFM-MFM) (Hartmann, 1999), Electric Force Microscopy (AFM-EFM) (Xu and Arnsdorf, 1995), Conductive AFM (C-AFM) (Murrell et al., 1998), Lateral Force Microscopy (AFM-LFM) among others.

In contact mode, the tip is brought into constant physical contact, where a PID/PI/PD controller is then used to maintain a constant force on the surface by measuring the deflection of the cantilever and used to measure the topography of the sample (Figure 2.3a shows an example of a contact mode image). The constant force on the surface can be set using the set point (shown in Figure

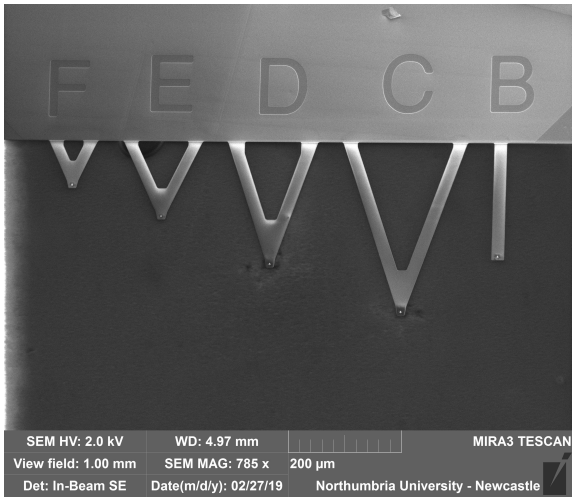

(a)

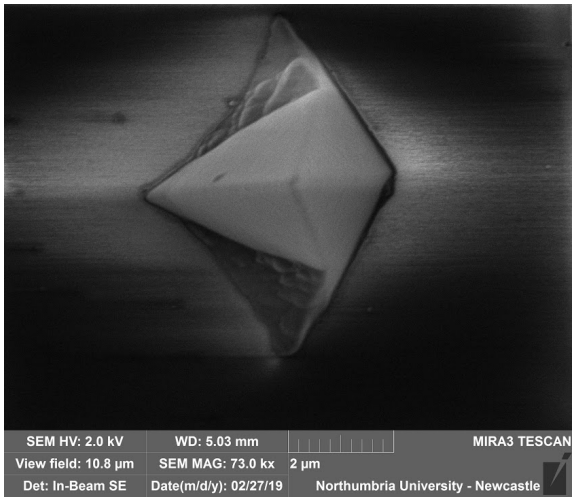

(b)

Figure 2.2: a) SEM image of a MLCT (Bruker) cantilever chip showing five cantilevers (Labelled F to B from left to right) with a variety of lengths and the two predominant geometries of AFM cantilevers b) Close-up SEM image of the tip of a cantilever B from figure 2.2a taken looking down on the tip.

2.1a). The PID controller takes the form of;

$$Z_v = \underline{P} \times Z_{\text{error}} + \underline{I} \times \int Z_{\text{error}}(t)dt + \underline{D}\frac{dZ_{\text{error}}}{dt} \tag{2.2}$$

Where $\underline{P}$, $\underline{I}$, $\underline{D}$ are the gains for Proportional, Integral and Derivative gains respectively. Z_v is the voltage applied to the piezoelectric actuator, and Z_{error}. is the error between the set point and the detected deflection of the cantilever or the amplitude of the cantilever in contact or intermittent

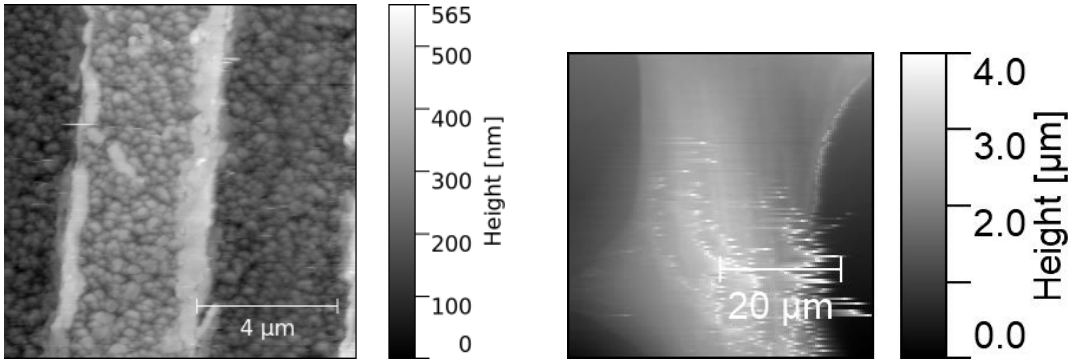

(a) (b)

Figure 2.3: a) Contact mode image of ZnO/Al SAW substrate (10μm by 10μm) b) Tapping mode image of a Normal Human Dermal Fibroblast using AFM (50μm by 50μm).

contact mode respectively.

$$Z_{\text{error}} = \text{Set Point} - \text{Vertical Deflection/Amplitude} \tag{2.3}$$

The piezoelectric voltage Z_v is then applied to the piezo, which will either contract or expand depending on the value of Z_v. The feedback value is defined as;

Where the user defines the set point, in tapping mode, the set point is the cantilever's oscillation amplitude. However, in contact mode, this is the vertical deflection of the cantilever, which can be adjusted to increase or decrease the force on the sample.

Contact mode proves primarily suitable for imaging hard samples where the sample can withstand lateral forces without damage. A contact scan could easily damage softer materials like those found in biology. An intermittent contact or tapping mode which minimises tip-sample forces can be used to overcome this limitation (Hansma et al., 1994). For tapping mode operation, the cantilever is driven at or near its resonant frequency with its oscillation amplitude measured with the PID/PI/PD controller used to maintain a constant cantilever oscillation (Figure 2.3b, shows an example of a tapping mode image of a NHDF cell).

Various quantifiable values can be extracted from the topographic scans. One of these quantities is the RMS roughness of the sample. The RMS roughness is defined as;

$$\text{RMS Roughness} = \sqrt{\frac{1}{n}\sum_{i=1}^{n} y_i^2} \tag{2.4}$$

Where n is the number of samples, i is the iterative portion of the summation and y_i is the value of the sample at a given index of y.

Varying the length of the cantilever can allow for variations in both the stiffness and resonant frequency, allowing for the cantilever to be engineered to suit a variety of different applications, with the frequency-length relationship being governed by;

$$f = \frac{K_n}{2\pi}\sqrt{\frac{EI}{wL^4}} \tag{2.5}$$

Where f is the resonant frequency of the cantilever, K_n is the mode of vibration,E is Young's modulus, I is the moment of inertia, w is the width of the beam, and L is the beam length; therefore, the cantilever's resonant frequency is proportional to the inverse square of the length of the cantilever. An advantage of this operation mode is characterising the material's properties whilst obtaining a topographic map by utilising the difference in the phase of the driving oscillation signal and that of the return.

Measurements using an AFM system can also be undertaken in liquid as well as in air. This ability to undertake experiments *in vitro* allows for a variety of molecular and biological experiments, including; microrheology (Wu et al., 2018), single-molecule force spectroscopy (SMFS), single cell force microscopy (Noy, 2011; Hughes and Dougan, 2016), among others.

2.2.2 Challenges in obtaining AFM measurements

Several challenges exist in the effective use of AFM for any of these applications; as an AFM system deals with the nanoscale and respective forces are equally small; meaning that typically effects without a significant role in an experiment when we consider bulk effects such as Brownian motion or the quantised nature of light to be continuous distributions. These effects start to affect the sensitivity and operation at the nanoscale. These challenges can be characterised into three main categories, with a further challenge applying to stochastic experiments that often arise with biological tests; drift, noise, dynamics and data throughput.

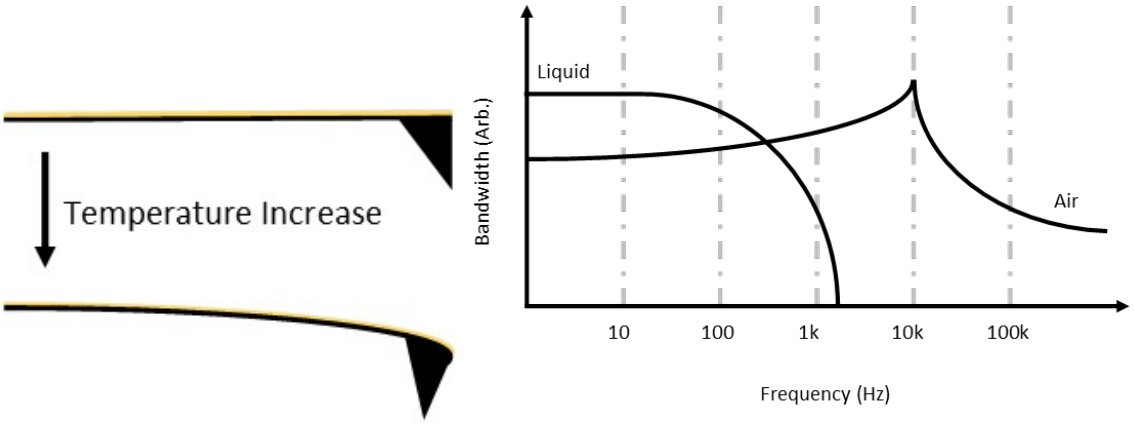

(a) (b)

Figure 2.4: a) Schematic showing the two-layer design of a cantilever and bending as a consequence of mismatched thermal expansion coefficients with temperature change not to scale. b) Example graph showing bandwidth in both air and liquid. Liquid operation shows a significant decrease in operational frequency.

Drift can arise from two main origins; mechanical and thermal. Mechanical noise can be mitigated through isolation of the system from the majority of external factors such as acoustic and mechanical vibrations, using appropriate hardware to control and mitigate. Most AFM cantilevers are of a dual-layer design, with typically a Silicon/Silicon Nitride (Si/Si_3N_4) layer with a reflective Gold/Aluminium (Au/Al) layer. This gives rise to bending as a consequence of a temperature change. Figure 2.4a schematically shows this effect; the gold layer has a higher coefficient of thermal expansion than that of the Si/Si_3N_4 layer, so as the temperature increases, the gold layer expands more than the bottom layer, the effect is a deflecting artefact on the sensor as the tip bends down. Ratcliff et al. (1998), used the photothermal effect to excite cantilevers with an amplitude of between 8-20nm when utalising a 2mW laser. This effect, however, can be mitigated through either design of the cantilever where only the tip is coated with a reflective surface or by allowing the system to come into equilibrium with the environment before measurements are taken.

Figure 2.4b shows a schematic outlining the frequency-bandwidth responses of a hypothetical cantilever with a resonant frequency of $\sim$10kHz in both air and liquid; it can be seen that as the frequency applied to the cantilever increases, the bandwidth in liquid decreases. The hydrodynamic drag on the cantilever causes this whilst it is actuated; the amount of drag experienced is related to the design of the cantilever. Cantilevers with a greater surface area experience a greater drag force. The drag force (F_d) can be characterised by the following equation (Janovjak et al.,

2004);

$$F_d = \frac{6\pi\nu a_{\text{eff}}^2}{h + d_{\text{eff}}} \cdot v_{\text{ip}} \tag{2.6}$$

Where ν is the viscosity of the fluid, h is the tip-surface separation and v_{ip} is the tip velocity. The coefficients a_{eff} and d_{eff} represent the empirical effective size of the cantilever and the tip height, respectively. This equation is only valid in purely viscous flow only. With the drag force being proportional to the square of the effective size of the cantilever, it can be concluded that minimisation of the cantilever size can reduce the drag force, which also increases its resonant frequency (See equation 2.5 and related discussion).

Other forms of mitigation for the issue of hydrodynamic drag can be achieved by using a long AFM tip with the cantilever being out of the liquid with the probe extending into the liquid, which maintains the resonant nodes of the cantilever, thus allowing for improved non-contact imaging in liquid (Guan et al., 2017).

2.2.3 Mechanobiology

Mechanobiology deals with the study of the roles physical factors play in the process of mechanotransduction.

Rheology studies the flow of matter, typically in a non-Newtonian regime, with microrheology dealing with the study of flow on the microscopic scale. Materials and cells which are viscoelastic follow a damped spring model when compressed; the elastic properties of the cell act as the spring, with the viscous medium in the cell acting as a dampener. Figure 2.5c shows an example of a force curve which probes a viscoelastic material; viscous dampening is observed when region C isn't a mirror image of the region B but rather the region C typically has a sharper drop-off upon the start of the retraction portion.

Microrheology can be used to probe the differences between healthy and diseased cells; stiffnesses of either the cells or the extracellular matrix can be critical indicators of disease. Typically, cancerous cells have a lower stiffness than healthy cells, so it is possible to sort healthy from cancerous cells using AFM (Cross et al., 2007; Alibert et al., 2017). Additionally, this can be applied to look at the responses of metastatic cancer cells (Cross et al., 2008). The Young's modulus of the cell is one key marker to show whether a cell has become cancerous.

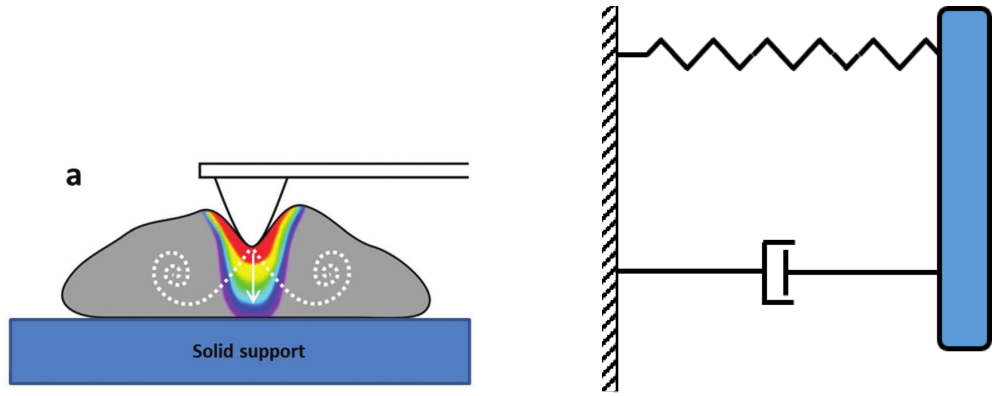

(a)

(b)

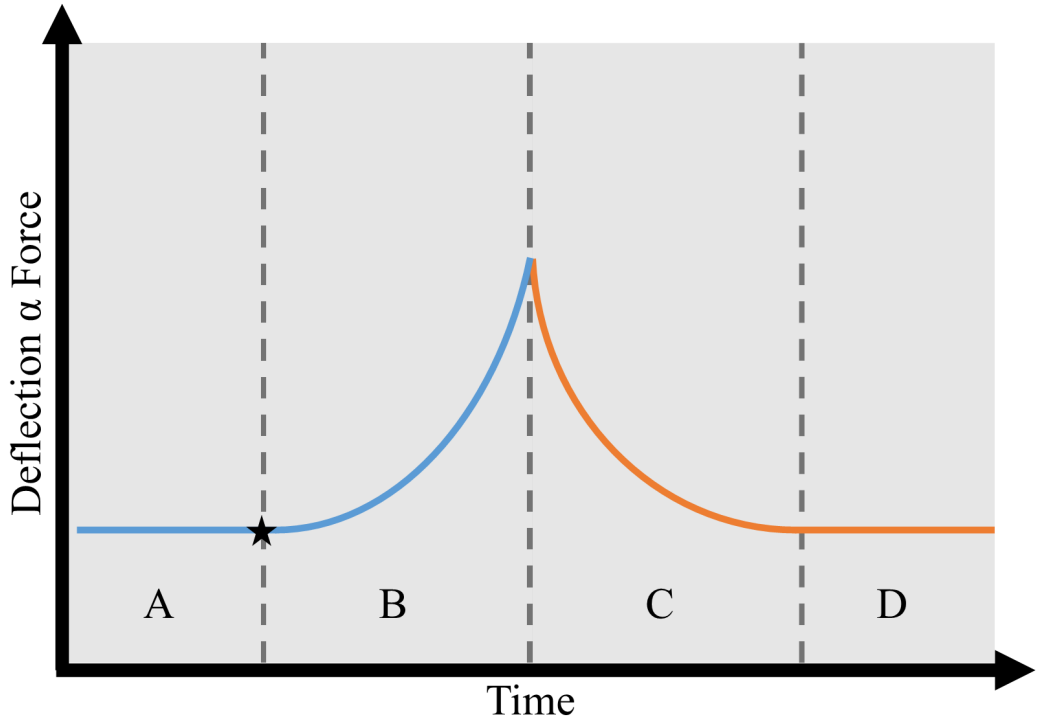

(c)

Figure 2.5: a) Scheme of an AFM probe indenting upon a cell adapted from (Garcia and Garcia, 2018), b) Schematic of a dampened spring system from the Kelvin-Voight model, which shows a spring in parallel to a dampener. c) Schematic of a typical deflection/time graph split into the four different regions; A) Approach to the cell, B) Contact and indentation of the cell from the point marked by $\star$ until the maximum point, C) Retraction whilst still in contact, D) Retraction from the cell and no longer in contact

Cancerous cells also exhibit the ability to undertake changes in their stiffness according to their surroundings, Gil-Redondo et al. (2022), has shown that MCF-7 breast cancer cells can alter their stiffness when seeded on substrates of differing stiffnesses; this aids in the spread of cancer cells. This ductility proves very useful to the spread of cancer as it allows for cancer cells to metasta-

sise as cancer cells have been shown to soften when navigating confined spaces whilst excluding Yes-associated Protein (YAP) from the nucleus (Rianna et al., 2020) which proves crucial for circulating tumour cells to enter the bloodstream.

Another key marker of diseases lies within the Extracellular Matrix. Systemic Sclerosis (SSc) is a disease caused by an excess cross-linking of collagen and causes patients afflicted by this pain from stiffer skin in addition to compromising organ function. In work by Strange et al. (2017), AFM was used to study the stiffness of skin collagen using AFM in patients afflicted by SSc and compared this to healthy patients. It was observed that the stiffness of SSc collagen was higher than that of healthy skin collagen.

The choice of the cantilever for indentation experiments is crucial because if the cantilever is stiffer than the sample, then the deflection is minimal. The measurement becomes insensitive, although it can easily damage the sample by applying large forces, whereas too soft cantilevers do not deform the sample well enough. Then the fitting model cannot be used (Krieg et al., 2018).

Analysis of Force-displacement (FD) curves can be achieved by careful selection and application of an appropriate model, each of which makes a variety of different assumptions and exclusions from their models; either a Hertzian (Hertz, 1896), Derjaguin-Müller-Toporov (DMT) (Derjaguin et al., 1975), or the Johnson-Kendall-Roberts (JKR) model (Johnson et al., 1971). Each of these was developed as a model to describe a spherical indenter contacting a flat surface; however, when considering real surfaces, the surface is rarely truly flat. Additionally, the models assume that the contact of the cantilever is directly perpendicular to the surface, and often cantilevers are tilted with respect to the surface ($\sim 10^{\circ}$), resulting in a non-perpendicular force during indentation.

To effectively analyse the FD curves generated through the experiments, the chosen model is crucial. The Hertzian contact model is used on the extension portion of the FD curve, where adhesive/repulsive contact is negligible. The Hertzian contact model makes several assumptions about the contact between the sample and the cantilever tip that no adhesive or frictional forces are acting between the two bodies when the cantilever is put into contact and is pressed into the body perpendicularly.

The Hertzian contact model can be used for the indentation portion of the experiment; other models need to be considered for the retraction portion where the adhesive contact of the cantilever to

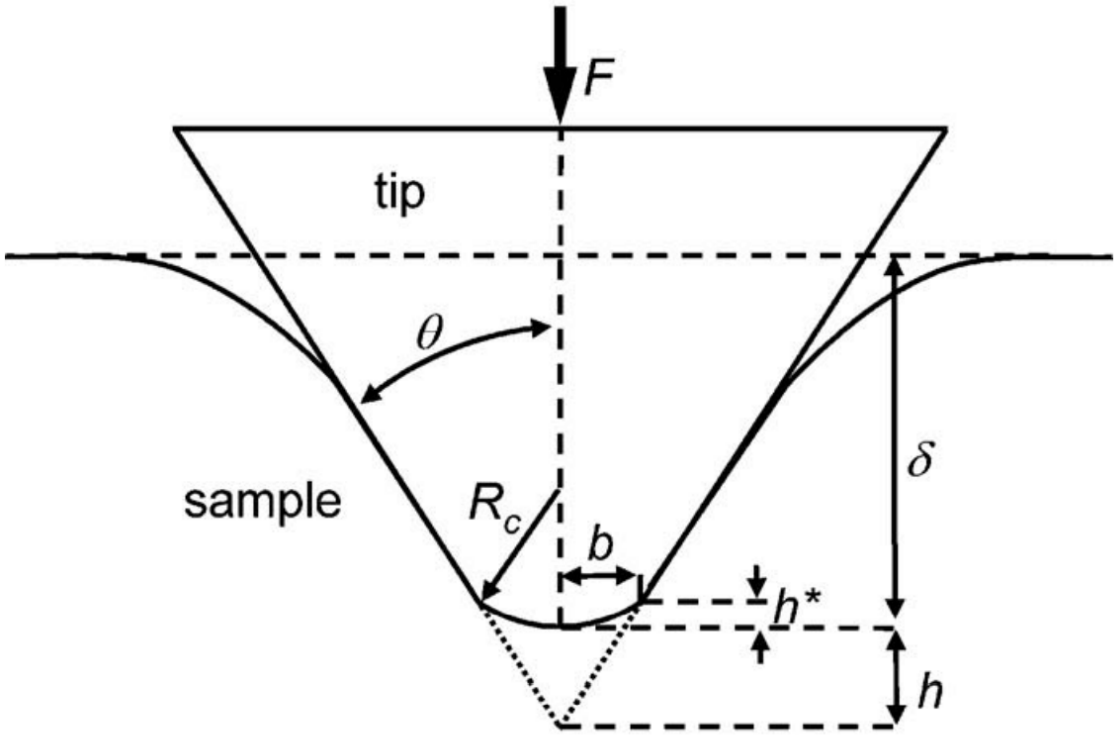

Figure 2.6: Section of the blunted pyramidal AFM tip indenting upon an elastic material to a depth of δ with an applied force F. The tip is modelled by its semi-included angle θ, tip defect h, and spherical cap radius R_c, b is the radial distance corresponding to the transition from the spherical cap to the pyramid's face. Figure adapted from (Rico et al., 2005).

the cell being probed is more significant than where the JKR model could be used. The JKR model is an extension of the Hertzian contact model, expanding upon the model by considering the attraction forces that arise due to adhesive effects, which for AFM-based measurements can include van der Waals effects, or by capillary or liquid-bridge farces. This model is valid for compliant materials indented upon by large colloidal probes and where strong adhesion is present.

The DMT contact model is similar to the JKR but considers longer-range surface forces outside the region of contact with the surface. This model is valid for stiffer materials indented by small spheres with weak adhesion.

For the work contained in this thesis, the Hertz model is chosen. The equation for a spherical/colloidal probe is given by (Krieg et al., 2018);

$$F = E_{\text{eff}} \left[(a^2 + R_p^2) \cdot \ln \left(\frac{R_p + a}{R_p - a} \right) - 2aR_p \right] \tag{2.7}$$

Where E_{eff} is the effective Young's modulus, a is the contact radius and R_p is the radius of the probe. With the indentation depth given by;

$$\delta = \frac{a}{2} \ln \frac{R_p + a}{R_p - a} \tag{2.8}$$

The radius R_p can be determined using SEM imaging for non-colloidal probes; despite the probe manufacturer having this on the specification sheet, this is often inaccurate due to manufacturing differences from wafer to wafer. This model can be further expanded to account for different geometries (Krieg et al., 2018), such as the blunted pyramidal model used for data analysis in this thesis.

In the work by Rico et al. (2005), the Hertz model is extended into a model for blunted pyramidal tips; this is achieved by approximating the pyramidal tip as a blunt tip with a spherical cap. The geometry of this approximation is found in figure 2.6. The equation relating the force exerted on the sample and the indentation provided by the cantilever is given by;

$$F(\delta) = \frac{1}{\sqrt{2}} \frac{E_{\text{eff}} \tan\theta}{(1 - \nu^2)} \delta^2 \tag{2.9}$$

Where F(N) is the measured force from the cantilever (Equation 2.1), E_{eff} (Pa) is the effective Youngs modulus of the sample being measured, θ (°) is the face angle (FA) of the indenting probe, ν is the Poisson's ratio of the sample under investigation and δ (m) is indentation. Poisson's ratio is defined as the deformation of a material perpendicular to the force applied. The indentation is defined as;

$$\delta = Z_{\text{Piezo}} - \frac{F}{k} \tag{2.10}$$

2.3 Surface Acoustic Waves

2.3.1 Introduction

Surface Acoustic Waves (SAW) were first investigated by Rayleigh (1885); this work focused on the behaviour of waves on an infinitely deep elastic material with the wave travelling near the material's surface. The wave amplitude is assumed to decrease exponentially as a function of the distance of the surface.

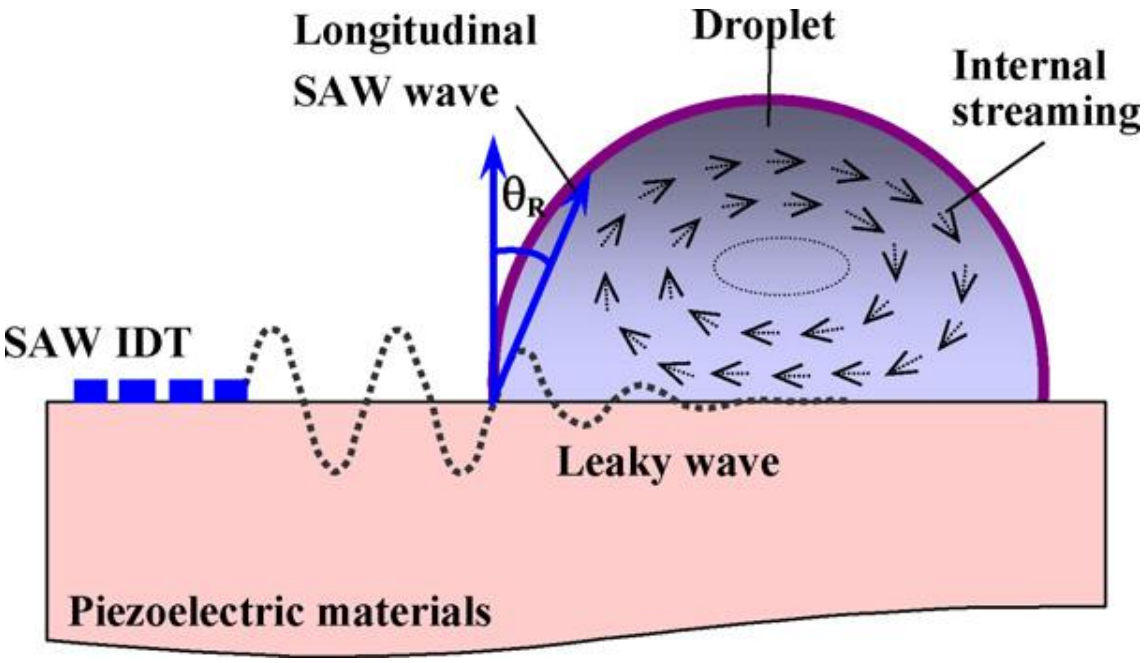

Figure 2.7: Interaction between a Surface Acoustic Wave and a droplet. The SAW causing internal streaming inside the droplet (Taken from (Fu et al., 2010))

Different modalities of acoustic waves exist, such as bulk acoustic waves and lamb waves, which occur if the wavelength is smaller or near the thickness of the substrate on which the wave is travelling; most SAW devices are based upon the Rayleigh wave with the devices used in this thesis using the Rayleigh wave mode.

SAW devices utilise the piezoelectric effect. Piezoelectric materials produce an electric field whenever they undergo mechanical stress; conversely, a piezoelectric material can experience a reverse effect where an electric field is applied, and consequentially, an expansion or contraction of the material occurs. Surface acoustic waves can explain the reverse effect waves to undertake liquid handling operations. The piezoelectric effect is helpful for various applications outside SAW and includes being a significant component of Atomic Force Microscopy, as previously discussed.

Interdigital transducers (IDTs) can generate surface acoustic waves. They are located on the SAW device's piezoelectric surface. The geometry of the IDT and positioning of the IDT(s) can alter the properties of the SAW; the distance between the fingers of the IDT changes the frequency/period of the generated SAW . The fundamental frequency (f_r) is defined as (Fu et al., 2017);

$$f_r = \frac{v_s}{\lambda} \tag{2.11}$$

Where v_s is the speed of sound in the substrate and λ is the wavelength of the generated SAW.

Temperature can alter the IDT spacing through the expansion/contraction of the device. When the temperature rises, the IDT spacing increases, hence the wavelength resulting in a decrease in the fundamental frequency of the SAW device. The reduction in the fundamental frequency is counteracted by the increase in the speed of sound in the substrate; however, the increase in the IDT spacing is the dominant mechanism and still results in a net decrease.

Combining multiple pairs of IDTs allows for the generation of waves of greater complexity; two IDTs of similar or the same design at opposite ends of a SAW device can create standing surface acoustic waves (Shi et al., 2009). Combining two IDTs with a further two IDT pairing perpendicular to the first set allows for a square region where surface acoustic waves can propagate in any direction.

The work by Vernon et al. (2022) shows that using a SAW device with sets of perpendicular IDTs it possible to manipulate and move droplets in a 2D plane, providing a convenient way to mix droplets.

The mechanism for droplet manipulation is driven by the interaction of a SAW and a droplet on a surface or superstrate placed on the surface of the SAW device. Figure 2.7 shows a SAW interacting with a droplet; when the SAW interacts with the droplet, it creates internal streaming. The energy and momentum of the acoustic wave become coupled into the fluid at the Rayleigh angle (θ_R). The Rayleigh angle is defined through the relationship between the speed of sound in the liquid being coupled and the speed of sound in the substrate. When these speeds are mismatched, then the wave diffracts into the liquid, giving the Rayleigh angle as defined by the equation;

$$\theta_R = \arcsin\left(\frac{v_s}{v_l}\right) \tag{2.12}$$

Where v_l and v_s are the speed of sound in the liquid and substrate, respectively (Wixforth, 2003).

By varying the power put into the SAW device, different behaviours of the droplet can be created; this can, as previously discussed, cause internal streaming inside the droplet, which is helpful

in mixing processes, droplet movement (Vernon et al., 2022) and droplet jetting (Biroun et al., 2020*a*).

SAW can enhance fluid handling operations by having two IDTs opposite each other with similar properties, which allow for constructive and destructive interference meaning the droplet can remain stationary but allows for nodes and antinodes to form, allowing for effective particle sorting or cell patterning (Shi et al., 2009; Collins et al., 2015).

2.3.2 Application of SAW for in biology

SAW has many applications inside and outside biology as they are or can be made sensitive to various physical, chemical or electrical (Fu et al., 2010). It provides a versatile platform for sensing. Examples of this include: breath sensing (Vernon et al., 2021), temperature changes (Reindl et al., 2003), and mass loading.

The ability to utilise SAW for a variety of liquid handling operations (Vernon et al., 2022) makes it versatile for creating lab-on-chip devices with potential applications in; Polymerase chain reaction (PCR) (Guttenberg et al., 2005), bacteria detection (Kordas et al., 2016), cell sorting (Ding et al., 2012; Maramizonouz et al., 2022), cell lysis of both eukaryotic and prokaryotic cells (Salehi-Reyhani et al., 2015; Lyford et al., 2012), detection of sexually-transmitted infections (Xu et al., 2015).

In work by Agostini and Collins (2018), surface acoustic waves acousto-mechanically stimulated the monocyte U-937 cell line. They showed that the application of SAW-induced streaming didn't contribute to cell death or changes in cell morphology; however, proliferation increased by approximately 36%.

The cytotoxic response of natural killer cells in response to acousto-mechanical streaming has been studied by Kim et al. (2022). They showed that the shear stress from the acousto-streaming from SAW of the surrounding culture media didn't damage the cells. However, it increased intercellular Ca^{2+} concentrations. When SAW was combined with treating the cells with a protein kinase C activator, it enhanced the lysosomal protein expressions of the natural killer cells; these outcomes from the cells assisted in the cell-mediated cytotoxicity against targetted tumour cells.

2.4 Summary

This chapter presented an overview of the existing literature surrounding Atomic Force Microscopy (AFM) and Surface Acoustic Wave (SAW) technologies and their potential for applications with cells to probe the impact of acousto-mechanical stimulation. Based upon the literature review, the following gaps are identified.

Most of the methods presently employed for studying mechanosensing in cells involve large-scale transducers. Consequently, a gap exists where a smaller platform could be utilized for prolonged *in vitro* cell stimulation studies.

Furthermore, the investigation of structural modifications in functionalized bacterial cellulose, achieved through the incorporation of hydrophobic proteins to enhance its surface characteristics, will be explored in the next chapter. This exploration will also include the examination of other samples, showcasing the utility of AFM for characterizing biomaterials.

Chapter 3

AFM as a platform for characterisation of biomaterials

3.1 Introduction

Observations using traditional microscopy methods are typically by the wavelength of the incident particle, whether this is a photon in the case of light microscopy or an electron in scanning electron microscopy. However, in AFM, these limitations are avoided using a contact or non-contact probe-based methodology, with the maximum lateral resolution limited by the tip radii whilst having higher vertical resolution.

Depending upon the characteristics of the sample, a suitable AFM mode has to be chosen prior to image/data acquisition. This chapter discusses contact and tapping modes, although more modes are possible. Contact mode typically provides a constant force to the sample and 'drags' along the surface, with the feedback controller working to keep the constant force. The advantage of contact mode is its conceptual simplicity when scanning a sample, and if the force is kept sufficiently low, the sample will remain undamaged.

Tapping mode involves actuating a cantilever at or near its resonant frequency to provide the maximum amplitude of the cantilever. To keep the distance of the cantilever to the sample, the feedback controller attempts to keep the amplitude of the cantilever constant. This is achieved by expanding or contracting the piezo to ensure a constant amplitude and hence gather topographic

detail about the surface. Minimisation of lateral forces on the surface is achieved in this mode as the cantilever makes intermittent contact, in contrast to contact mode, where the tip 'drags' along the surface.

By driving the cantilever at a given frequency and measuring the return signal, it is possible to measure the phase shift between the driving signal and the received signal, which can provide further detail about the surface, such as differences in stiffness and viscoelastic properties and adhesive forces. It is possible to resolve in greater detail compared to contact mode AFM.

Tip sharpness plays a crucial role in resolving different structures, with sharper tips resolving smaller structures than tips with larger tip radii.

All images in this chapter have had their minimum value set to zero to make comparisons between images and the imaged structures easier as well as having the data levelled to take into account the effects of drift within the system over the scan time.

Characterising hierarchical structures

This work explores a variety of samples with sized silicon micro and nanoparticles. These samples provide a unique challenge in finding hierarchical structures by identifying nanoscale and micro-scale features.

The challenge comes with identifying an appropriate scale to capture the nanoscale features and the larger overall structure. Obtaining topographic scans over various scales can achieve this. Taking scans over different orders of magnitude will give different lateral resolutions. For example, a 2μm scan with 512 data points results in a resolution of 3.9nm/px, whereas a 10μm scan with 512 data points results in a resolution of 19.5nm/px.

A series of samples with increasing silica particle sizes are selected for investigation. The particle diameters under investigation are: 7nm (AEROSIL300), 20nm (AEROSIL90), 40nm (AEROSILOX50) and 4.5μm (SIPERNAT 350). The silica particles adhere to glass slides providing a flat and rigid substrate for imaging, providing a flat and clean surface for AFM imaging.

Figure 3.1 shows an AFM scan of one of the plain glass slides used in this experiment at the scale of images taken with the samples under investigation. The RMS roughness was measured to be approximately 2.74nm; consequentially, the glass slide shows sufficient flatness at this scale to

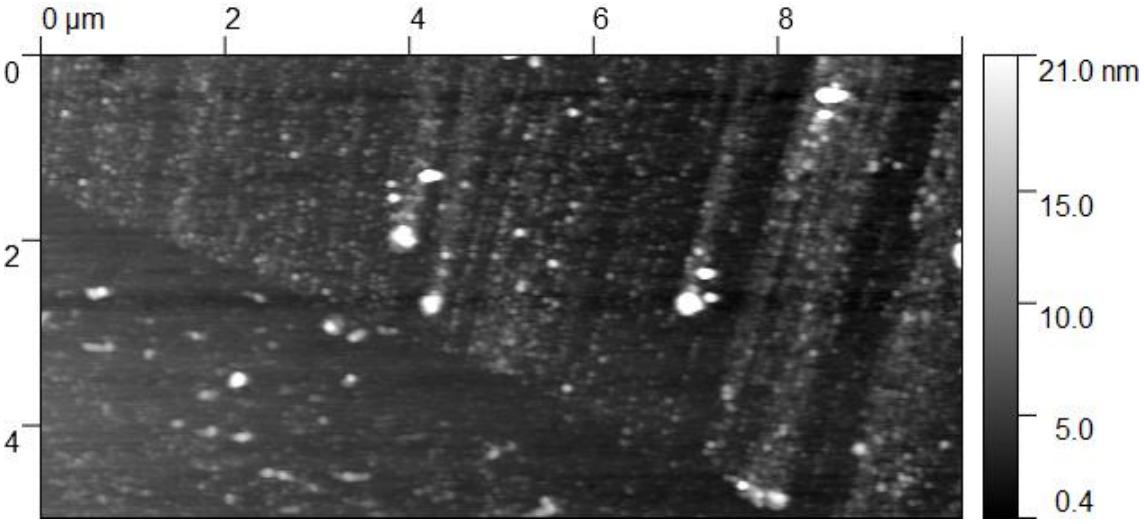

Figure 3.1: 10μm by 5μm scan of a plain glass slide

image the samples with negligible influence of the substrate on the final image.

Glass microscope slides were spray-coated five times with the silica suspension (1 wt % in IPA) using a Sparmax spray gun (GP-35). After each spray coating layer, the slides were dried in air for 20-30s. The silica-coated microscope slides were then immersed in DI water for 5 minutes, rinsed with 50mL of DI water, and left to dry overnight. A PDMS mixture containing the 4.5μm particles was also investigated with the ratio of PDMS to silica microparticles adjusted to determine the effect of increasing the PDMS mixture on the roughness and topography of the surface. The ratios under investigation are; 40/60, 50/50, and 60/40. One further PDMS sample was investigated and consisted of micro-silica covered by PDMS with nano-silica on the surface of the PDMS Figure 3.2 shows the expected variations in surface morphology as a function of PDMS coverage.

3.2 Methodology

Characterisation of hierarchical structures

The samples were loaded onto the microscope stage using the vacuum sample holder, which allows for minimal sample movement during scanning, aiding in the sample's noise reduction. OTESPA (Bruker) cantilevers were chosen for these experiments; this is due to their low-tip radii ($<$7nm), which allows for the scanning of and resolution of the expected smaller features of these samples and its high resonant frequency 270-320kHz making it ideal for tapping mode in air imaging.

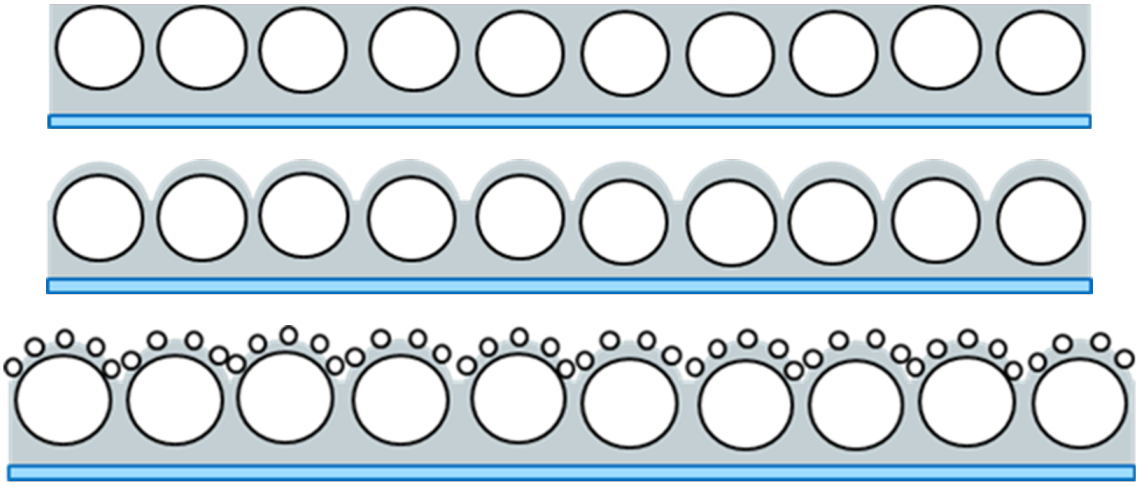

Figure 3.2: Schematics showing the different expected outcomes of PDMS coverings. *Top*: PDMS completely covering the micro-particles, *Middle*: PDMS partially covering the micro-particles. *Bottom*: PDMS partially covering the micro-particles with 7nm nano-particles covering the PDMS.

A standard cantilever holder (DAFMCH, Bruker) is used to mount the cantilever. The laser is aligned to the tip of the cantilever before maximisation of the sum signal, followed by centring the laser spot on the quadrant photodiode. The resonant frequency of the cantilever was then determined by sweeping through a range of frequencies between the expected minimum and maximum of the cantilever and then determining the frequency which gives the maximum oscillation amplitude.

The sample's surface was then brought into focus using the optical microscope, followed by the cantilever. This gives a rough estimate of the distance between the cantilever and the sample for which the cantilever traverses before imaging commences. Once the cantilever is on the surface, the scanning area increases and the PI controller is optimised. The PI values must be sufficiently high for the feedback system to track the surface.

The PI controller optimises by increasing the Integral term until the trace and retrace curves become noisy and then backed off so that the noise is no longer there and once the operator is confident that the trace-retrace curves show the surface's features. Following optimisation of the integral term, the Proportional term is optimised, minimising the area between the trace-retrace curves.

The samples were imaged at various length scales to differentiate between the larger structures of the sample and the nanoscale features.

Measuring the width of SWNT

To measure the changes in the width of Single-walled nanotubes (SWNT) by attaching Polyethyleneimine (PEI) to carboxylic acid (COOH) attached to SWNT. SWNT were dropcasted onto a clean Silicon wafer at various concentrations to increase the probability of imaging the nanotubes individually instead of in a bundle. The concentrations selected were 2.391mg/L and 0.77mg/L for the COOH-SWNT and the PEI-SWNT, respectively. The samples were diluted in DI water from a higher concentration solution of 241mg/L and 78mg/L and sonicated for several minutes to ensure a uniform suspension. A 10μL sample was placed onto the silicon wafer and left to evaporate at room temperature.

OTESPA (Bruker) cantilevers were chosen for these experiments, and these were selected due to their low-tip radii (<7nm), which allows for the scanning of and resolution of the theoretical diameter of the single-walled nanotubes and its high resonant frequency 200-400kHz making it ideal for tapping mode imaging. Topographic images were taken over an area of 1μm by 1μm with an image size of 512 by 512 pixels which gives a pixel size of 1.95nm, which proves sufficient to distinguish between the different types of nanotubes under investigation.

Bacterial Cellulose

The cellulose-producing bacteria used in these experiments was *Komagataeibacter xylinus*. The BslA (Biofilm-surface layer protein A) with and without a CBM were synthesised by TWIST in pET28a. Once obtained plasmids were transformed into *Escherichia coli*, the BslA protein with and without the CBM are super expressed in this bacterium. The *E. Coli* bacteria are harvested and lysed utilising sonication to obtain the protein composition of the bacteria, including the BslA/BslACBM. Although other proteins will be present in the lysate due to the increased expression of the BslA/BslA within the bacteria, these are negligible. The unmodified bacterial lysate is also investigated; this is referred to as 'empty vector' in the text.

The protein concentration within the lysate is analysed using the Bradford assay, which involves binding Coomassie Brilliant Blue G-250 dye to proteins and measuring its absorption at 595nm using a plate reader. The dye binds to proteins in the solution under investigation resulting in a shift in the maximum absorption wavelength from the unbound 465nm to the bound at 595nm, with an increasing amount of protein present in the solution resulting in more absorbance at 595nm

(Bradford, 1976). The resulting value from the Bradford assay was then used to dilute the lysate to the different concentrations under investigation in a tris-based buffer solution. The concentrations of BslA/BslA with CBM under investigation in this work are 50 μg/mL, 250μg/mL and 500 μg/mL.

Two portions of work were undertaken: one is to look at the adhesion between a hydrophobic and control surface and a hydrophilic silicon nitride cantilever and to image bacterial cellulose to determine differences in topography between functionalised bacterial cellulose and control.

The bacterial cellulose was functionalised with BslA or BslA with a carbohydrate-binding module (CBM). The CBM allows for strong attachment between the hydrophobin BslA and the underlying cellulose structure. This was achieved by harvesting the BslA with CBM from *Escherichia coli* by taking the whole cell lysate, and this was dropcasted onto the bacterial cellulose pellicle.

The samples were then prepared for AFM by air drying at 20 $\pm$2°C.

3.3 Results and Discussion

3.3.1 Bacterial Cellulose

Figure 3.3a, shows the topography of a sheet of bacterial cellulose with the empty vector dropcast onto the substrate; this shows that without any BslA, only the bacterial cellulose structure remains present, which consists of long fibres with a width of approximately 100nm. Figure 3.3b, shows the same sheet of bacterial cellulose but at a different location as figure 3.3a with the same size scan it can be seen that there is no significant difference in maximum heights of these samples and that the sample is homogeneous with no difference in widths of the cellulose fibres.

By comparing figures 3.4a and 3.4c which are bacterial cellulose with 50μg/mL of BslA without CBM and with CBM, respectively. When BslA is dropcast onto the surface without a cellulose-binding domain, the fibres remain visible in the topographic image although BslA is present on the surface with additional globular structures visible in both the 5μm and 10 μm scans (Figures 3.4b and 3.4c). The influence of the cellulose-binding domain on the topography of the surface can be seen; where no CBM is present, a layer of protein is covering the fibres, although the fibres remain present in the topographic image, which can be seen as the long fibrous elements present

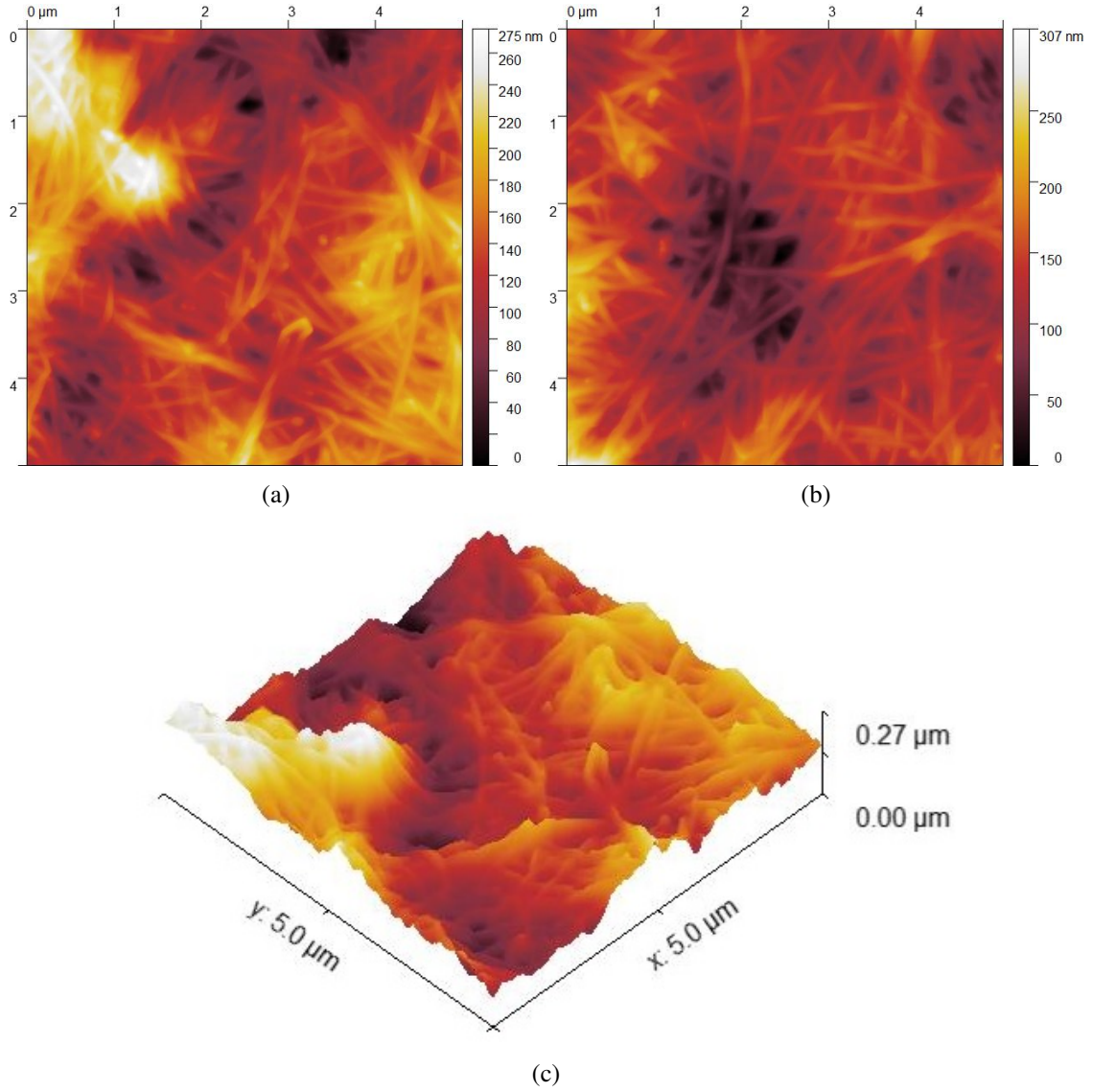

(a) (b)

(c)

Figure 3.3: Tapping mode images of bacterial cellulose taken over an area of 5μm x 5μm; (a) Empty vector and (b) Empty vector, (c) 3D representation of (a).

in the images in figures 3.4a and 3.4b. Whereas when the CBM is attached to the BslA, it shows better coverage for the same concentration of protein dropcast onto the pellicle (Figure 3.4c), this structure is consistent in the larger scan (Figure 3.4d).

When comparing figures 3.5a and 3.5c, it can be seen that at the higher concentration of 250μg/mL of BslA without CBM and with CBM respectively; that the conclusion remains consistent with the lower concentration. Figure 3.5a, shows the underlying fibre structure is visible below the layer of BslA which is consistent with figures 3.4a and 3.4b whereas the BslA with CBM (Figure 3.5c) is consistent to the lower protein concentration in not having a visible fibre structure (Figure 3.4c

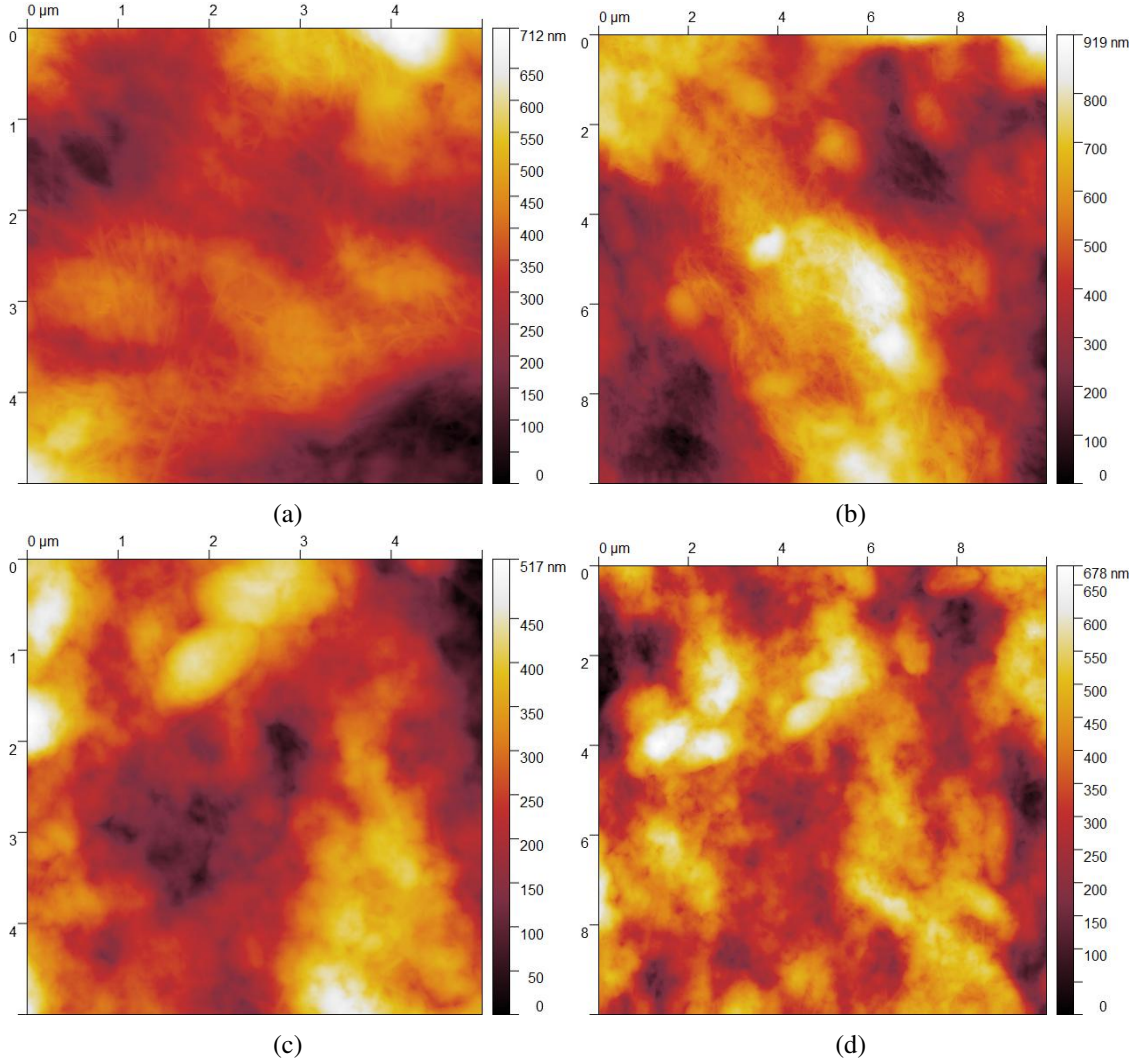

Figure 3.4: Tapping mode images of bacterial cellulose functionalised with 50μg/mL BslA without CBM over a scan area of; (a) 5 μm by 5 μm and (b) 10 μm by 10 μm. Tapping mode images of Bacterial cellulose functionalised with 50μg/mL BslA with CBM over a scan area of; (c) 5 μm by 5 μm and (d) 10 μm by 10 μm.

and 3.4d).

It can be noted that the lower concentration shown in figure 3.4a and that of the increased concentration shown in figure 3.5a that the network of fibres becomes difficult to distinguish at the higher concentrations.

A higher concentration of BslA was also investigated. Figures 3.6a and 3.6b, shows a similar structure to 3.5a with globular structures present within the network of bacterial cellulose; although at the higher concentration the amount of fibres not buried by the BslA reducing (see figures 3.4a and 3.5a to see this sequence). Additionally, the difference between the max and min values of the

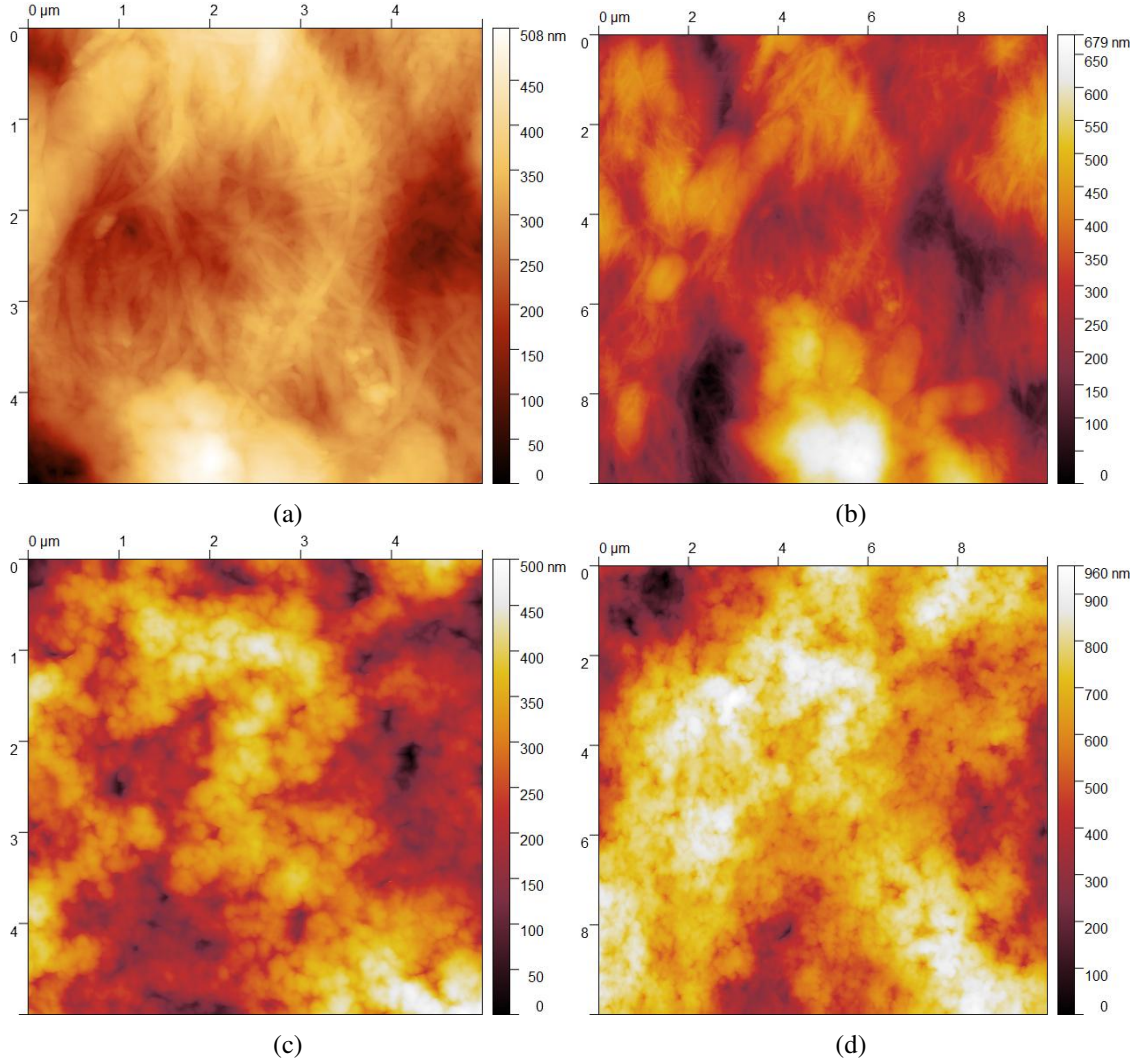

Figure 3.5: Tapping mode images of Bacterial cellulose functionalised with 250μg/mL BslA without CBM over a scan area of; (a) 5 μm by 5 μm and (b) 10 μm by 10 μm. Tapping mode images of Bacterial cellulose functionalised with 250μg/mL BslA with CBM over a scan area of; (c) 5 μm by 5 μm and (d) 10 μm by 10 μm.

two topographic images is only 6nm; showing that with an additional 250μg/mL of BslA doesn't result in any significant change in surface morphology.

The RMS roughness measurement of these samples at the same length scale backs up this observation with a negligible decrease in RMS roughness between the 250μg/mL sample and the 500 μg/mL sample (Figure 3.7).

The presence of the BC fibres can be observed in the line scans extracted from the AFM images (figure 3.8), extracted at arbitrary points although the same behaviour described here is observed throughout the images. When observing the line-scans extracted from the empty-vector sample

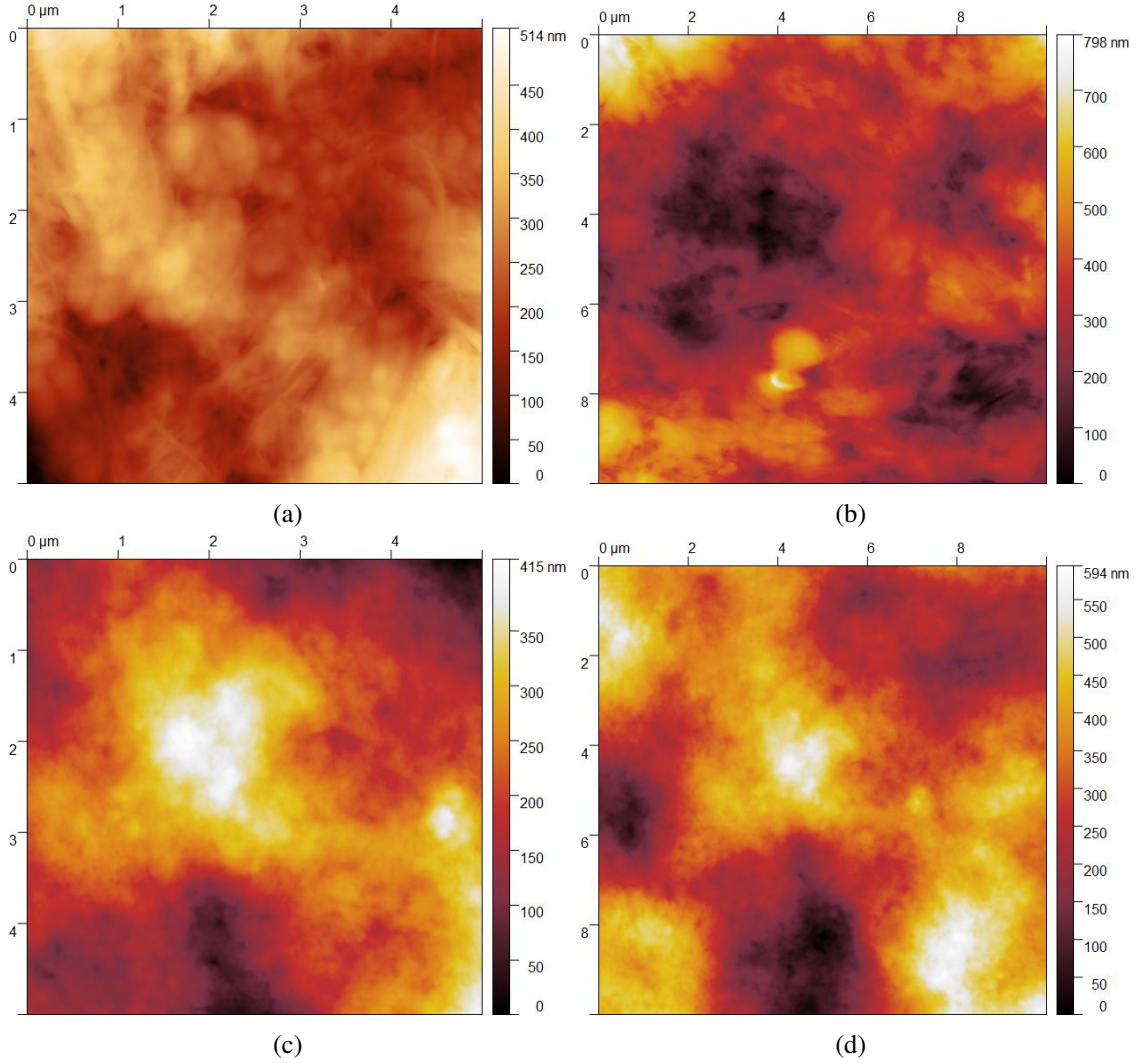

Figure 3.6: Tapping mode images of Bacterial cellulose functionalised with 500μg/mL BslA without CBM over a scan area of; (a) 5 μm by 5 μm and (b) 10 μm by 10 μm. Tapping mode images of Bacterial cellulose functionalised with 500μg/mL BslA with CBM over a scan area of; (c) 5 μm by 5 μm and (d) 10 μm by 10 μm.

it can be observed that the line-scans contain low frequency oscillations corresponding to the presence of bacterial cellulose fibres (Figures 3.8a, 3.8b).

These low frequency oscillations remain present when BslA is added to the surface of the bacterial cellulose, in the line-scan presented in figure 3.8d, the lower frequency, high amplitude oscillations are present. In the line-scan, higher frequency oscillations are present showing the coating of BslA on the sample.

In the line scan extracted from the sample with the BSLA-CBM coating (Figure 3.8f), the higher frequency oscillations have a smaller amplitude, implying better adhesion to the BC fibres when

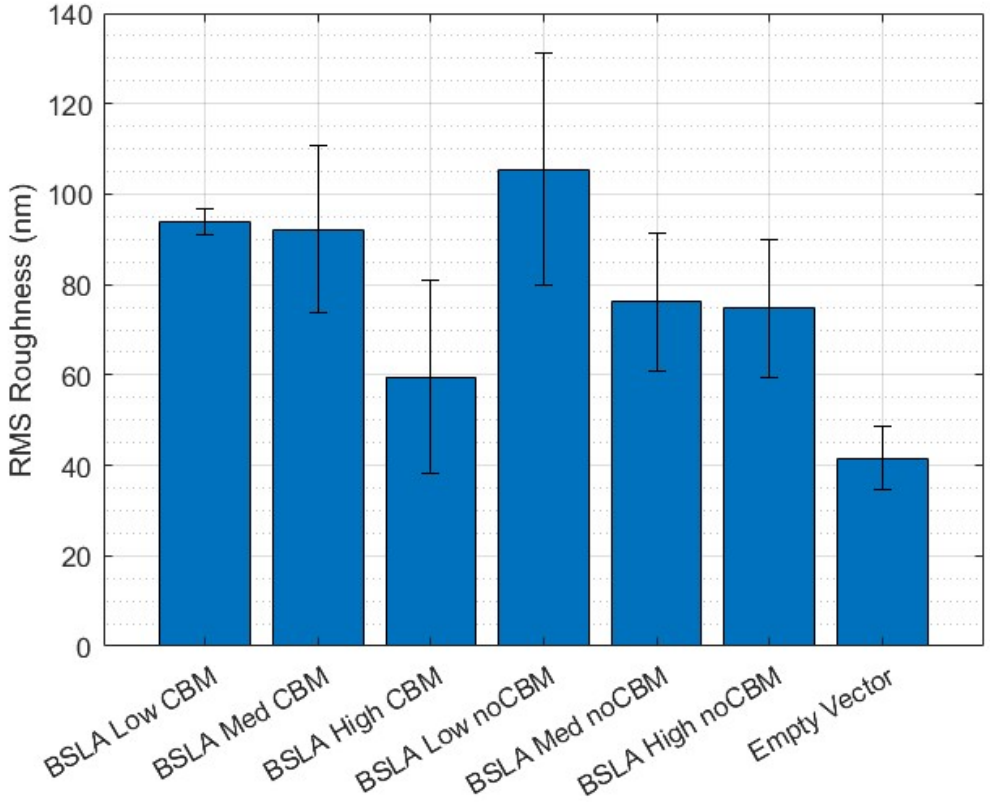

Figure 3.7: Bar Graph comparing RMS roughness as a result of changing the functionalisation of the BC surface

compared to the sample without CBM (Figure 3.8d).

3.3.2 Cell Morphology

Methodology

Fibroblast images were taken at a scan rate of 0.49Hz using an MLCT-E cantilever (Bruker) with an applied driving frequency of 29.02kHz, which lies within the expected range of frequencies for this cantilever (26-50kHz) with a nominal spring constant of 0.1N/m.

Analysis

Figure 3.9a shows a topographic image of a focal adhesion point of a fibroblast cell with a maximum height of 1.22μm. Figure 3.9c shows the corresponding phase image to figure 3.9a; this was obtained simultaneously and focused on the difference in phase between the driving frequency and the return signal. This reveals some interesting details of the cell which are not visible in the

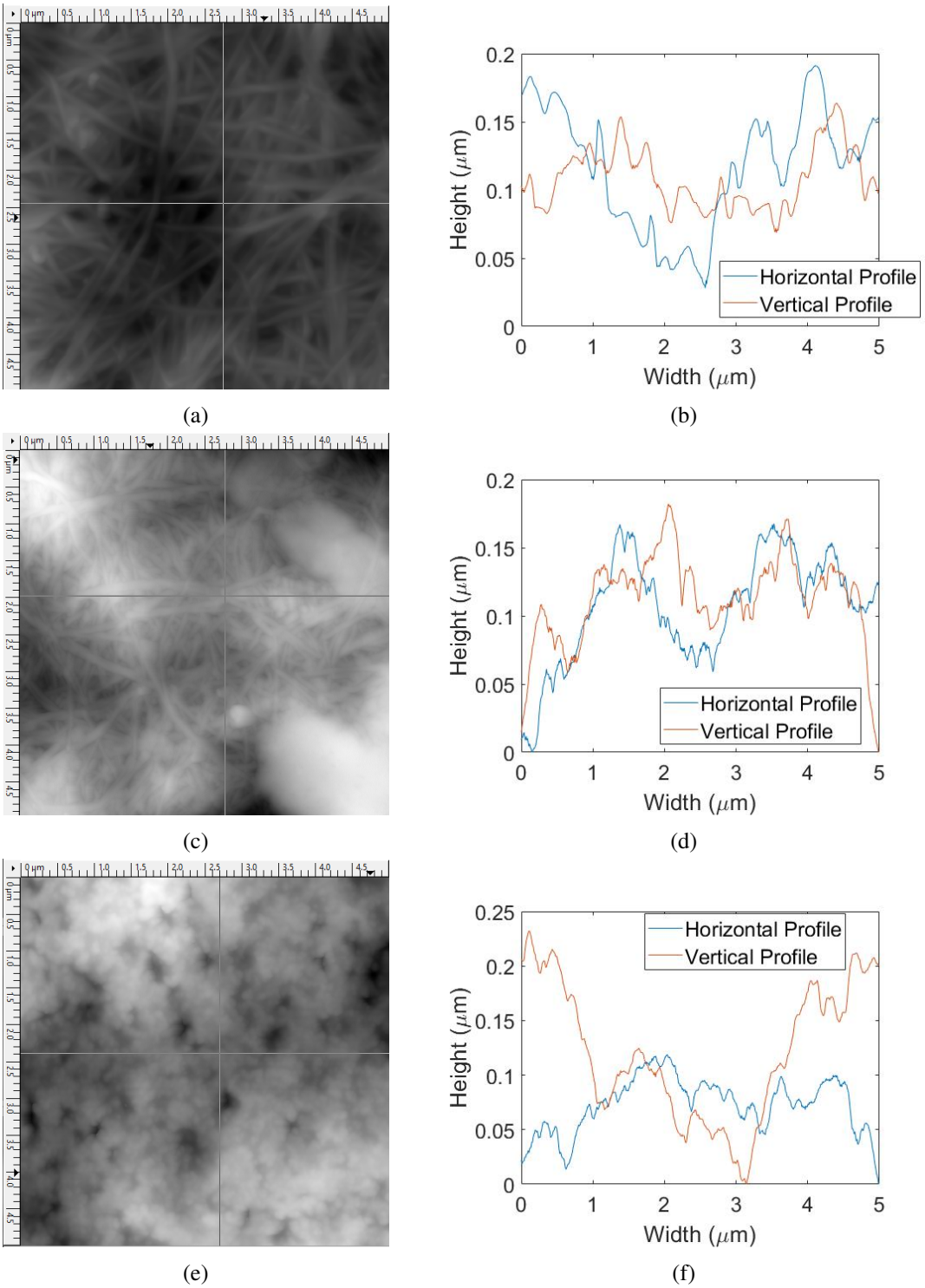

Figure 3.8: Line scans of Bacterial Cellulose; a) Empty Vector AFM image with overlaid lines highlighting extracted points shown in b). c) AFM image of Bacterial Cellulose functionalised with 250μg/mL BslA without CBM (c) with overlaid lines highlighting extracted points shown in (d). e) AFM image of Bacterial Cellulose functionalised with 250μg/mL BslA with CBM (c) with overlaid lines highlighting extracted points shown in (f).

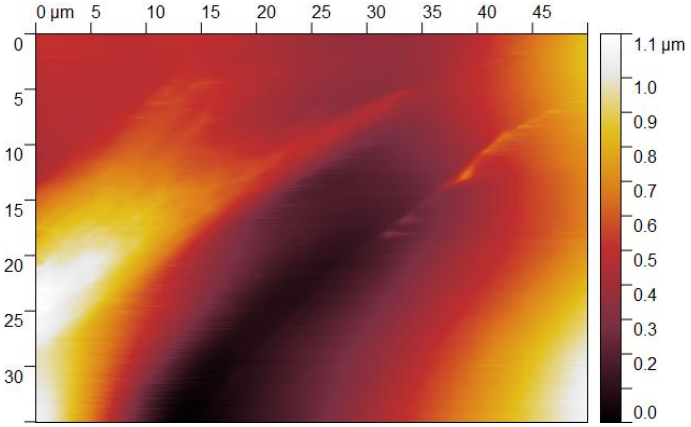

(a)

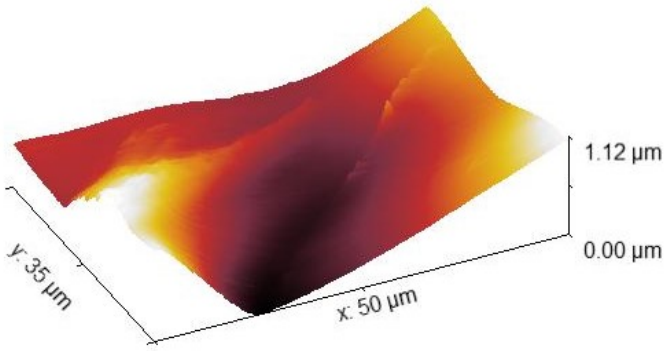

(b)

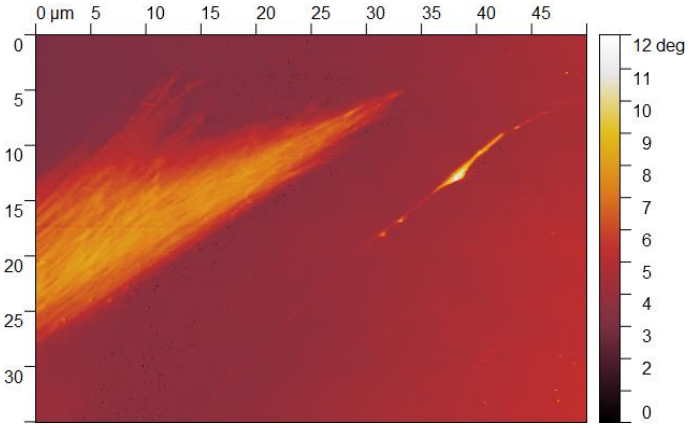

(c)

Figure 3.9: Tapping mode images were taken over an area of 50μm by 35μm of a fibroblast cell on the edge of a cell. a) Topographic image. b) 3d representation of a. c) Phase image, d) 3d representation of c.

topographic image; these actin filaments are found in the cytoskeleton of cells and play crucial roles in the motility of cells, cell structure and cell division.

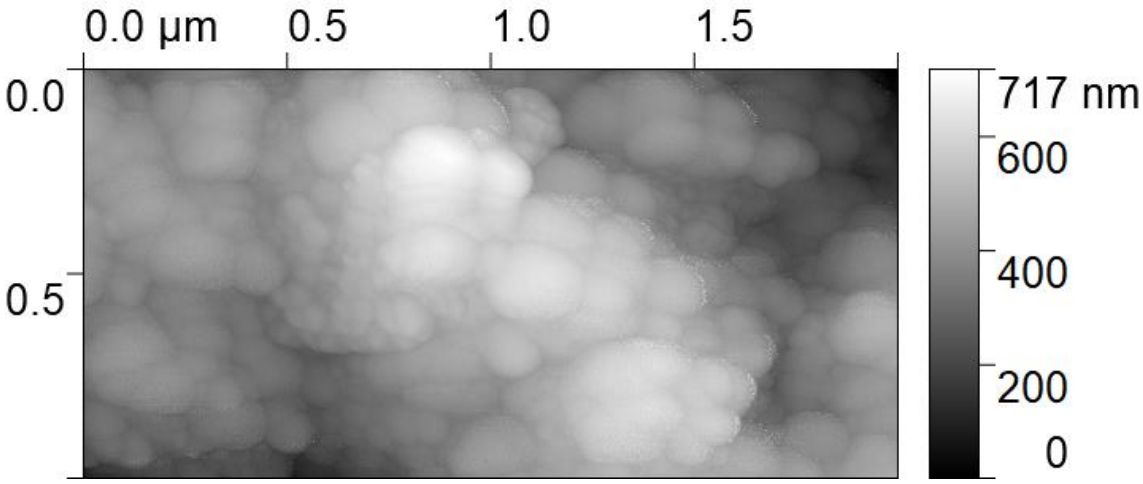

(a)

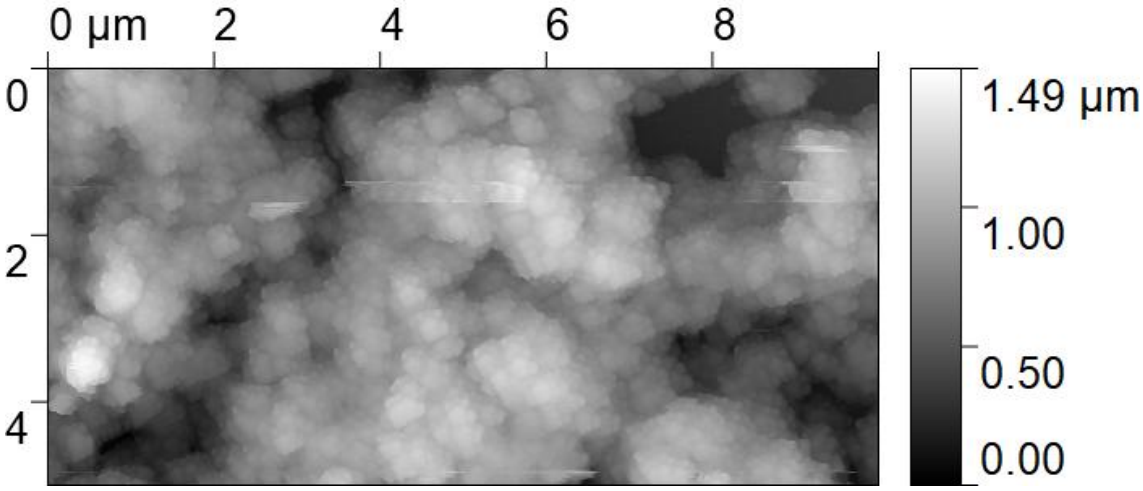

(b)

Figure 3.10: Topography of 40nm silica micro-particles taken over an area of; a) 2μm by 1μm and b) 10μm by 5μm.

3.3.3 Silica micro and nanoparticles

Scans were taken over different sizes to gauge the different structures that may form when adding in different sized particles, one to see the finer structure to resolve the different micro/nanoparticles and over a larger area to resolve any clustering of beads and where appropriate hierarchical structures where a combination of nanoparticles and micro-particles are used. Figures 3.10b, 3.11b and 3.12b, show the topography of a variety of different particle surfaces on surfaces. It is possible to distinguish the difference in particle sizes between each of the samples at a glance, whereby there is a decrease in the periodicity of the particles across the samples.

Figure 3.13a and 3.13b, is an example of a hierarchical surface. The small scan (Figure 3.13a)

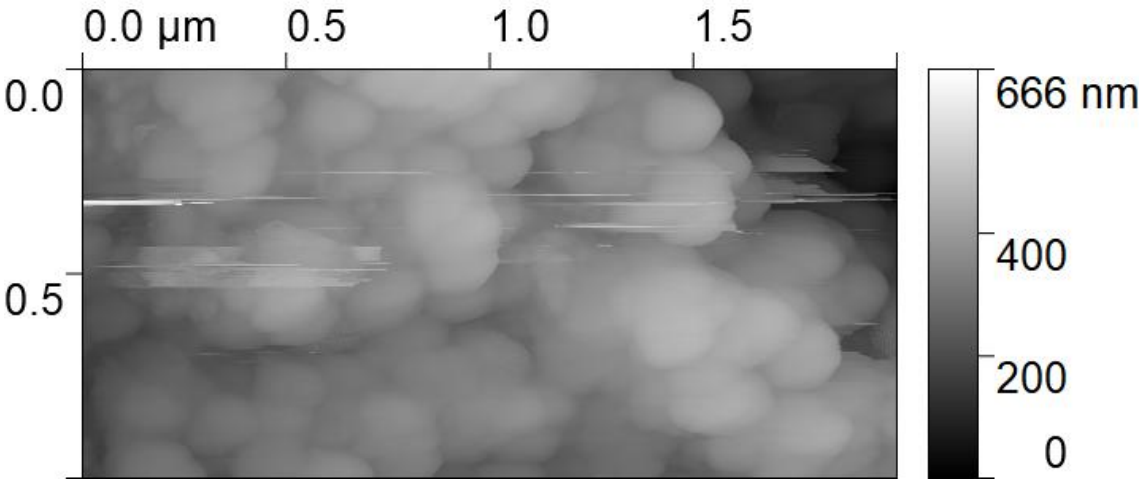

(a)

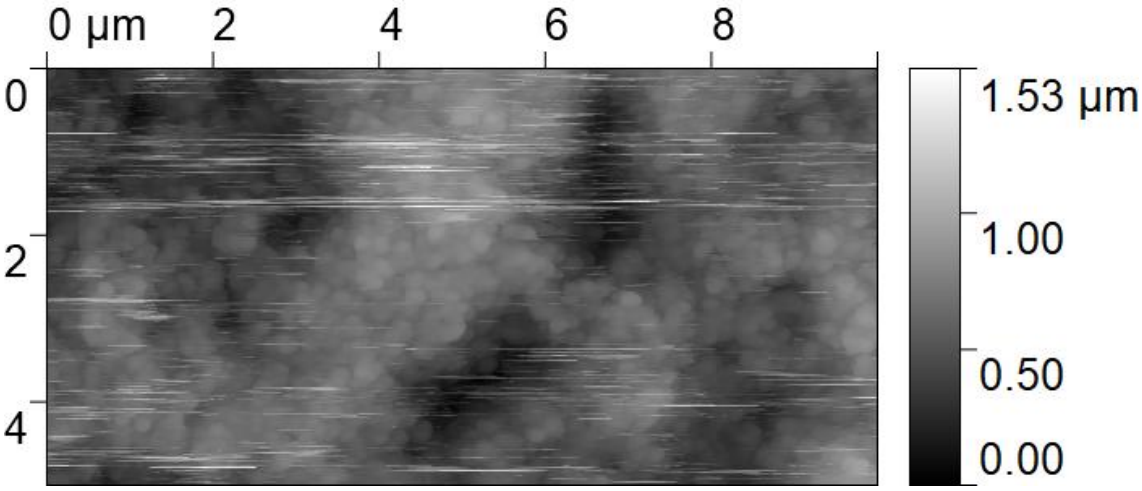

(b)

Figure 3.11: Topography of 20nm silica micro-particles images taken over an area of; a) 2μm by 1μm and b) 10μm by 5μm.

shows a structure which is similar in form to what is already seen over the same length scale as Figure 3.11a are the same size nanoparticles are used. There is very little difference in the RMS roughness of the two samples at this scale, with the sample without the underlying micro-particles having an RMS roughness of 84nm compared to 93nm.

It is seen that on the larger topographic scan (Figure 3.13b) that there is an underlying structure with an increase in the height of the scan from 1.53μm to 2.85μm and an increase in the RMS roughness of the samples from 178nm to 301nm.

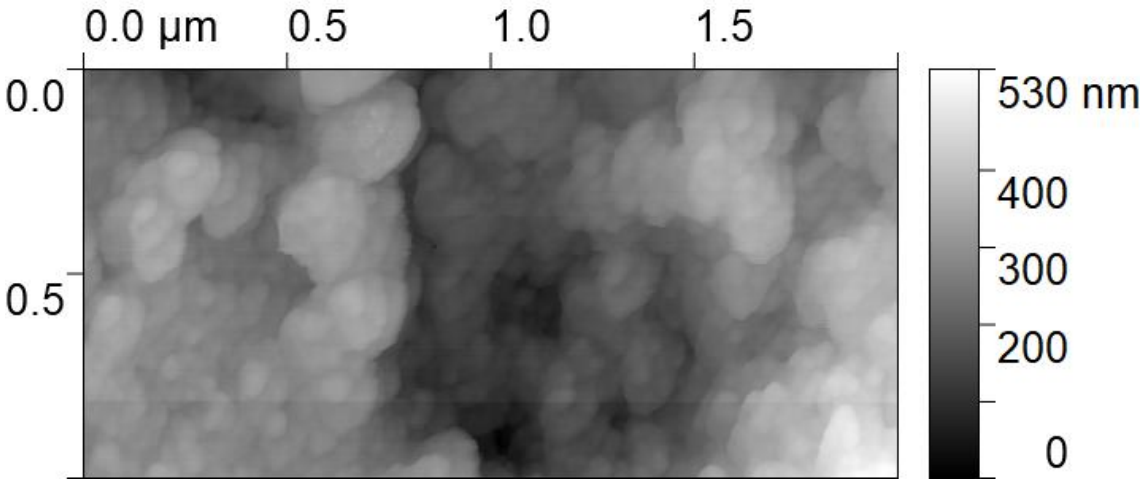

(a)

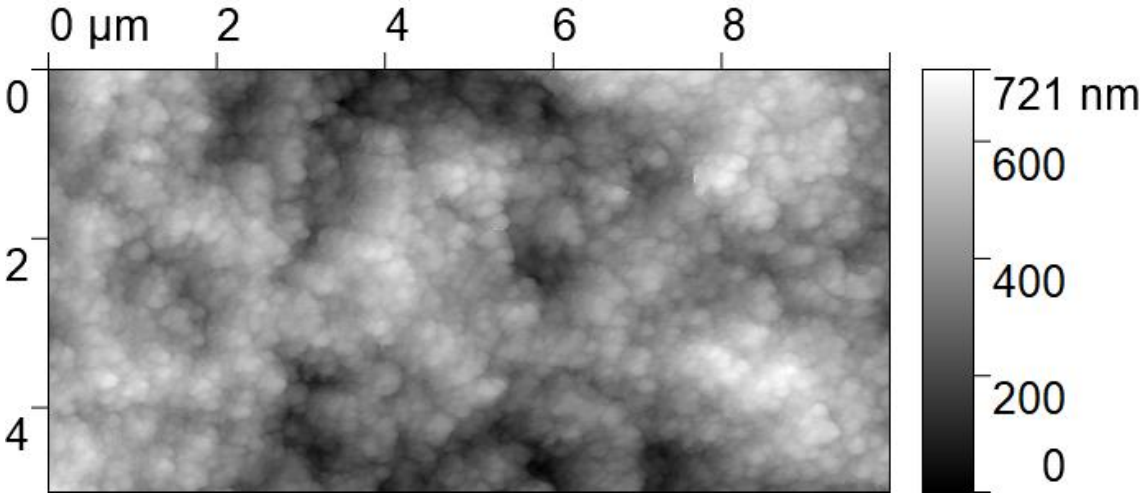

(b)

Figure 3.12: Topographic of 7nm silica images taken over an area of; a) 2μm by 1μm and b) 10μm by 5μm

3.3.4 PDMS covered micro and nanoparticles

The effect on the topography of the samples by varying the PDMS layer on the Silica nanoparticles can be measured. There are a few suitable measures of this; the difference between the sample's peaks and troughs and the root mean square roughness (RMS). As the ratio between the PDMS and the Silica micro-particles increases, it is hypothesised that the sample will flatten with the PDMS filling in the gaps between the micro-particles until such a ratio is reached whereby the sample is just flat PDMS with the silica micro-particles embedded into the PDMS. However, a flat PDMS sample is not achieved in the three samples under investigation, as shall be demonstrated here, but the effect is measured.

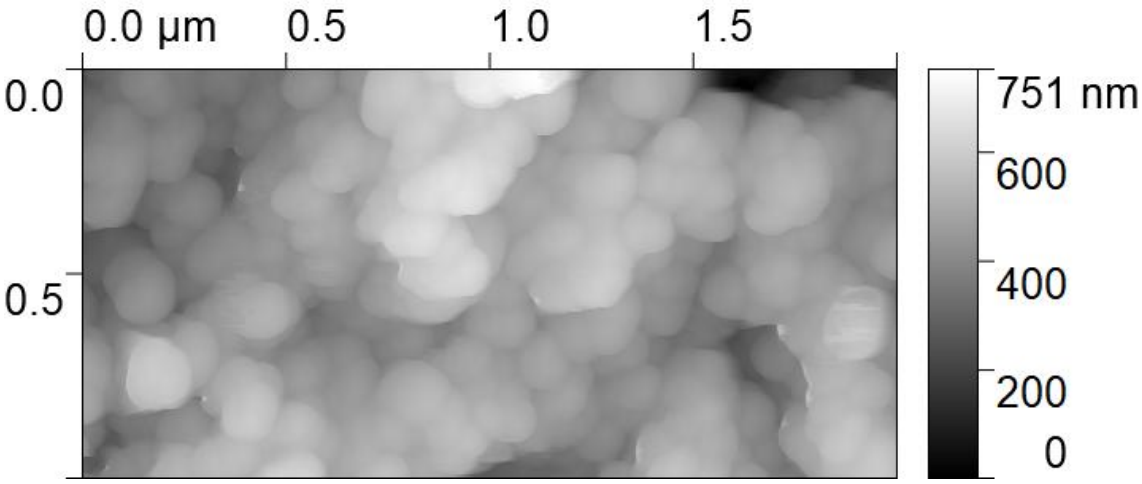

(a)

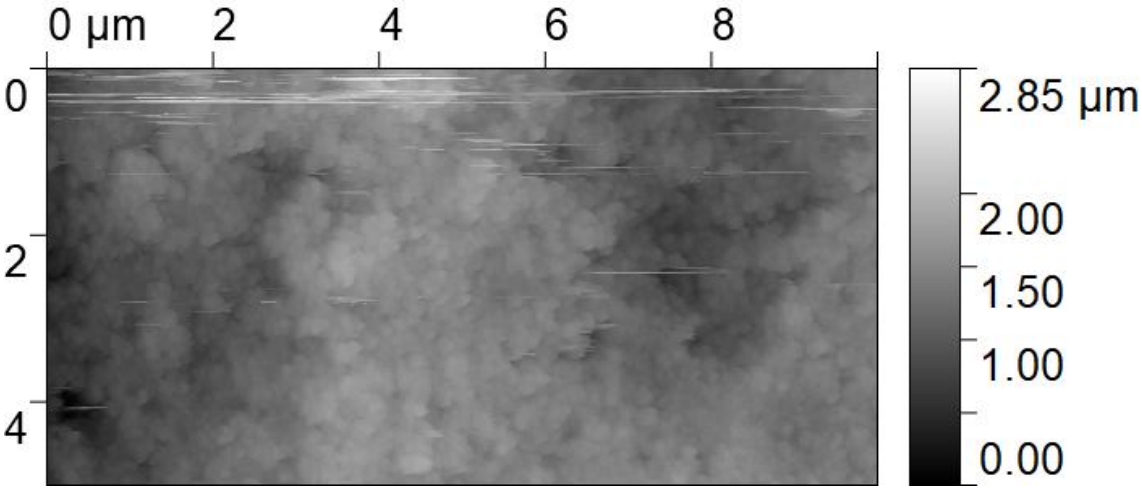

(b)

Figure 3.13: Topographic of 4.5μm micro-particles with 20nm nanoparticles on the surface of the micro-particles silica images taken over an area of; a) 2μm by 1μm and b) 10μm by 5μm

When comparing figures 3.14b, 3.14d and 3.14f, it can be seen that as the amount of PDMS increases relative to the silica microparticles, the difference between the lowest point and the highest point on the topography decreases. This is further shown when comparing the RMS roughness of each of these scans, which are; 726.62nm, 588.62nm and 344.34nm, respectively. The decrease in these values shows that the PDMS is smoothing out the peaks and troughs of the sample with an increase in the ratio of PDMS to silica microparticles.

Figures 3.15a, 3.15c and 3.15c, show PDMS coated micro-particles such as those found in figures 3.14a and 3.14b with an additional layer of 7nm nano-particles such as those found in figures 3.12a and 3.12b.

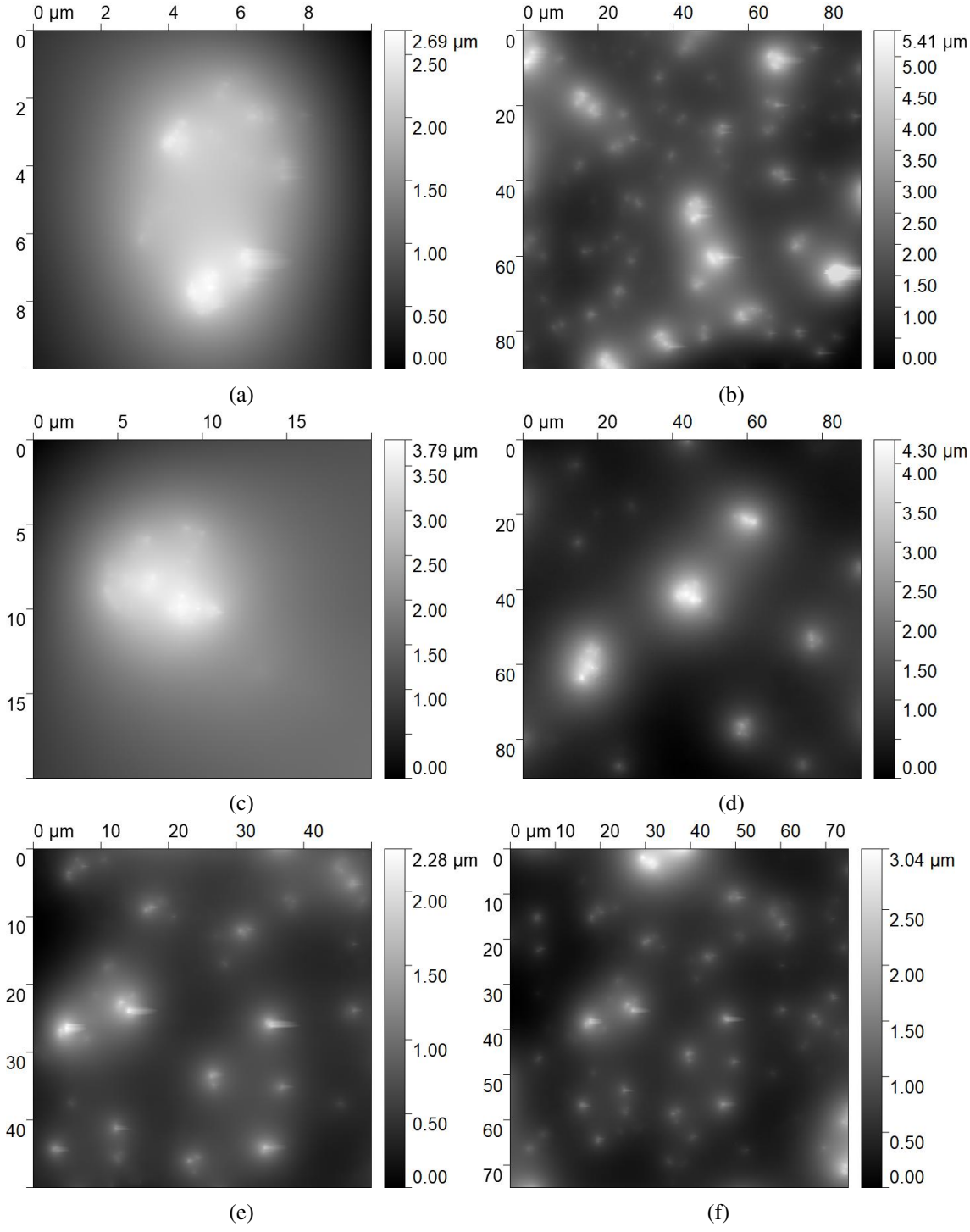

Figure 3.14: Scan of a 40/60 mix of Silica micro-particles with a PDMS covering, with scan sizes of; a) 10μm by 10μm b) 90μm by 90μm. Scan of a 50/50 mix of Silica micro-particles with a PDMS covering, with scan sizes of; c) 20μm by 20μm d) 90μm by 90μm. Scan of a 60/40 mix of Silica micro-particles with a PDMS covering, with scan sizes of; e) 50μm by 50μm f) 75μm by 75μm.

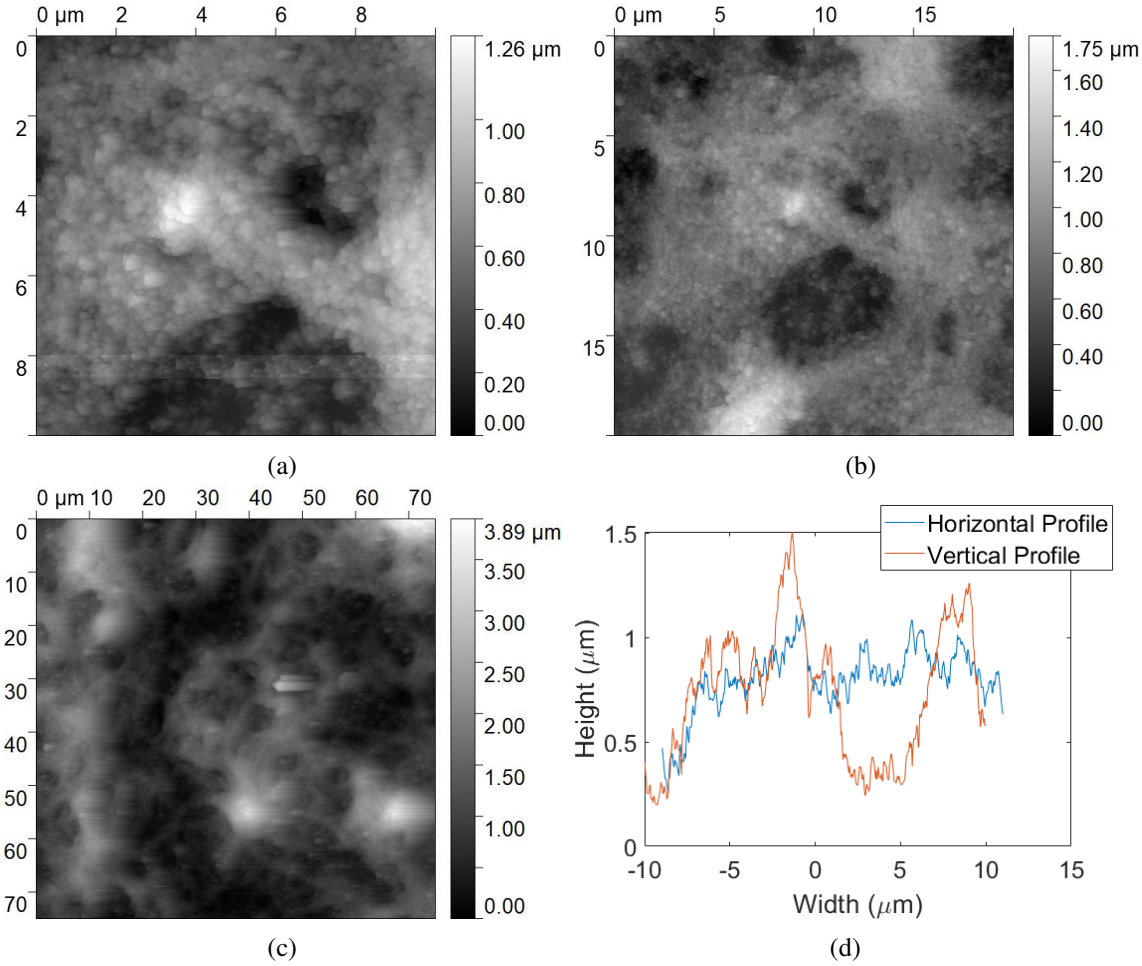

Figure 3.15: Scan of 4.5μm silica micro-particles coated with PDMS and 7nm silica nano-particles over areas of; a) 50μm by 50μm b) 75μm by 75μm c) 20μm by 20 μm. d) Line profiles extracted from figure 3.15b along the horizontal (blue) at 9μm and vertical (orange) at 9 μm.

Figure 3.15d shows a line scan taken as a cross-section of figure 3.15b centred on 9μm in x and 9μm in y; this shows the larger micro features shown by, the larger amplitude peaks which make up the underlying structure on which the smaller amplitude nano features sits.

Measuring Widths of SWNTs

Uniform deposition from dropcasting onto the silicon wafer was not observed; however, the coffee-ring effect was experienced, whereby most nanotubes were at the edge of the sample as the droplet evaporated. However, some nanotubes would have been deposited throughout the area, although most were visible at the edge of the dropcasted area, Figure 3.16a shows a representative place where these topographic images were taken.

The topographic images were imported into an AFM image analysis software to determine the

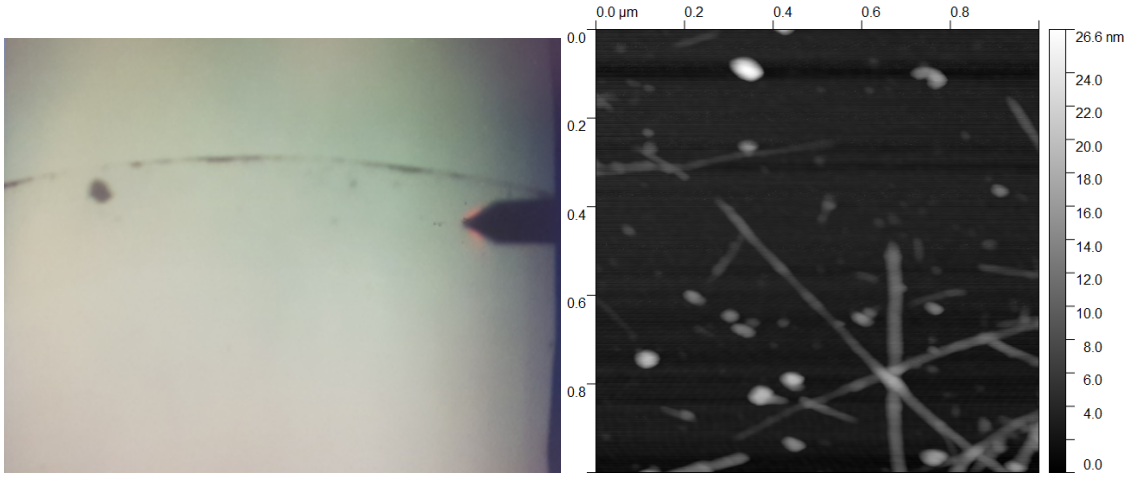

(a) (b)

Figure 3.16: a) Optical Microscope image with the cantilever engaged on the surface position from which topographic scans were taken, showing the coffee ring effect experienced when drop casting the SWNT samples b) Topographic scan of COOH-SWNT showing several SWNTs.

widths of the SWNTs; multiple perpendicular profiles across multiple SWNTs were extracted, giving the cross-sectional profile of the SWNTs from which the widths can be determined. For each SWNT imaged, multiple profiles were extracted along the length of the SWNT to build up a histogram of widths to get a mean value and the standard deviation for each SWNT.

The profiles were then imported into MATLAB for further analysis, where the width of the CN can be determined. Figure 3.17a shows a representative profile across the width of a SWNT. The flat portion to the left of the SWNT corresponds to the silicon wafer on which the SWNT are deposited before the height increases, which corresponds to the SWNT before decreasing again back down to the silicon wafer. The distance between the start and end of the SWNT is then measured and compiled into a histogram. The data is then fitted to a normal distribution with the mean and standard deviations extracted.

For the COOH-SWNT sample, a total of 20 CNs had their profiles extracted, with an average of 9.15 profiles extracted per SWNT. The mean width was 41.1nm, with a standard deviation of 7.7nm.

For the PEI-SWNT sample, a total of 16 CNs had their profiles extracted, with an average of 8.69 profiles extracted per SWNT. The mean width was found to be 59.1nm with a standard deviation of 7.8nm.

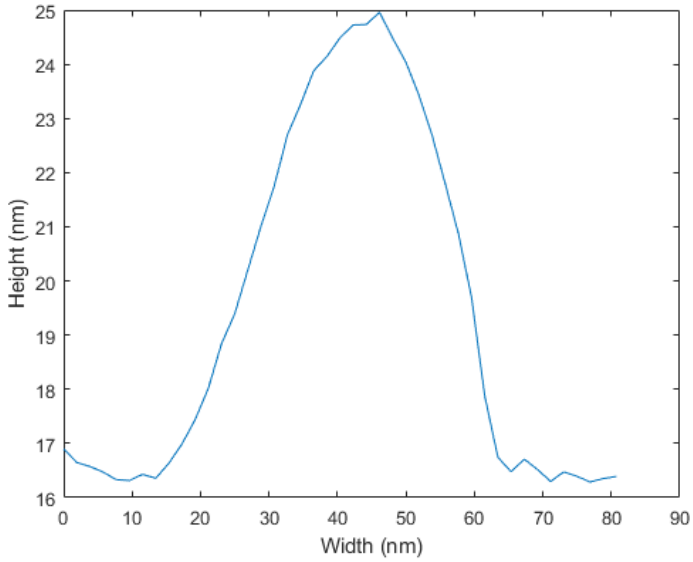

(a)

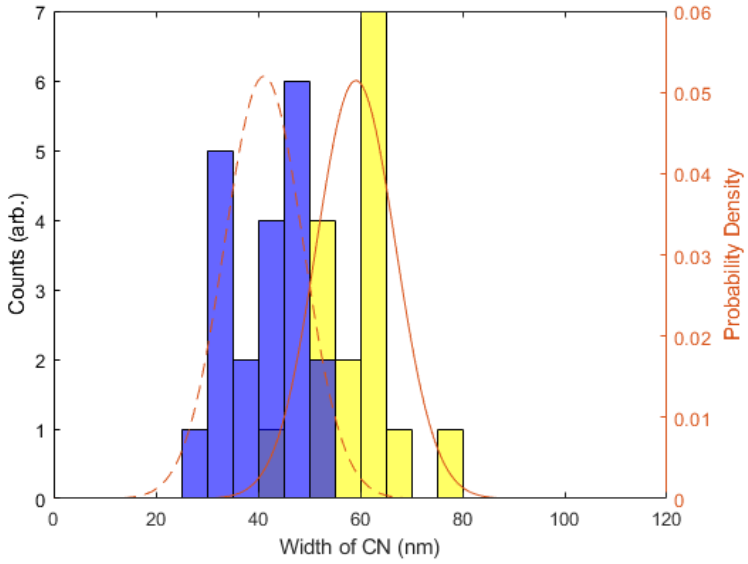

(b)

Figure 3.17: a) Representative line profile through a SWNT, b) A histogram comparing the difference in widths between COOH-SWNTs (Blue histogram and orange dashed fitted probability density function) and PEI-SWNTs (Yellow histogram and orange fitted probability density function)

Figure 3.17b shows a comparison between the COOH-SWNT (grey-histogram and orange dashed distribution) sample and the PEI-SWNT (blue-histogram and solid orange distribution). It can be seen from this comparison that there are two distinct distributions. Due to the data sets being of unequal sample sizes, Welch's t-test was selected to determine the statistical significance of the data set. The difference in widths between the two types of SWNTs is found to be significant

($p<0.005$), and the null hypothesis was rejected.

The AFM images show a successful attachment of PEI to COOH-SWNT as given by the increase of approximately 18nm of the SWNT widths.

3.4 Summary

This chapter explores the use of AFM as a method for characterizing and measuring various surfaces. The initial samples investigated were Bacterial Cellulose, which was functionalized with BslA, either containing a Carbohydrate-binding domain or lacking this domain. The investigation focused on determining any topographic changes exhibited when BslA/BslACBM is added to the cellulose post-growth. It was found that the functionalization of BslA to the bacterial cellulose fibers resulted in a change in the RMS roughness of the sample and visible alterations in the topography of AFM scans. A clearer difference in topography was observed when BslA with CBM was functionalized to the fibers.

This surface characterization and its implications set the stage for a case study involving normal human dermal fibroblasts (NHDF) to measure the effect of acousto-mechanical stimulation on cells, an exploration that will be detailed in the next chapter.

Chapter 4

Mechanical stimulation of cells and characterisation using SAW

4.1 Introduction

A case study of normal human dermal fibroblasts (NHDF) was studied to measure the effect of acoustomechanical stimulation on cells. Characterisation experiments using SAW stimulated cells were performed in this research. Characterization experiments using Surface Acoustic Wave (SAW) stimulated cells were performed in this chapter, leading us to delve into the effects of acousto-mechanical stimulation on fibroblasts.

In this chapter, a case study involving normal human dermal fibroblasts (NHDF) was undertaken to investigate the effects of acousto-mechanical stimulation on cellular behavior. Characterization experiments used Surface Acoustic Wave (SAW) stimulation, using two techniques: Atomic Force Microscopy (AFM) and cell counting. AFM provided a nanoscale perspective, looking at mechanical changes within cells subjected to mechanical stimuli, while cell counting offered quantitative insights into cellular proliferation.

4.2 Methodology

4.2.1 Surface Acoustic Waves

Fabrication of SAW devices

ZnO thin film was chosen as the piezoelectric material for the SAW devices. ZnO thin film was deposited on an 10cm^2 Aluminium plate of 1.6mm thickness using physical vapour deposition (PVD). A direct current reactive magnetron sputtering system (Nordiko) with two zinc targets of 99.99% purity was used to produce the thin film of ZnO on the Aluminium plate. The surfaces of the plates were cleaned with acetone, rinsed in ethanol and then with deionised water, and dried with nitrogen.

The deposition process was performed by flowing Oxygen into the deposition chamber to oxidise the Zinc to form ZnO. The aluminium plate was positioned 20 cm away from the targets, and the holder rotated at 4rpm. The vacuum pump was turned on, and a chamber pressure of 3.75mTorr was maintained during deposition. A flow of argon/oxygen (Ar/O2) with a ratio of 10/15 mixture was used. The optimal parameters were selected based on the quality of the thin film and the thickness of the ZnO layer.

The ZnO thin film was characterised using scanning electron microscopy (SEM) to examine the morphology and cross-section. The film structure, orientation and crystallinity were characterised using X-ray diffraction. The surface roughness was characterised by atomic force microscopy.

The Cr/Au IDT design was fabricated using standard lithography, magnetron sputtering and lift-off processes. The samples had photoresist (S1813, Rhom and Haas) spin-coated onto the surface of the thin film ZnO layer with a low rotational speed (10 rpm for 10s) initially followed by a higher rotational speed of 3700rpm for 60 seconds. The samples were then placed onto a hot plate to soft bake at 95°C for 10 minutes. A UV exposure dose of 90mJ was applied to the samples using an EVG620 mask aligner, followed by immersion in MF319 developer solution for 1 minute to develop the photoresist. The samples were then rinsed with DI water and dried with dry nitrogen.

Similar devices have been used for; Reducing the contact time of droplets on a surface (Biroun

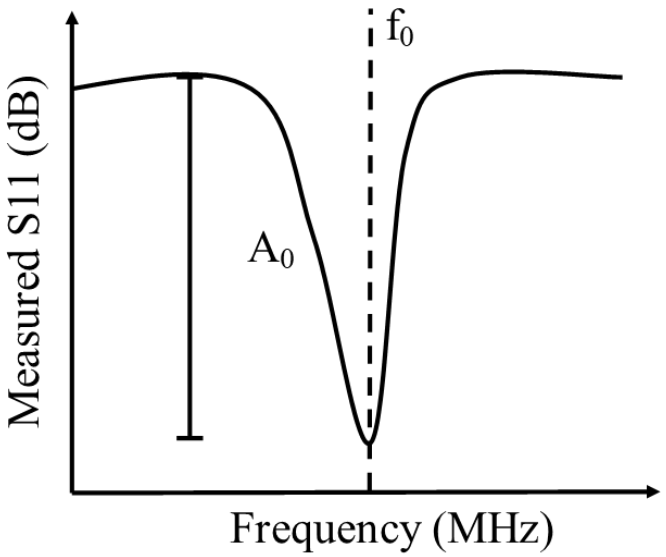

Figure 4.1: Schematic of a typical S11-Frequency response graph with f_0 and A_0 labelled

et al., 2020*b*), droplet jetting (Li et al., 2020) and droplet control and manipulation (Vernon et al., 2022).

SAW characterisation

SAW devices are characterised by their S11 properties, which are measured by looking at the frequency spectra of the SAW devices were characterised using a Vector Network Analyser (Keysight N9913A Fieldfox handheld analyser). Figure 4.1, shows a schematic of a typical S11-frequency response graph centred around the ideal frequency (f_0) of the SAW device and the value of A_0 corresponding to the return loss of the device and hence is a measure of the quality of the coupled SAW power.

The properties of the devices used in this research are outlined in Table 4.1 in the SAW treatment section below (§4.2.1).

SAW stimulation

Surface Acoustic Wave devices are utilised in these experiments to acousto-mechanically stimulate Normal Human Dermal Fibroblasts. In this work, four devices were used with differing properties as outlined in the table below.

Figure 4.2, shows the scheme for which the cells were stimulated. The cells were stimulated with a

Table 4.1: Table listing the SAW devices utilised in the following experiments ($\bar{A_0}$ is the average return loss of the device over all experiments)

Device	Wavelength (μm)	S_{11}Frequency (MHz)	$\bar{A_0}$
1	200	14.035	1.3
2	200	14.193	0.55
3	300	9.489	0.9
4	100	27.071	0.9

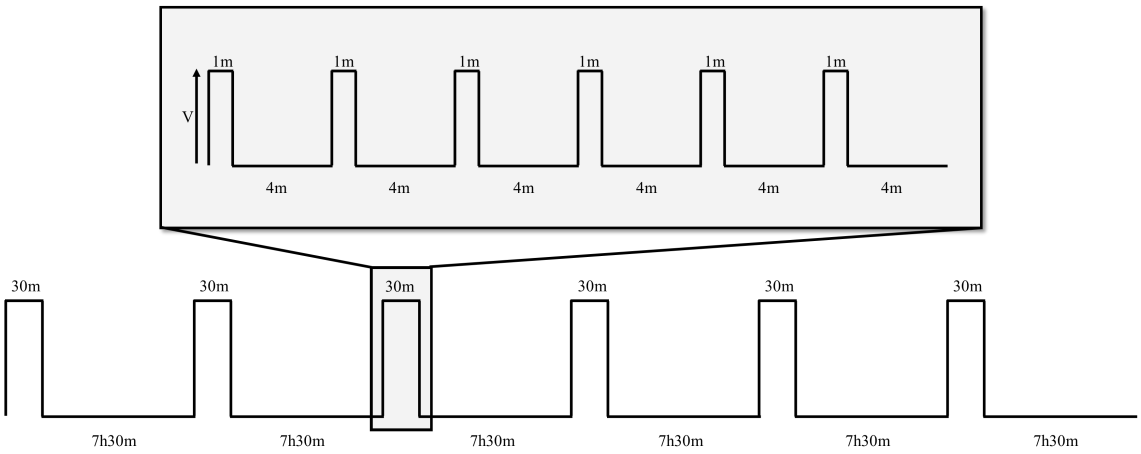

Figure 4.2: Diagram showing the scheme for stimulating cells. The bottom portion shows the overall 48-hour-long experiment with the 30-minute spikes representing when the stimulation profile occurs which is shown in the top portion of the diagram.

duty cycle of 20% at the given S_{11} frequency for the device for over half an hour before resting for seven and a half hours when the next stimulation profile begins. This is repeated a total of six times before a selected experiment is performed upon the cells. Figure 4.2 is true for the first device, however, for subsequent devices, their start is delayed for half an hour after the first device, then half an hour after the second device and so forth. The reason for the delayed start of the devices is due to the limitations of the experimental set-up where the signal generator can only output to one device at any given time.

Figure 4.3, shows the experimental set-up used for the SAW stimulation. The set-up uses a Raspberry Pi connected to a signal generator with the Pi controlling both the frequency and amplitude of the signal generator's output. The output of the signal generator is connected to a PCB with RF switches which are controlled by the Pi which allows for the correct frequency to be output to the appropriate device. This system can be set up using either a smartphone or a PC using commercially available remote desktop software and software developed using python to achieve the functionality mentioned.

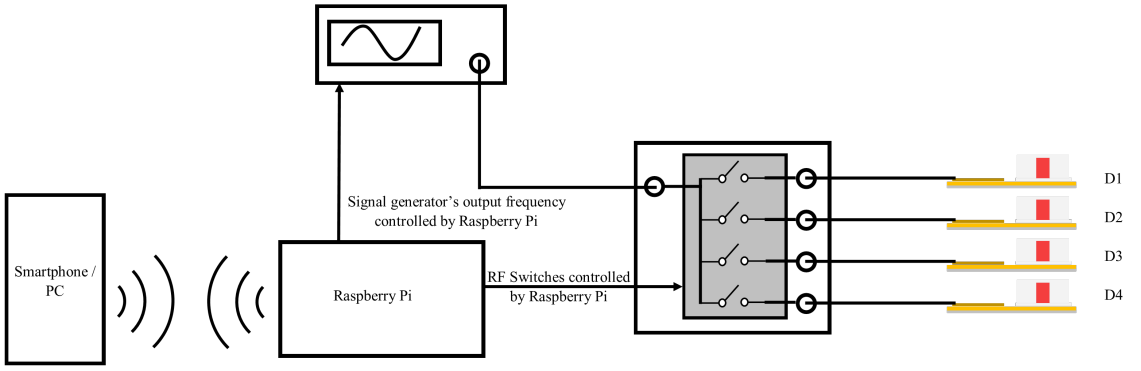

Figure 4.3: Diagram of the experimental set-up used for the stimulation of NHDF cells using SAW. D1-4 refers to Devices 1-4 in Table 1.

PDMS chamber fabrication

To fabricate the chambers that are used to contain the medium and the cells, Polydimethylsiloxane (PDMS) was chosen as the material to create the chamber walls with a glass substrate (22mm x 22mm with a thickness of 170μm) where the cells will be adhered to. PDMS is chosen for this role due to its elasticity, biocompatibility (Bélanger and Marois, 2001), and its ability to be attached to glass which is a substrate on which the NHDF cells are capable of growing on without further surface functionalisation.

A mould was created using Fused Deposition Modelling (FDM) using either Acrylonitrile Butadiene styrene (ABS) or Polylactic acid (PLA), with 1.5cm diameter rods of a height of 2cm forming the negative of the chamber which were stuck to a petri dish using double-sided adhesive tape. The rods were arranged in a grid such that there is an equal spacing between the chambers thereby controlling the thickness of the PDMS walls.

PDMS was fabricated using a SYLGARD™ 184 Silicone Elastomer kit which consists of two parts: the pre-polymer base and the cross-linker cure. The base and the cure were added in a 10:1 (w/w) mixture to create the desired PDMS mix. The combined mix was then stirred for five minutes to ensure that the two parts are completely mixed as this allows for the cross-linking of the polymer chains. This was then poured over the mould until the mould is at the desired level then the mixture was degassed using a vacuum pump to remove any bubbles that may appear when the PDMS goes through the heat cure step as this may damage the final chambers. Once a negligible number of bubbles were left, the mould was then placed inside a heated oven for three hours at 70°C converting the liquid material into a solid elastomer.

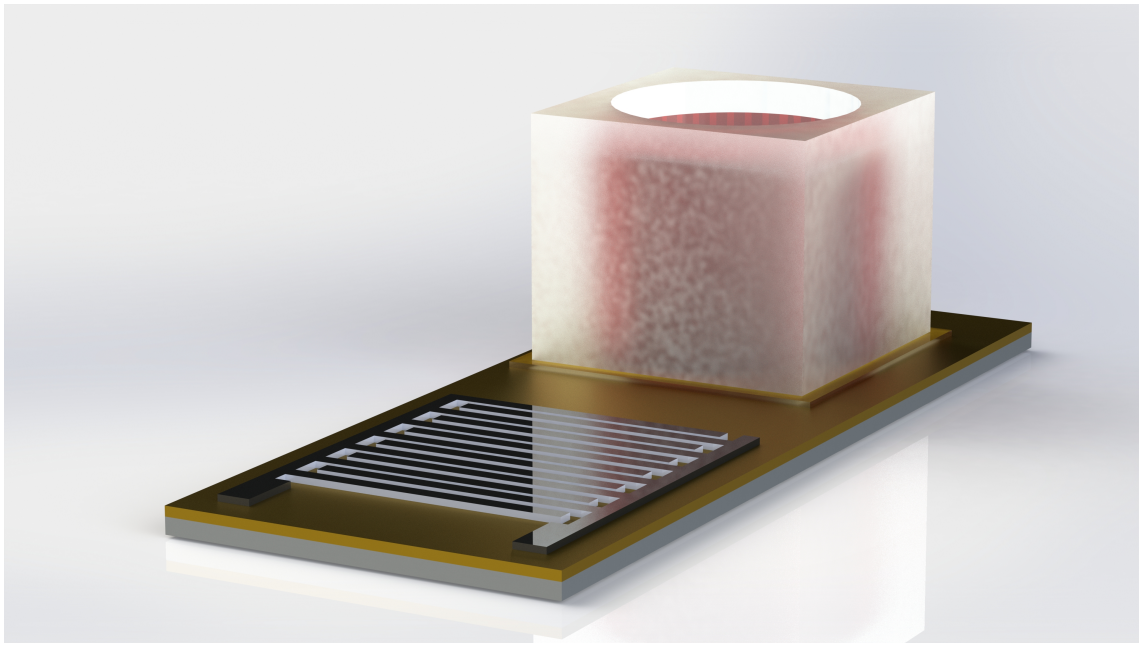

Figure 4.4: Conceptual render for the stimulation of cells using a SAW transducer and a PDMS chamber

For experiments that required the chambers to be bonded to the glass, the glass and the PDMS chamber are placed inside a plasma oven. The plasma oven was used to seal the PDMS to the glass substrate, this is achieved by the creation of OH groups on the surface of the PDMS and the glass which creates a bond between the glass substrate and the PDMS. This was achieved by using a plasma oven set at 100W for 1 minute using air plasma. This creates a permanent seal between the PDMS and the glass coverslip ensuring that the chamber is watertight.

Where the chamber is to be removed from the glass, the PDMS chamber is placed on a glass coverslip to create a temporary seal between the glass and the PDMS chamber. This method is used for AFM and confocal experiments.

Chamber preparation for SAW stimulation

The chambers are either treated using the plasma oven to permanently bond the chamber to the glass coverslip or left untreated depending on the assay that is performed afterwards. The chambers are submerged in a 70%/30% ethanol-water mix for 30 minutes before being removed and left to dry. Cells are then trypsinised from sterile cell culture, counted using the haemocytometer and then the correct volume for each chamber is calculated for the given experiment. To ensure the even distribution of cells across all chambers, the total number of cells for all chambers is

calculated and this is removed from the supernatant and then added to the correct volume of media used in the experiment.

The diluted cell suspension is then divided up among the chambers, for most experiments the number of cells per chamber is set to be 10,000 cells in 1mL of complete media. The cell suspension is pipetted into the chamber and left to settle at room temperature in the class II biosafety cabinet for 3 hours. The chambers are then attached to the SAW devices by adding a layer of ultrasound gel (Ultrasound gel 250mL, Revitive) to the point just after the IDTs, the chamber is then placed on top of the ultrasound gel and the chambers and devices are placed inside a conventional tissue culture incubator held at 37°C with 5% CO_2 concentration. Figure 4.4, schematically shows the set-up with a chamber placed on the SAW device.

4.2.2 Atomic Force Microscopy

Single cell microrheology experiments

AFM measurements were performed using a commercial setup (Veeco, Dimension 3100), silicon nitride cantilevers with nominal spring constants of k=0.01N/m with a probe radius of 20nm. (MLCT-C, Bruker Probes). These cantilevers were chosen for these experiments due to their low spring constant which reduces the force on the cells and hence the chance of damaging the cell during indenting experiments. The cantilever was mounted onto a liquid holder which was placed onto the end of the piezo tube.

The PDMS chamber was removed carefully from the glass coverslip, leaving a pool of liquid on top of the cells, the AFM head was then slowly stepped down towards the media-covered glass coverslip until a meniscus was formed between the liquid holder and the sample. The system was then left to come to equilibrium before any force measurements were undertaken.

The coverslip was brought into focus using the built-in microscope to set the approximate z-height that the cells would be at. A selected point was chosen to allow for calibration of the inverted optical lever sensitivity (InvOLS); the point selected was one without any cells so that the probe was on just the glass.

The tip was then retracted and the stage moved such that the tip was brought into a position that when the tip was engaged and the Z-stage moved down that the tip would indent upon the cell. The

tip is then engaged and began indenting upon the cell. The amount of indentation was controlled by stepping the Z-stage up or down to get a large portion of the force-curve not in contact before the tip indents upon the cell, this was to ensure that when the force-curve was fitted with the appropriate model that the contact point is clear.

For most single-cell experiments, approximately 20 force curves were taken in one spot before the tip was retracted by 10μm and moved by approximately 100nm a total of 5 times. Between 100-200 force curves were taken per cell using triangular oscillations of the cantilevers and a ramp size of 5μm with a frequency of 1Hz. The cells were indented between 1-2μm with the peak force applied to be approximately 10nN.

Each force curve was fitted using the Hertzian Blunted Pyramidical Model (Rico et al., 2005);

$$F = \frac{E\tan(\theta)}{\sqrt{2}(1-\nu^2)}\delta^2 \tag{4.1}$$

The face angle θ was taken to be 17.5° and Poisson's Ratio (ν) taken to be 0.5 using the assumption that cells are incompressible. Curves were fitted with between 300nm and 700nm of indentation. Equation 4.1 can be rearranged to give an equation in the form $y = mx$, which is useful for fitting acquired force curves.

$$\sqrt{F} = \sqrt{\frac{E_{\text{eff}}\tan(\theta)}{\sqrt{2}(1-\nu^2)}}\delta \tag{4.2}$$

This gives the gradient of the line m to be;

$$m = \sqrt{\frac{E_{\text{eff}}\tan(\theta)}{\sqrt{2}(1-\nu^2)}} \tag{4.3}$$

This equation can be rearranged to give the effective Young's modulus (E_{eff});

$$E_{\text{eff}} = \frac{\sqrt{2}(1-\nu^2)m^2}{\tan(\theta)} \tag{4.4}$$

Analysis

For the analysis of force-curves as written in section 4.3.2, a MATLAB script and a Graphical User Interface (GUI) was developed using GUIDE which is a built-in graphical user interface creator in MATLAB. The GUI is created to allow the user to select the contact point on a given force-curve

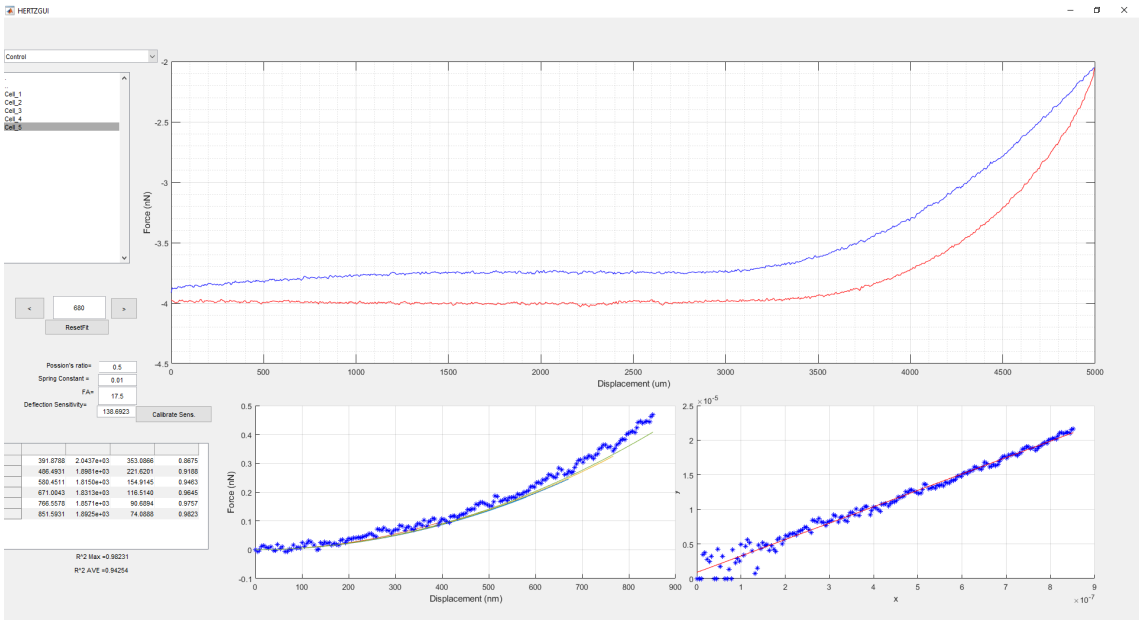

Figure 4.5: Screenshot of the GUI for selecting the contact point and fitting the appropiate model.

and fit the chosen contact model.

Figure 4.5, shows a screenshot taken from a force-curve being fitted. The top-left portion of the GUI shows where the user can chose the experiment through a drop-down menu which when selected populates the list below with the folders containing the data from each cell. The user can then select the cell that they are interested in undertaking data analysis with and then the first file in this folder is then loaded in and displayed on the large graph on the right hand side of the GUI.

Before the user can undertake force-curve analysis, the user must put in the values into the text-input fields for Possion's ratio, Spring constant, the Face-angle and the Deflection Sensitivity. If the deflection sensitivity is unknown or if the user wishes to calibrate this from a force-curve acquired on a hard surface then when the user presses the 'Calibrate Sens.' button then a smaller file browser window is shown to allow the user the ability to choose this calibration file. When this file is loaded in then the force-curve is shown on the large graph on the right side with the y-axis changing to volts and the x-axis remaining in nanometres. The user's mouse cursor then becomes a cross-hair for choosing start point, this is confirmed by pressing the left mouse button and then the end point is chosen using the same method; the section of the force-curve corresponding to the start and the end points is fitted using a linear fit which gives the gradient to be the deflection sensitivity (invOLS), this value then populates the deflection sensitivity text-input field.

The user can press 'Reset Fit' or reselect the cell that they wish to undertake the force-curve analysis with, this then populates the large graph on the right side of the GUI and the mouse cursor becomes a cross-hair for selecting the indentation point and once this is confirmed with a press of the left mouse button then the code begins fitting the force-curve with a variety of different indentation depths. The bottom two graphs shown give an idea about how well the force-curves are being fit to the data, with the graph on the right side showing the points fitted around a linearised version of the fitting equation and the left hand side takes the values from the fit and replots through the range of the respective points used for the fitting.

The curve-fitting algorithm used gives a variety of important values, the values used in the analysis of the data are the Effective Young's modulus, the indentation depth, the Error in the calculated Effective Young's modulus value and the goodness of fit value (R^2). When the force-curve has been fitted for all of the indentation depths, the table in the bottom-left of the GUI is populated with the values mentioned. The values in the GUI are listed in table 4.2;

Table 4.2: Data extracted from force-curve analysed in figure 4.5

Indentation Depth	Effective Young's Modulus	±Effective Young's Modulus	R^2
391.8788	2.0437e+03	353.0866	0.8675
486.4931	1.8981e+03	221.6201	0.9188
580.4511	1.8150e+03	154.9145	0.9463
671.0043	1.8313e+03	116.5140	0.9645
766.5578	1.8571e+03	90.6894	0.9757
851.5931	1.8925e+03	74.0888	0.9823

This table is then sent to the system's clipboard using the nun2clip library (Browning, 2022), for pasting to a spreadsheet editor for collation of the data and further analysis. The code which accompanies this can be found in Appendix A.

4.2.3 Cell preperation

Cell culture

For in vitro experiments, we chose the NHDF cell line. All cell culture procedures were conducted within a class II biosafety cabinet to minimize the risk of contamination, whether from other cell lines or bacteria.

Figure 4.6 displays a bright-field microscope image of fibroblasts in culture. Notably, these cells

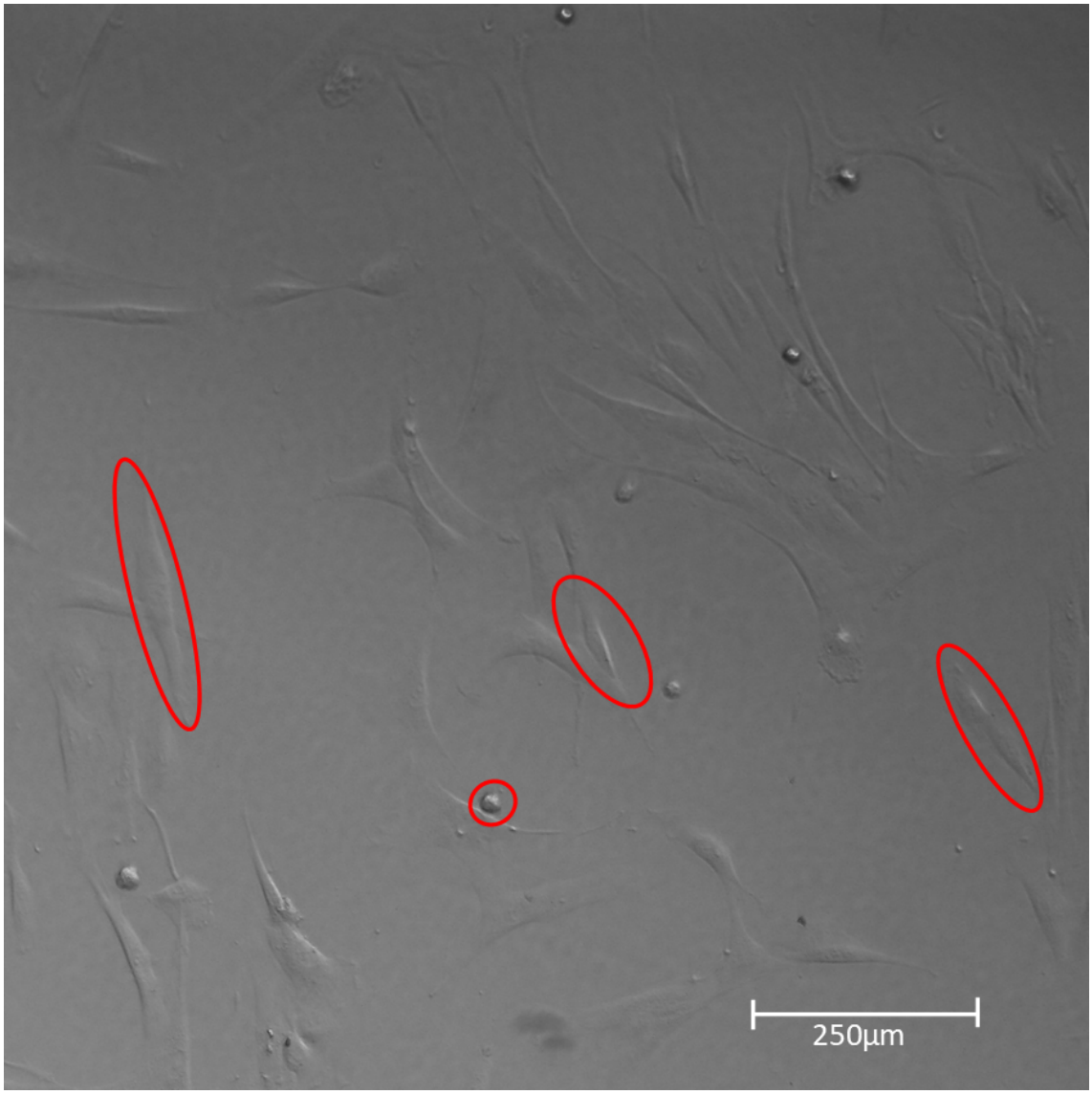

Figure 4.6: Bright-field microscope image of NHDF cells in culture on a glass substrate with a field of view of 1.2mm. With some of the cells circled in red.

exhibit an elongated, ellipse-like morphology. The exceptions to the ellipse-like shape are circular cells, which can be identified as either undergoing apoptosis (cell death) or mitosis.

Retrieval and revival of cells from long-term cryopreservation

Cell lines were brought back to an active state from long-term storage at -150°C. This was accomplished by immersing the cryovial in a bath held at 37°C, causing the cells suspended in the cryomedia (composed of 90% v/v complete media and 10% v/v DSMO) to thaw. The contents of the cryovial were subsequently transferred to a falcon tube, and 10 mL of complete media was introduced to the vial in order to dilute the cell suspension.

The falcon tube containing the diluted cells was then subjected to centrifugation at 1600 rpm for 6 minutes. This process led to the separation of a supernatant (liquid above the pellet) and a cellular pellet (solid mass at the bottom of the tube). The supernatant was carefully taken out, and the cellular pellet was re-suspended in complete media. Finally, the re-suspended cells were transferred to sterile tissue culture flasks.

Routine cell culture

Routine cell culture involves the maintenance of cell lines to ensure their continued viability and growth. This involves the feeding and splitting of cell lines. The NHDF cell line was cultured in complete media consisting of DMEM supplemented with FBS (10% v/v) and penicillin streptomycin (1% v/v).

NHDF cells were cultured in standard culture flasks held at 37°C in a 5% CO_2 environment at high humidity, this is to ensure that the cells are cultured in an environment closely mimicking that of the human body. Cells were split when they reach approximately 70-80% confluency, this is achieved by washing the cells with PBS and then using the enzyme trypsin to release the cells from the substrate for approximately 3 minutes at 37°C.

The trypsin is then neutralised using complete DMEM with a volume of one and a half times more than that of the trypsin leaving the cells in suspension. The cells are then centrifuged at 1600rpm for 6 minutes, which leaves the cellular pellet and supernatant. The supernatant was then pipetted off and the cells were resuspended in 1mL of complete DMEM for either cell counting or passaging.

Cell counting

Routine cell culture

In the experiments outlined in this thesis involving cells, a haemocytometer was used to count cells. A haemocytometer is a useful tool for a wide variety of biological samples from blood counts, sperm counts and counting eukaryotic cells. Figure 4.7a, shows a schematic of a haemocytometer which consists of a thick piece of glass with a small depression in the middle in which two chambers are located with a grid.

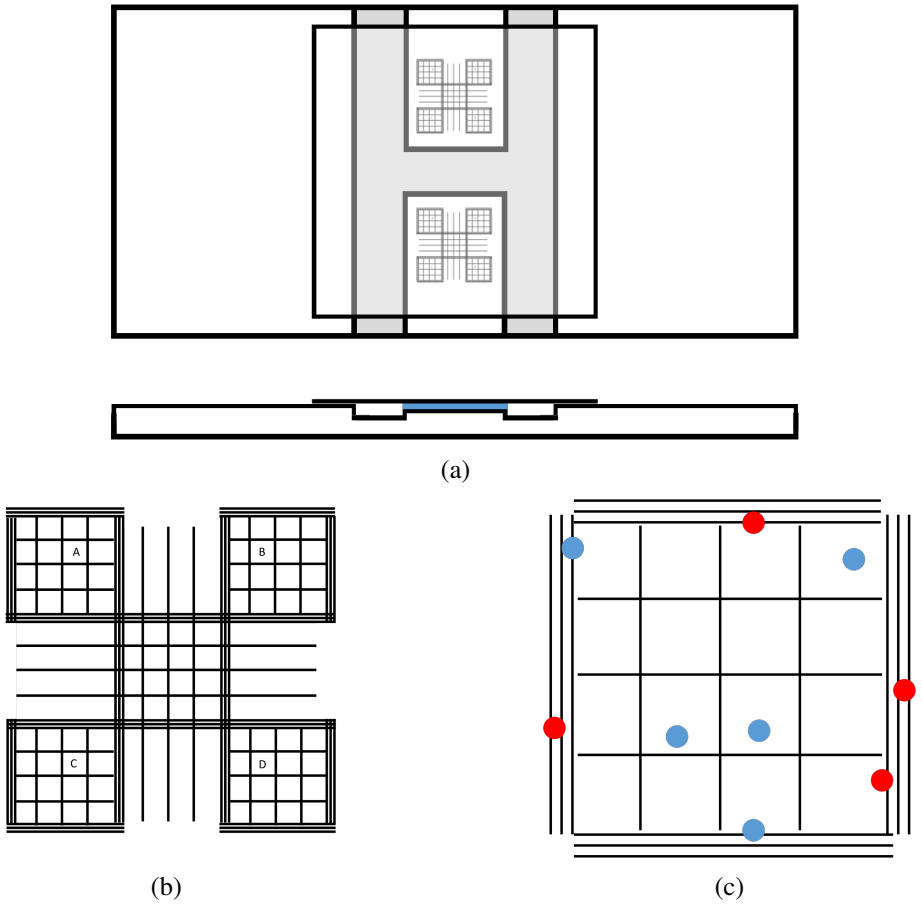

Figure 4.7: a) Schematic showing the layout of a haemocytometer chamber with a top-down view (*top*) and a side on view (*bottom*) with the area where the cells are loaded in shown in blue, b) Layout of one of the chambers with four different cell counting areas from which a mean can be extracted each region contains a volume of 100nL. c) Schematic showing the cell counting exclusion procedure according to the position of the cell within each region (shown in figure 4.7b as the regions labelled a-d). Red are to be excluded from counting and the blue cells are to be added to the count. Two sides of the haemocytometer are chosen where the cells are to be counted if they are touching the borders marked by three lines, in the example given the left and the bottom are chosen.

Figure 4.7b shows in greater detail the grid shown in the top portion of figure 4.7a, each of the four regions labelled (A-D) are used in counting cells. Figure 4.7c shows in greater detail one of the regions mentioned; to ensure consistent counting, if cells are touching the edge of the region marked by three horizontal or vertical lines then two of the sides were chosen where the cells would be counted (shown in blue) and the remaining two sides are discounted (shown in red). If the cell isn't overlapping the counting region but is on the chosen sides where cells will be counted, then that cell isn't counted; this is shown as the far left red 'cell' in figure 4.7c.

The haemocytometer was prepared by wetting the corridors with ethanol and then sliding the

glass cover slip over the chambers. A small sample (10μL for routine tissue culture) of the cell suspension for which the density of cells was unknown was removed after thoroughly mixing to ensure that the concentration was accurate and not due to an artefact of where the sample was taken from.

This small sample is then mixed with trypan blue (10μL for routine tissue culture), which acts as a good marker for cell viability due to its ability to pass through the membrane of a dead cell and not that of a viable cell. It also acts to improve the contrast between the background and counting cells making counting easier for the user. The ratio of the volumes of trypan blue to cell suspension plays a role in determining total cell count through the dilution factor;

$$\text{Dilution Factor (DF)} = \frac{\text{V}_{\text{Trypan Blue}} + \text{V}_{\text{Cell Suspension}}}{\text{V}_{\text{Trypan Blue}}} \tag{4.5}$$

The diluted cell suspension was then added using the capillary effect to both chambers of the haemocytometer this should distribute the cells with a consistent density across the chamber. The cells were then counted in both chambers which were then compared against each other to ensure that the difference in count between the two chambers did not exceed twice the counting error ($\sqrt{n}$ where n is the population size) of either chamber. The average was then taken from all the chambers and then input into the equation for cell concentration (cells/mL);

$$\text{Cell Concentration} = \bar{x} * DF * 10^4 \tag{4.6}$$

Where $\bar{x}$ is the average cell count per region (see figure 4.7b), DF is the dilution factor (equation. 4.5) and the factor of 10^4 is applied to the equation to convert the measurement from 100nL per region to milliliters. This conversion allows for two main applications:

1. Cell Count Calculation: This enables the collection of data to determine the number of cells present within a given sample.
2. Experiment Preparation: Alternatively, it facilitates the preparation of a specific number of cells required for a particular experiment.

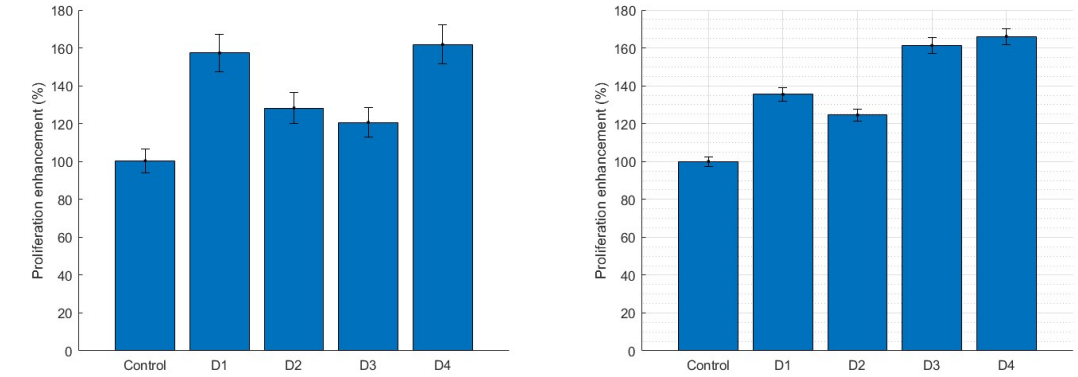

(a) (b)

Figure 4.8: Bar graphs showing the results from proliferation testing, the error bars arise from the counting error discussed in the section §4.2.3. a) two volts, b) three volts.

Proliferation testing

For testing the proliferation of the cells a variation on the above method is used. The cells were trypsinised in their respective wells with 10μL of trypsin until all of the cells were detached from the glass substrate; this volume allows for both full coverage of the wells and allows for reasonable cell density for counting with the haemocytometer. 20μL of trypan blue was then added to each of the wells and thoroughly mixed with the cells, this gives a dilution factor of 1.5 as per equation 4.5. Using equation 4.6, the concentration of cells can be determined and then scaled according to the total amount of cell suspension (30μL) to give a value of the number of cells in any given well.

4.3 Results and Discussion

4.3.1 Proliferation

Whether a cell dies, lives or thrives is a crucial measure of an outcome from any given treatment. To ascertain whether the stimulation profile is causing cell death or increasing the number of cells, the cell count is measured after stimulation. Figure 4.8, shows the results from the proliferation testing over a variety of powers. These results are normalised to the count of the control set with the error bars representing the standard counting error.

From Figure 4.8, it can be observed that with low power (2V and 3V) and devices proliferation is enhanced by the application of acousto-mechanical stimulation with a maximum enhancement of

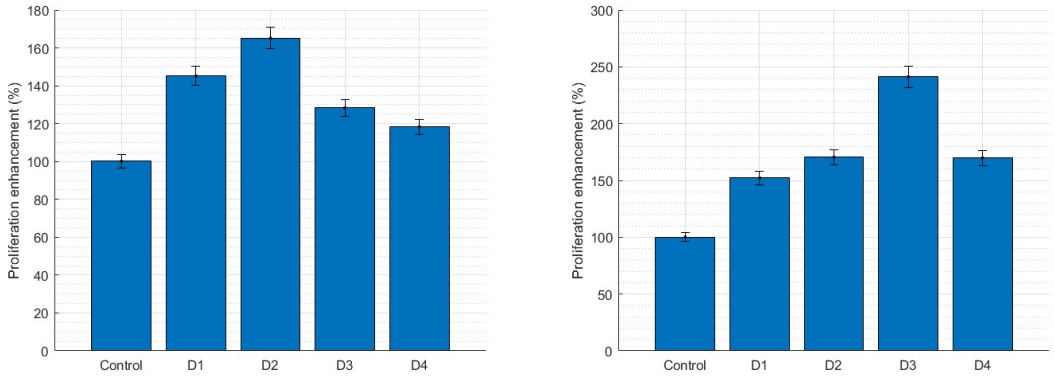

(a) (b)

Figure 4.9: Bar graphs showing the results from proliferation testing, the error bars arise from the counting error discussed in the section §4.2.3. a) five volts, b) seven volts.

166±3% above control (Device 4 3V) with the lowest enhancement being 120±7% above control (Device 3 2V). There are two contributing factors to the enhancement of proliferation through stimuli, one of which is the surface acoustic wave travelling along the superstrate which can be sensed by the cell and/or due to SAW's ability to induce streaming inside a liquid which can be utilised to ensure an even distribution of fresh media for the cells in addition to providing an additional method for dispersing extra-cellular messaging proteins can be transported from cell to cell.

Figure 4.9, shows a simular story to that of figure 4.8, with Device 3 showing the best increase in proliferation with a maximum enhancement of 241±9% above control when the applied potential to the SAW device is seven volts. Accross all devices it can be seen that there is an increase in the cell count for the 5V and 7V samples.

There are two exceptions to the conclusion that proliferation is enhanced through stimulation and both of these are contained within the experiment with the highest power. Device 1 shows a marked decrease in the number of cells when compared to control (having 83±3.75% the number of cells compared to control) which means rather than enhancing proliferation, the application of strong acousto-mechanical stimulation with these parameters is causing cell apoptosis; A possible mechanism for this can be seen with Device 2 which has the same design wavelength and a similar frequency as Device 1, however, has a much lower coupling coefficient (see Table 4.1 for details) meaning that Device 1 creates a more powerful SAW for a given input voltage.

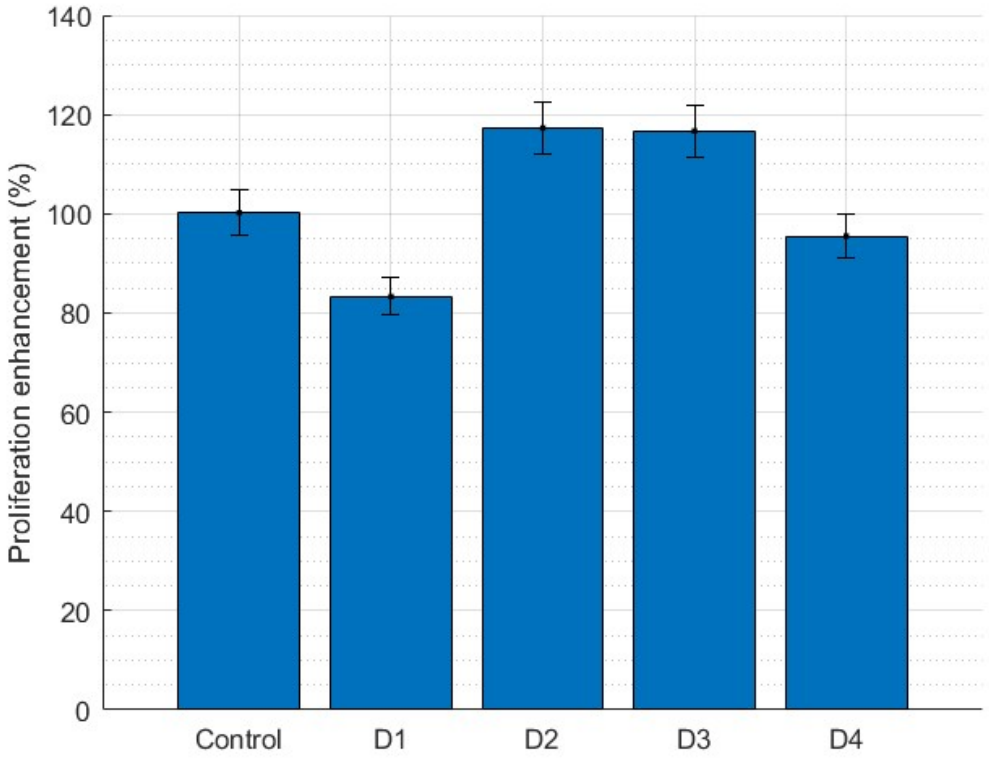

Figure 4.10: A bar graph showing the results from proliferation testing at nine volts, the error bars arise from the counting error discussed in the section §4.2.3.

It is observed from Figure 4.8 that Device 2 has an enhanced proliferation at 9V compared to Device 1 which lends itself to the hypothesis that Device 1 at this higher power is causing cell death from the stronger acousto-mechanical stimulation. The other exception is with Device 4 at the same higher power, where there is no statistically significant difference between the control set and the stimulated set with $95 \pm 4.3\%$ of the cells compared to the control.

4.3.2 Mechanobiology

In this work, the cells are stimulated using the set-up in Figure 4.4, with an additional chamber for each set acting as control where there is no stimulation applied. After the stimulation profile is completed then the cells are probed according to the protocol laid out in §4.2.2.

Figure 4.11, shows an example of a force-curve obtained, it shows a flat portion on the extension portion, followed by an increase in the force detected when the cell is indented before reaching its maximum and retracting. It can be noted that the retraction portion of the graph doesn't follow

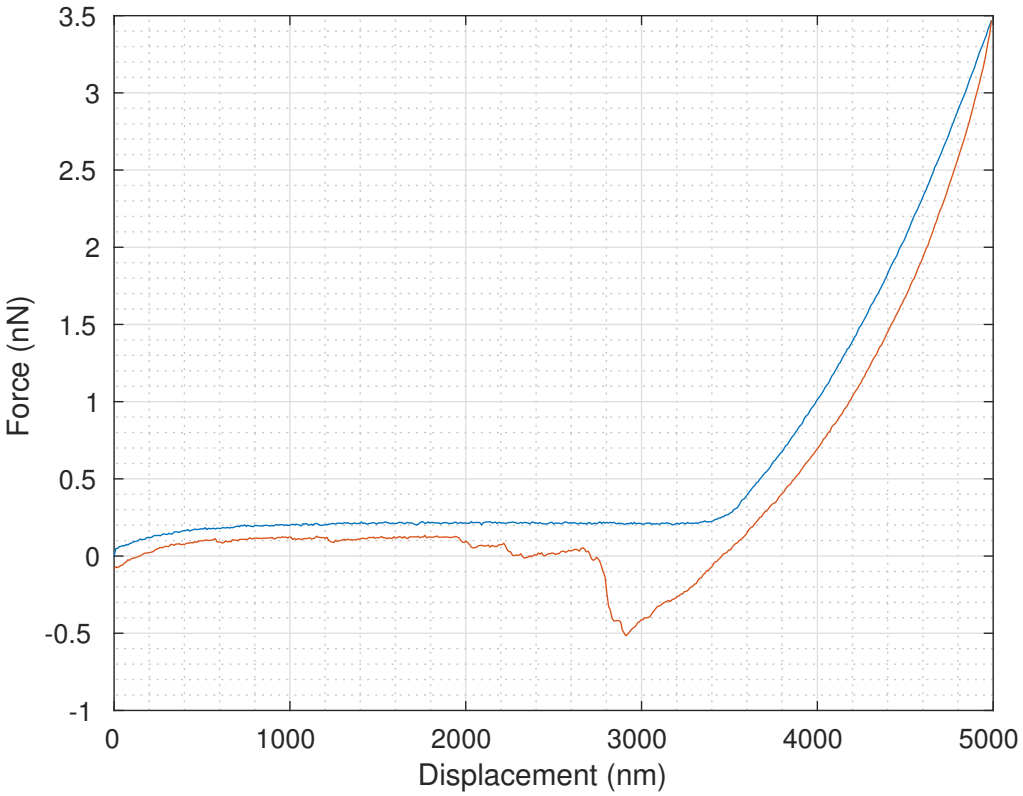

Figure 4.11: An example force curve taken from the 5V control dataset with a 5μm ramp, the two lines are the; extension (blue) and retraction (orange).

the same path as the extension portion, this is due to the viscous dampening where a portion of the energy put into the system is lost. Further along the retraction portion, it can be seen that there is an unbinding event, where a molecule or protein has been picked up by the cantilever when it has indented upon the cell and as the cantilever retracts from the surface has been stretched until the bond has broken; the exact molecule/protein that has attached to the cantilever is unknown, however, this is a demonstration of the ability for AFM measure these binding/unbinding events.

Figure 4.12 presents another example of a obtained force-curve, differing in its presentation from the previous Figure 4.11, which demonstrates a force-curve in the time domain with respect to the piezo displacement. The y-axis represents the measured force, while the x-axis displays the time taken for the force measurements, centered around 0 seconds, which is defined as the point of maximum indentation. This presentation illustrates that the acquisition frequency is 1Hz.

It is important to determine accurately the point on the force curve where the cantilever has in-

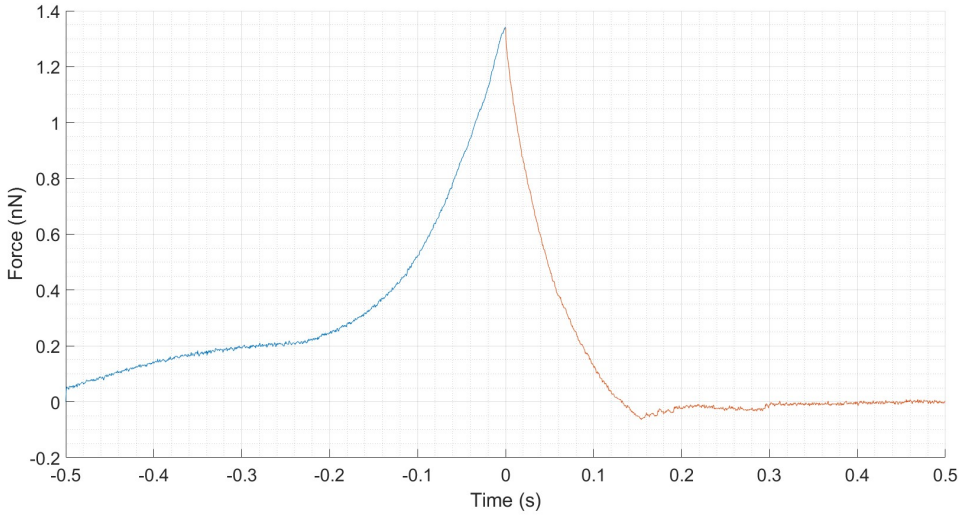

Figure 4.12: Graph showing an example force-curve in the time domain, centred around the point of maximum force

dented upon the cell. Figure 4.13, shows an extract of figure 4.11 with a variety of fitted curves, it can be seen that as the indentation point moves towards and past the true point of the indentation that the gradient of the curve increases and hence the measured Young's modulus is higher. This is demonstrated in figure 4.14, it can be seen that up until around 3050nm that there is virtually no measured Young's modulus data, as this is purely on the approach phase of the force-curve. From this point onwards it can be seen that there is an increase in the measured Young's modulus although this is not necessarily representative of the sample under investigation as the start point of the fitting may not be when the cantilever indents upon the sample but rather the data points extracted to fit the model could incorporate the indentation portion and thus observe a non-zero change in the gradient of the fitted graph. It can also be observed that the Goodness of Fit parameter (R^2) also is low at this point.

The chosen indentation point for this curve is selected to be about 3175nm, when comparing this point on figures 4.13 and 4.14, it can be observed that the fitted curve follows the curve of the data and has a high GOF value of (R^2 = 0.85) showing a strong positive correlation and the measured Young's modulus value is ($E_{\text{eff}} = 1.05$ kPa).

Each cell underwent repeated indentation, typically ranging from 100 to 200 times, utilizing a ramp size of 5μm. This approach was adopted to ensure that the cell's stiffness was not localized to a specific region and to evaluate the cell's response to the cantilever stimulation.

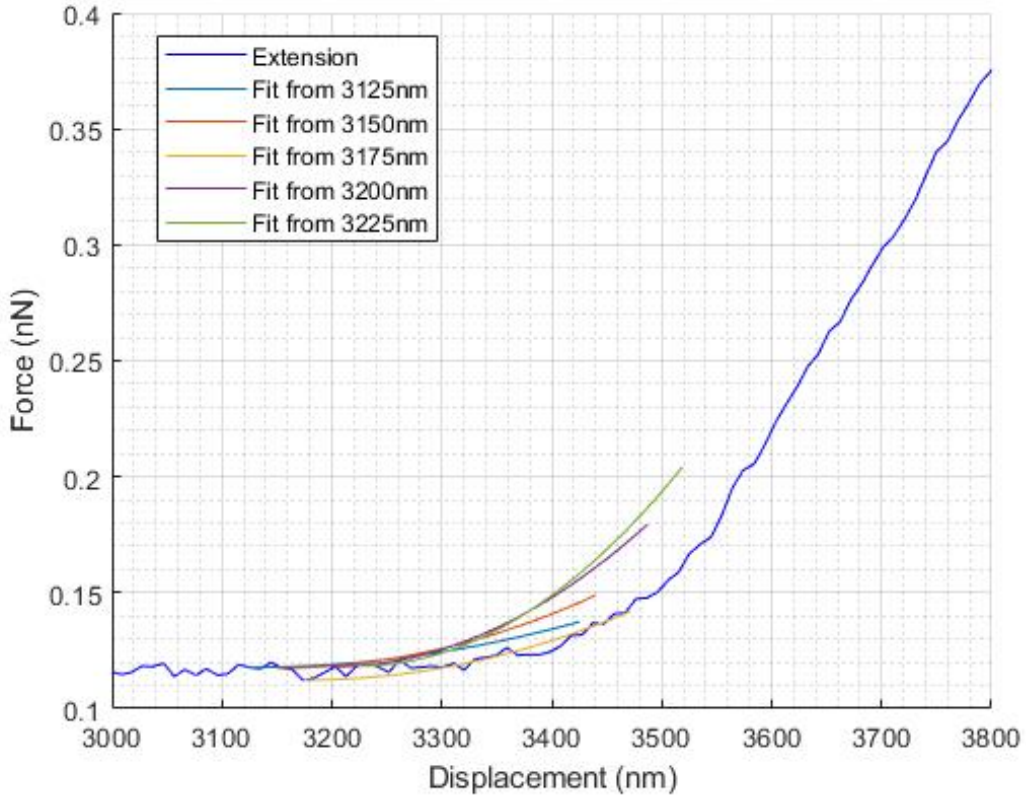

Figure 4.13: An extract of Figure 4.11 showing a variety of fitting points and their respective fitted curse overlaid, the curves were fitted using 300nm of indentation.

To minimize the impact of cell inhomogeneity, an offset of 100nm was introduced in either the x or y direction after every 20-30 force-curves. This offset repositioned the cantilever to an unstimulated region of the cell. This step was necessary because cells exhibit varying stiffness across their structure. Therefore, a single measurement wouldn't suffice to determine the cell's stiffness; instead, a distribution of stiffness values was compiled to provide a comprehensive insight into the properties of the cells under investigation.

Each force curve was then fitted using the aforementioned model which allows for a distribution of measured Young's moduli to be collated. Figure 4.15, is an example of one of the distributions obtained, these are fitted to a normal distribution, from which the average stiffness of the cell can be obtained along with the standard deviation of the stiffness measured.

Distributions of stiffnesses are generated from each cell probed throughout the experiment, and the distributions are overlaid to observe any differences between the control and the stimulated cells. Figure 4.16, shows two histograms for both control (*top*) and stimulated (*bottom*) cells;

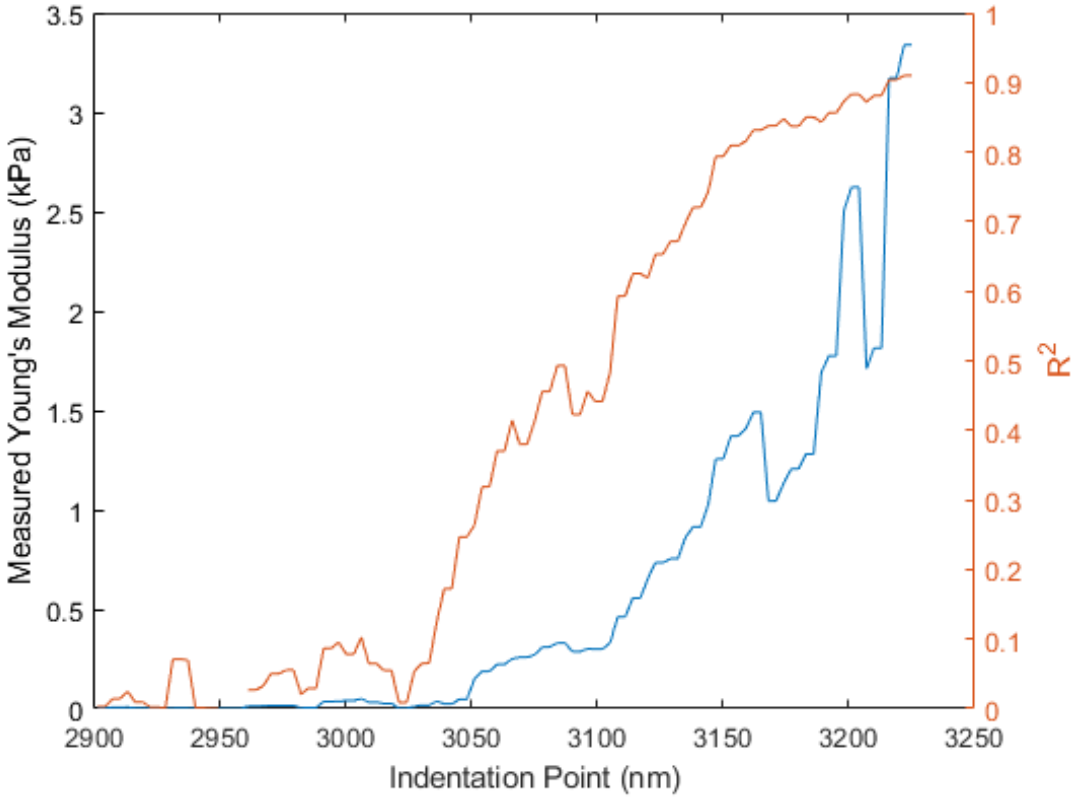

Figure 4.14: Graph showing the effect on the measured effective Young's modulus (E_{eff} in blue) and the Goodness of Fit parameter (R^2 in orange) when varying the chosen indentation point for fitting the model.

These cells were stimulated with Device 3 with an applied potential of 3V.

The aforementioned figure shows that the NHDF cells stiffen in response to the stimuli applied through SAW, with the vast majority of measured effective Young's moduli for the stimulated set being greater than that of control.

It can also be observed that when comparing the control set and the stimulated set that there is an increase in the mean value of Young's modulus in addition to the spread of Young's moduli measured on any one given cell.

The influence of acousto-mechanical stimulation on the stiffness of the cells becomes clearer when comparing the means of each of the cells measured. Figure 4.17, shows a box plot comparing the stiffnesses of stimulated cells at two different powers with the same device. It can be seen that the average effective Young's modulus of each data set is higher for stimulated cells than for their respective control.

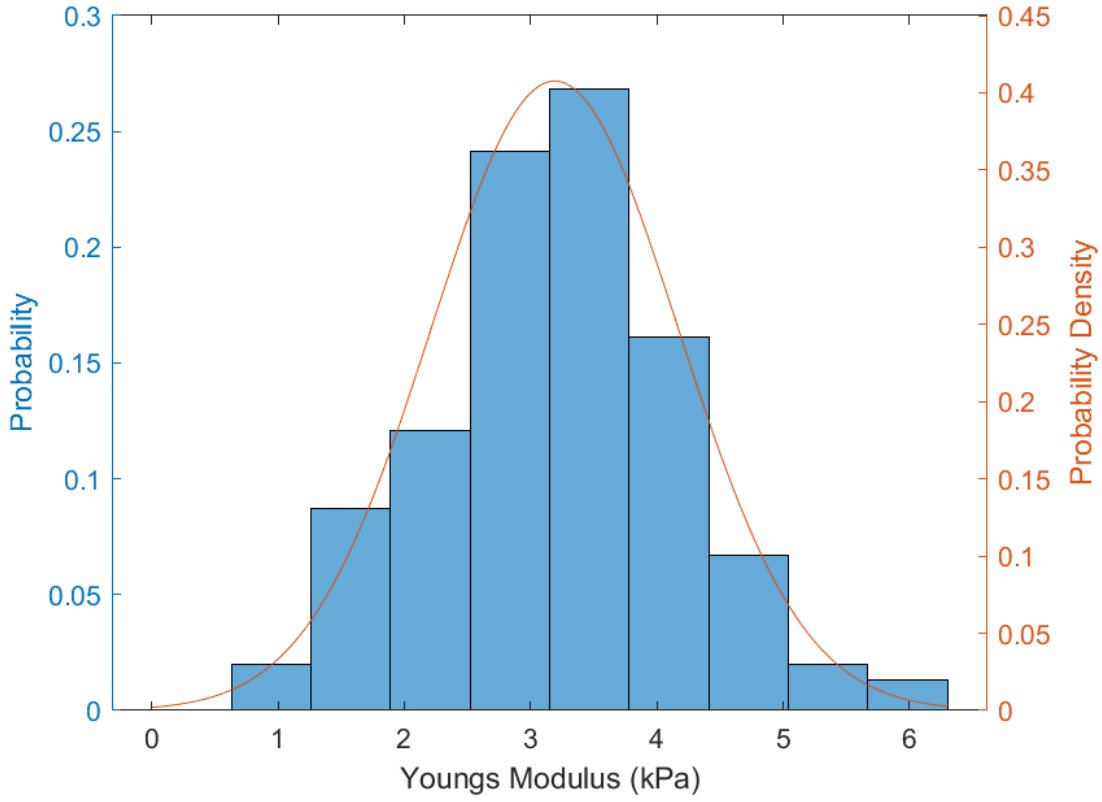

Figure 4.15: A representative histogram from the control dataset for the 3V 9.5MHz experiment, with the force-curve fitted with an average indentation value of 360.5nm. The graph also shows the fitted normal probability density function (orange), with an average stiffness of 3.19kPa with a standard deviation of 0.98kPa (n=148).

For the 9.5MHz 3V experiments there is an increase in the mean effective Youngs modulus of 2.7kPa from an average cell stiffness of 4.2kPa for the control experiment to an average cell stiffness of 6.9kPa for the stimulated cells. This is a stiffness increase of 64% above control.

For the 9.5MHz 3V experiments there is an increase in the mean effective Youngs modulus of 8.0kPa from an average cell stiffness of 7.6kPa for the control experiment to an average cell stiffness of 15.6kPa for the stimulated cells. This is a stiffness increase of 106% above control.

Although there is a difference between the control sets (3V compared to 5V), it is important not to make a comparison here and only compare between sets of experiments as there will be great variability due to a variety of factors with two major ones being; passage number and different cantilevers with spring constants and tip radii can be different even between cantilevers in the same box (te Riet et al., 2011) with the force curves fitted using the nominal values given by the manufacturer although there is a great variety of calibration methods available including; reference

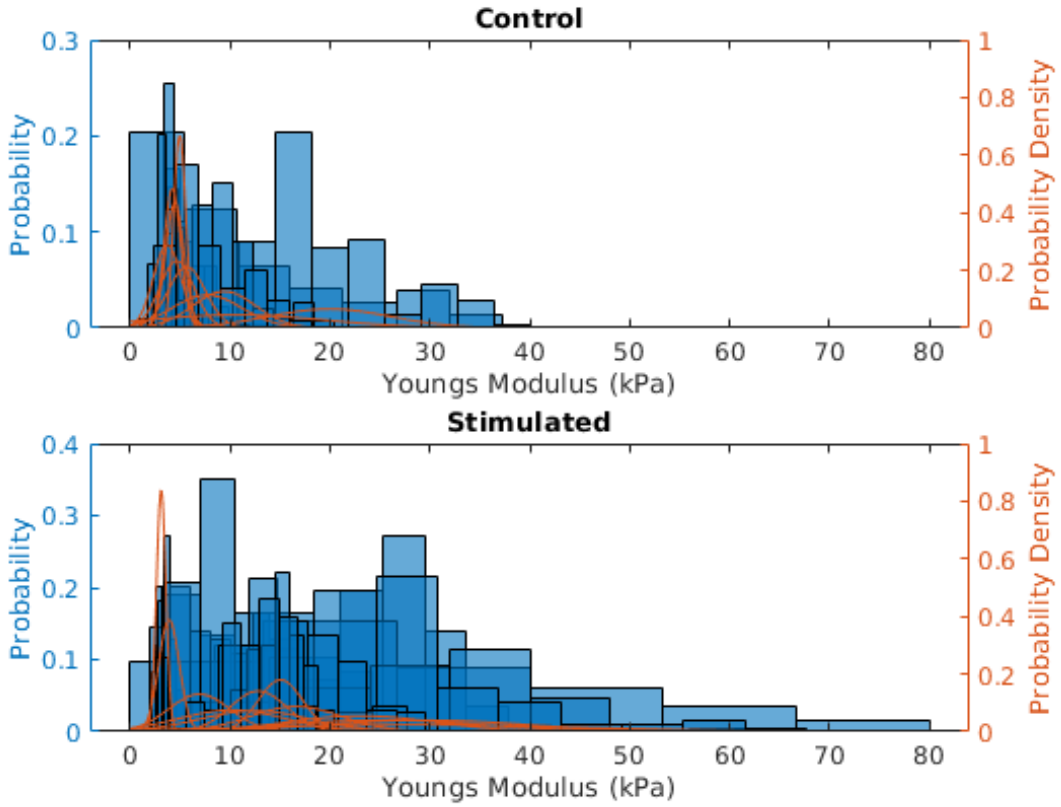

Figure 4.16: A comparison of stiffness between the control cells (*top*) and stimulated cells (*bottom*) from Device 3 with a potential of 5V applied.

cantilevers (Gates and Reitsma, 2007), thermal noise (Hutter and Bechhoefer, 1993), added mass method (Cleveland et al., 1993) and Sader method (Sader et al., 1998).

Comparisons, however, can be made between the respective control and stimulated cell sets because for these experiments the same cantilever is used for probing both the control and stimulated cells which means that the spring constant of the cantilever will not change. Additionally, the control and stimulated cells come from the same passage number.

4.4 Summary

In this chapter, the effect of acousto-mechanical stimulation has been explored using a case study of Normal Human Dermal Fibroblasts with their proliferative and mechanical properties tested. It has been shown that by applying SAW-based stimulation to NHDF cells that their proliferative properties can be enhanced although the careful selection of these parameters is required otherwise cell apoptosis can be induced at higher powers with Device 1 showing a decrease in cell count to

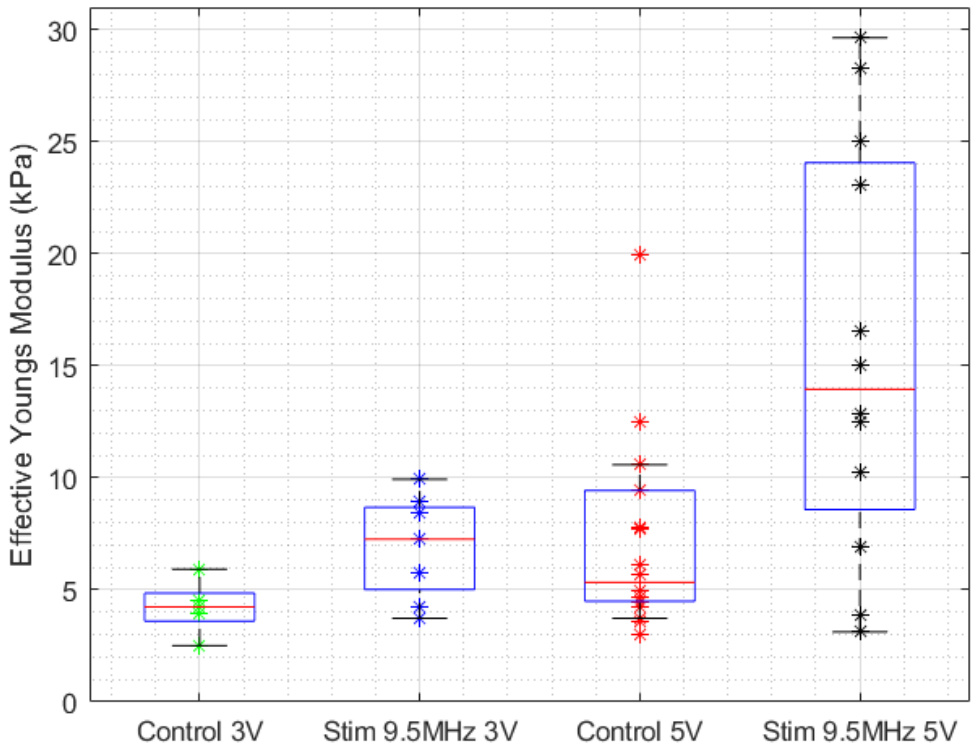

Figure 4.17: Box plot showing the differing distribution of Effective Young's Moduli between control cells and stimulated cells. Each $\star$ represents the mean effective Young's Modulus of a cell within that set with the red line representing the mean effective Young's Modulus of all cells within the set. (Control 3 n=5 (average of 152 FCs per cell), stimulated 9.5MHz 3V n=8 (Average of 150 FCs per cell), Control n=10 (average of 153 FCs per cell), stimulated 9.5MHz 5V n=12 (Average of 144 FCs per cell))

83% of control at the maximum applied power. The maximum proliferation observed across all powers and devices was observed to be 241% above control with Device 3 at seven volts.

Furthermore, the findings show that in response to stimulation, the cells undergo a substantial increase in stiffness. This marked change is quantified by an elevation in the effective Young's modulus, ranging between 64% and 106% when compared to control experiments.

Chapter 5

Conclusions and Further Work

5.1 Conclusion

This thesis presents research for the integration of Atomic Force Microscopy to probe the effects of the stimulation of cells through acousto-mechanical stimulation. Using a case study of Normal Human Dermal Fibroblasts, it has been demonstrated that they respond to acousto-mechanical stimulation in two primary manners; an increase in proliferation and an increase in cell stiffness.

Proliferation was investigated (See §4.3.1) to measure whether the cells remained viable and at which point the stimulation could start causing cell death, if at all. In this work, the cells responded positively to the stimulation and would proliferate more as a consequence, with a peak of $240\pm10\%$ enhancement compared to the control set. However, it was found that after a specific power, the stimulation effect would cause cell death or stagnation of the population where there would be no net increase above control.

The stiffness of cells when acousto-mechanical stimulation was applied was also investigated (See §4.3.2) as a measure of the extent the cells' mechanical properties might change in response to stimulation.

In chapter 3, a variety of surfaces were characterised to investigate what changes occur as a result of surface functionalisation of Bacterial cellulose with BslA with and without a cellulose binding domain; it was found that adding BslA to the BC resulted in a change in the RMS roughness of the

surface with the BslACBM samples showing greater consistency in the coating of the BC fibres. To investigate hierarchical structures, investigations of silica micro-particles and nano-particles were investigated (§3.3.3) with the micro-particle structure visible underneath the layers of nano-particles.

5.2 Further Work

The following future work has been proposed;

- With an established protocol for the stimulation of cells using SAW, it would be possible to expand this work to include more cell lines in the future. Of particular interest would be cell lines which are well noted for their mechanical response, or rarer cell lines, for which looking at the response of cells to external forces is difficult either due to differentiation from applied stimulation or an inability to proliferate at speed. These cell lines could include; myoblasts, Osteoblasts, cardiomyocytes, and patient-derived SSc fibroblasts, as well as expanding this work to include suspended cells, including bacteria.
- To supplement upon the work in Section §4.3.2, additional tools of AFM could be utilised, for example, taking Force-volume images, which would be able to combine a topographic map of the sample along with measuring elasticity changes creating a heat-map of Young's moduli which can be overlaid on the topography to identify which regions of the cell exhibit stiffening when acousto-mechanical stimulation is applied and whether this is a global phenomenon for the whole cell or if it is localised to specific regions of the cell. Localisation can be assisted by utilising regular tapping mode topographic scans whilst looking at the phase to see if any structural changes can be observed between stimulated against unstimulated cells.
- Additionally, varying the frequency of indentation would reveal in greater detail in investigating the dynamic modulus of the cells. This could be achieved using a standard force-curve acquisition protocol (as laid out in §4.2.2) but with the operator acquiring force-curves using a variety of frequencies.
- To improve the work outlined in Chapter 4, the stimulation profile could be changed to allow for sequential stimulation. (I.e. Stimulate Device 1 for 1 minute, then Device 3 for 1 min,

then Device 4 for 1 minute, wait for 2 mins and then repeat).

- To supplement the work in Chapter 4, a series of images could be taken using confocal microscopy to look at changes in structural protein composition immediately after stimulation; proteins of interest could include F-Actin. This could be combined with AFM if live-cell stains are used, allowing for a combination of Bright-field, florescence, topographic and mechanical correlative data acquisition with the identification of particular regions of interest identifiable. This would allow for longer-term experiments as the cells could be held at physiologically relevant conditions.
- Mechanical properties of stimulated fibroblasts were studied in this research, with one avenue explored for a biological reason for the enhancement of proliferation and stiffness of the fibroblasts. Further work could measure whether the acousto-mechanical stimulation increases cytokines such as TGF-β which serves as a critical player in cell proliferation, differentiation and apoptosis (Kubiczkova et al., 2012); if an increase in TGF-β is observed, then both inter- and intra-cell signalling plays a crucial role in increased proliferation.
- Additionally, to determine the dominant signalling mechanism, gene knockout using CRISPR can be used to knock out/down the expression of Yap/Taz and then study the effect of acousto-mechanical stimulation on the cells. This would validate or point in a different direction for a dominant intra-cellular signalling mechanism.

Appendix A

Force-curve analysis GUI code

```
SpringConstant=str2double(get(handles.SpringCon,'String'
   ));
DeflectSens=str2double(get(handles.DeflectSens,'String')
   );
extenddata(:,2)=extenddata(:,2)*SpringConstant*
   DeflectSens;
retractdata(:,2)=retractdata(:,2)*SpringConstant*
   DeflectSens;
axes(handles.curveaxis);
plot(extenddata(:,1),extenddata(:,2),'b-',(max(
   retractdata(:,1))-retractdata(:,1)),retractdata(:,2),
   'r-')
grid on
grid minor
xlabel('Displacement (nm)')
ylabel('Force (nN)')
z_ext=extenddata(:,1);
v_ext=extenddata(:,2);
z_ret=retractdata(:,1);
z_ret=z_ret(end:-1:1);
```

```
v_ret=retractdata(:,2);


F_ext=v_ext*SpringConstant*DeflectSens;
%F_ret=v_ret*SpringConstant*DeflectSens;
[x,~]= ginput (2);
z_start=x(1);
z_end=x(1)+(6)*7;
%low_ind=ceil(mean(find(extenddata(:,1)>z_start*0.99&
   extenddata(:,1)<z_start*1.01)));
%high_ind=ceil(mean(find(extenddata(:,1)>z_end*0.99&
   extenddata(:,1)<z_end*1.01)));
%cont_ind=ceil(mean(find(z_ext>x(2)*0.99&z_ext<x(2)
   *1.01)));
YoungsMod=zeros(6,4);
FA=str2double(get(handles.FA,'String'));
nu=str2double(get(handles.nu,'String'));
for i=1:6
z_end=x(1)+(i+3)*100;
%limiting the f-d curve
%low_ind=ceil(mean(find(extenddata(:,1)>z_start*0.99&
   extenddata(:,1)<z_start*1.01)));
high_ind=ceil(mean(find(extenddata(:,1)>z_end*0.99&
   extenddata(:,1)<z_end*1.01)));
cont_ind=ceil(mean(find(z_ext>x(2)*0.99&z_ext<x(2)*1.01)
   ));
%disp(cont_ind-low_ind);
%z_ext_zoom=extenddata(low_ind:high_ind,1);
%F_ext_zoom=extenddata(low_ind:high_ind,2);
z_analyse=z_ext(cont_ind:high_ind)-z_ext(cont_ind);
F_analyse=F_ext(cont_ind:high_ind)-F_ext(cont_ind);
```

```
indentation=z_analyse-F_analyse/SpringConstant;
%inde(i)=max(indentation(i));
%indentation(i)=z;
axes(handles.fitaxis)
cla reset
grid on
hold on
plot(indentation*10^(-9),sqrt(F_analyse*10^(-9)),'b*')
try
[f,gof2]=fit(indentation*10^(-9),sqrt(F_analyse*10^(-9))
   ,'poly1');
catch
end
plot(f,indentation*10^(-9),sqrt(F_analyse*10^(-9)))
legend('off')
hold off
%ci(1,1)
%ci(2,1)
%plot(f)
% axis([-inf inf min([min(extenddata(:,2)) min(
   retractdata(:,2))]) max([max(extenddata(:,2)) max(
   retractdata(:,2))])])
axes(handles.zoomaxis)
grid on
hold on
plot(indentation,F_analyse,'b*',indentation,(f.p1*(
   indentation*10^(-9/2))).^2,'-')
xlabel('Displacement (nm)')
ylabel('Force (nN)')
xlim([0 900])
```

```
legend('off')

ci=confint(f,0.95);
disp(f.p1)
low=(sqrt(2)*(1-nu^2)*ci(1,1)^2)/tan(deg2rad(FA(1)));
high=(sqrt(2)*(1-nu^2)*ci(2,1)^2)/tan(deg2rad(FA(1)));
YM=(sqrt(2)*(1-nu^2)*f.p1^2)/tan(deg2rad(FA(1)));
YoungsMod(i,:)=[max(indentation) YM mean([abs(YM-low)
    abs(YM-high)]) gof2.rsquare];

end

minerrdata=[YoungsMod(1,1) YoungsMod(1,2) YoungsMod(1,3)
     YoungsMod(1,4);YoungsMod(2,1) YoungsMod(2,2)
    YoungsMod(2,3) YoungsMod(2,4);YoungsMod(3,1)
    YoungsMod(3,2) YoungsMod(3,3) YoungsMod(3,4);
    YoungsMod(4,1) YoungsMod(4,2) YoungsMod(4,3)
    YoungsMod(4,4);YoungsMod(5,1) YoungsMod(5,2)
    YoungsMod(5,3) YoungsMod(5,4);YoungsMod(6,1)
    YoungsMod(6,2) YoungsMod(6,3) YoungsMod(6,4);];
num2clip(minerrdata);


set(handles.YoungTab,'data',minerrdata);

set(handles.aveerr,'String',strcat('R^2 AVE =',num2str(
    mean(YoungsMod(:,4)))))
set(handles.minerr,'String',strcat('R^2 Max =',num2str(
    max(YoungsMod(:,4)))))
disp('Fit complete')
```

```
        hold off
```

Appendix B

Supplementary AFM Images

B.1 Bacterial Cellulose

Empty Vector

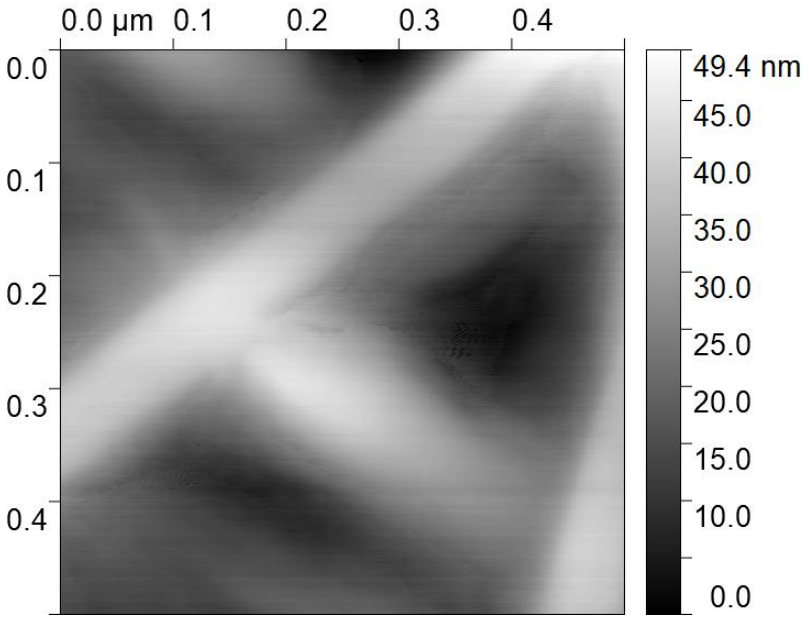

Figure B.1: 0.5 μm by 0.5 μ scan of Empty Vector Bacterial cellulose.

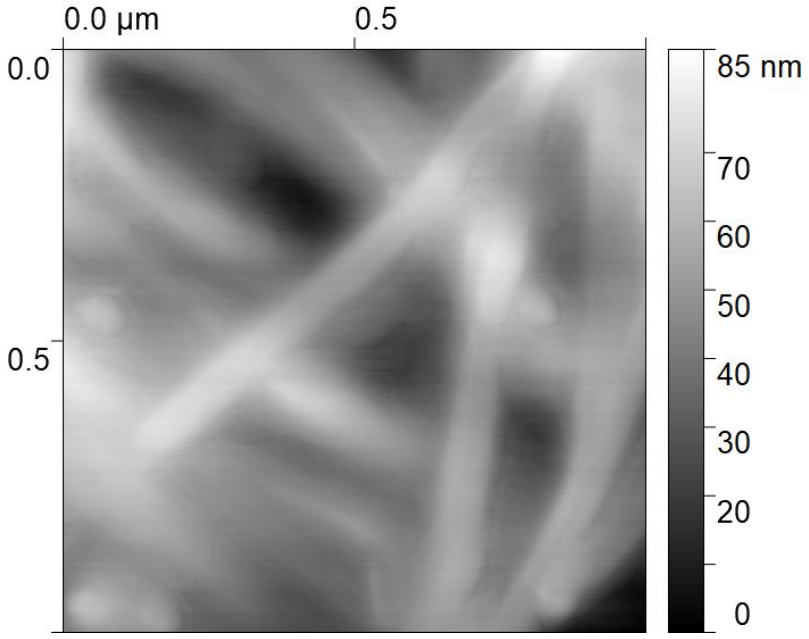

Figure B.2: 1 μm by 1 μm scan of Empty Vector Bacterial cellulose.

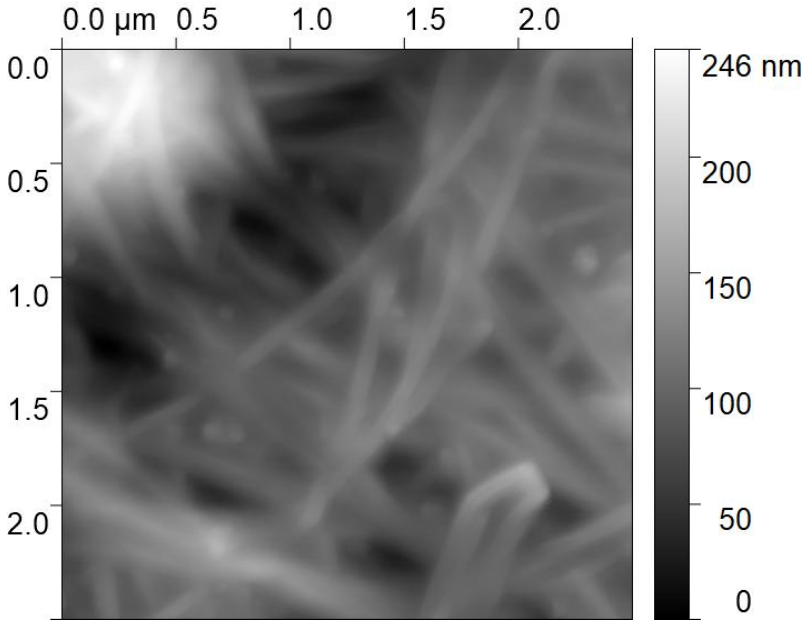

Figure B.3: 2.5 μm by 2.5 μm scan of Empty Vector Bacterial cellulose.

B.2 Anti-viral surfaces

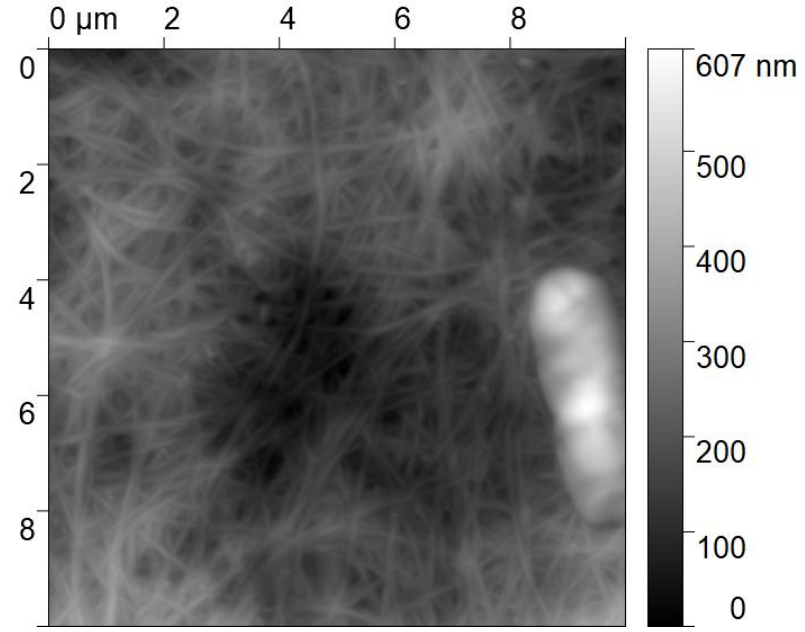

Figure B.4: 10 μm by 10 μm scan of Empty Vector Bacterial cellulose.

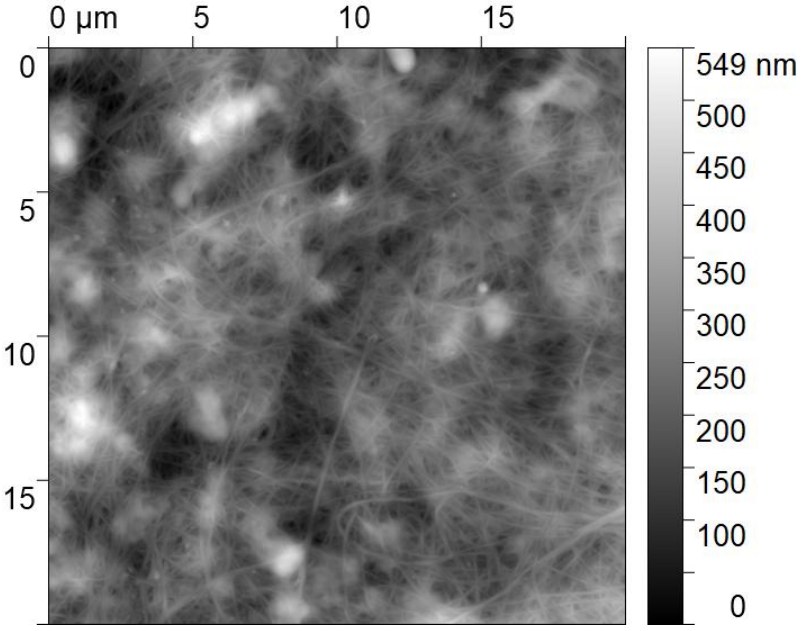

Figure B.5: 20 μm by 20 μm scan of Empty Vector Bacterial cellulose.

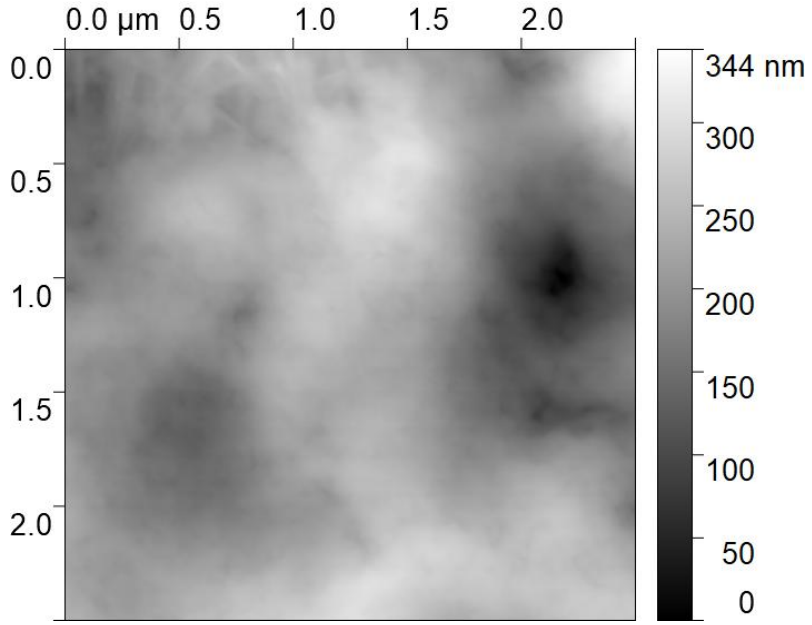

Figure B.6: 2.5 μm by 2.5 μm scan of Bacterial cellulose functionalised with 50μg/mL BslA without CBM.

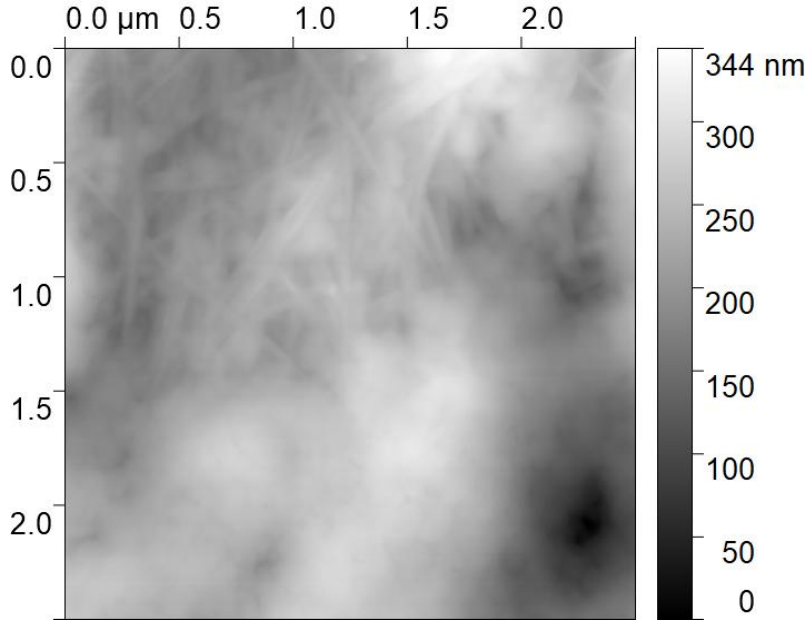

Figure B.7: 2.5 μm by 2.5 μm scan of Bacterial cellulose functionalised with 50μg/mL BslA without CBM.

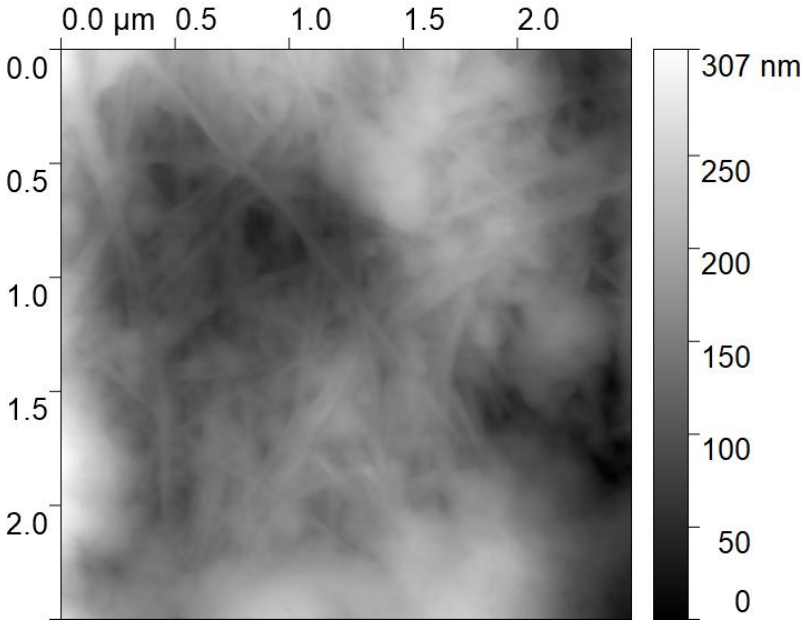

Figure B.8: 2.5 μm by 2.5 μm scan of Bacterial cellulose functionalised with 50μg/mL BslA without CBM.

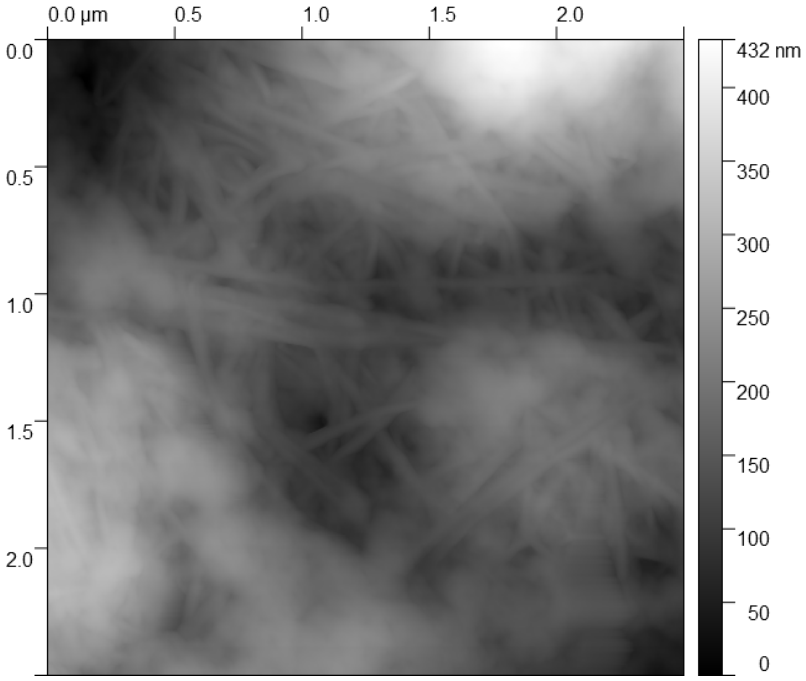

Figure B.9: 2.5 μm by 2.5 μm scan of Bacterial cellulose functionalised with 50μg/mL BslA without CBM.

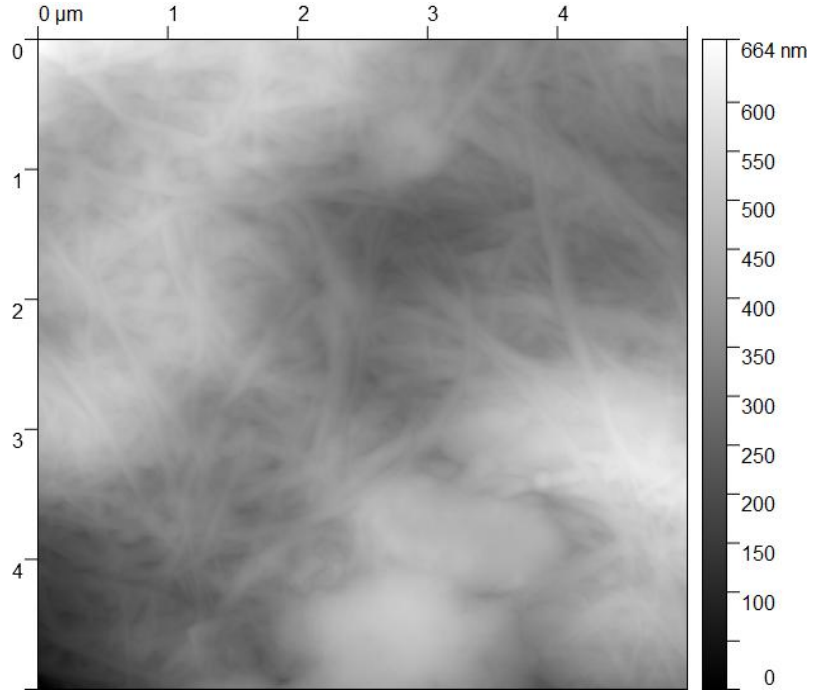

Figure B.10: 5 μm by 5 μm scan of Bacterial cellulose functionalised with 250μg/mL BslA without CBM.

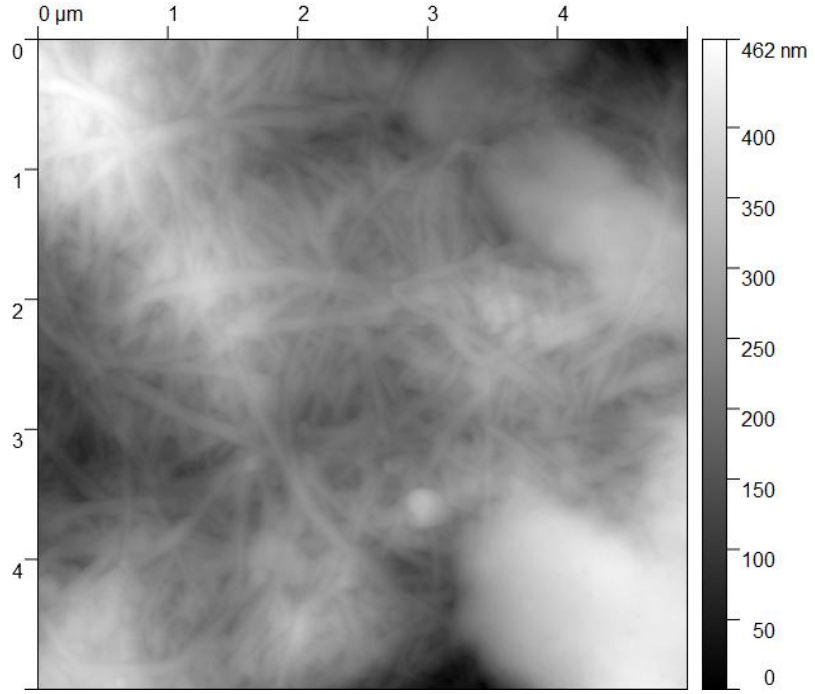

Figure B.11: 5 μm by 5 μm scan of Bacterial cellulose functionalised with 250μg/mL BslA without CBM.

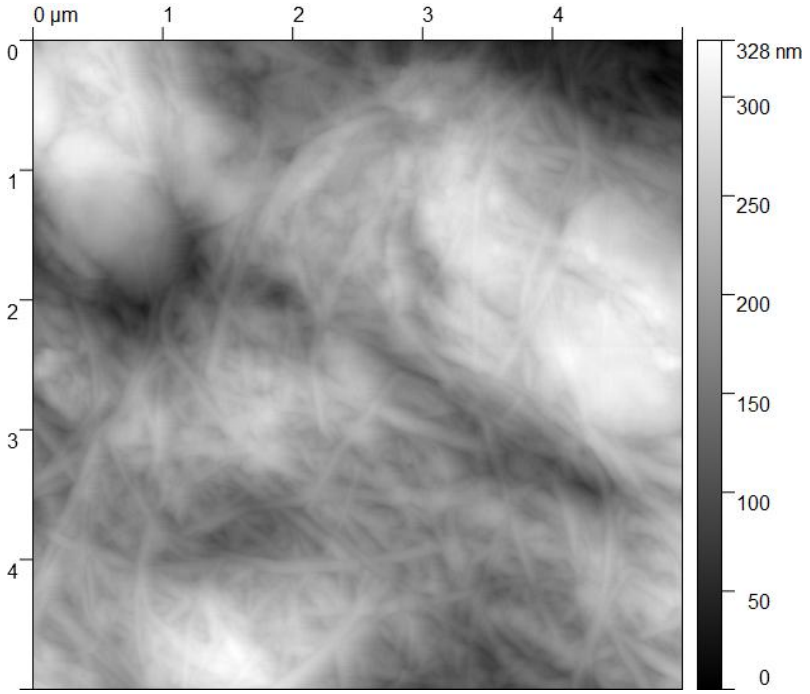

Figure B.12: 5 μm by 5 μm scan of Bacterial cellulose functionalised with 250μg/mL BslA without CBM.

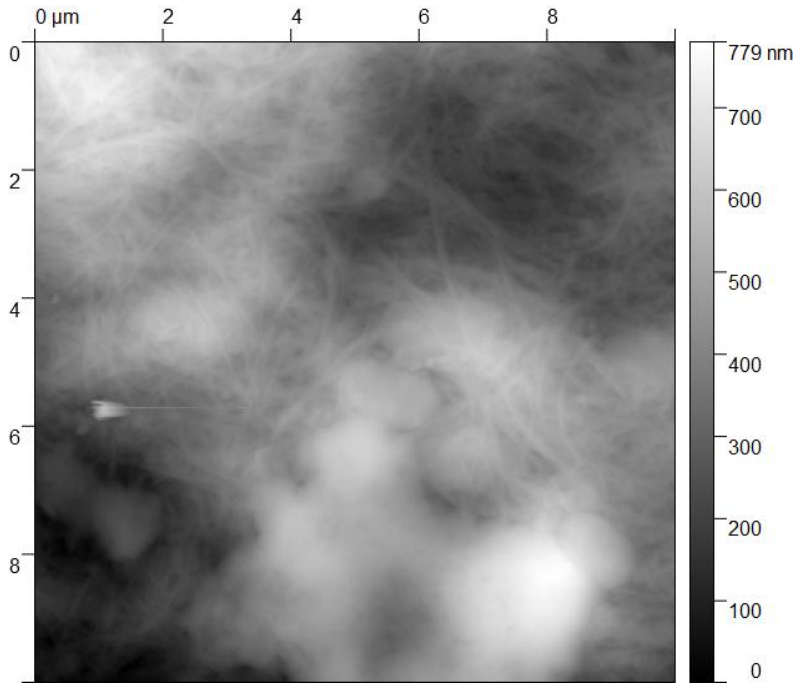

Figure B.13: 10 μm by 10 μm scan of Bacterial cellulose functionalised with 250μg/mL BslA without CBM.

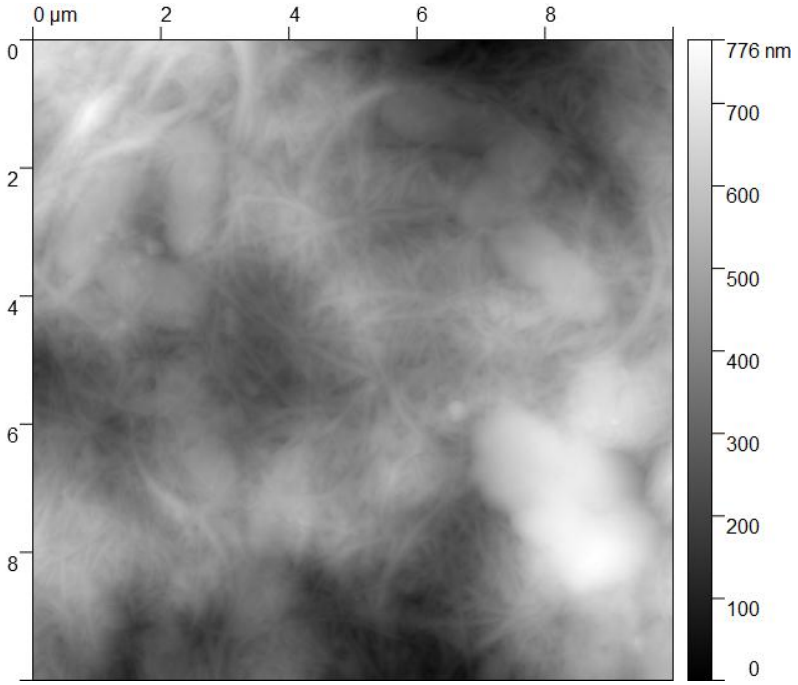

Figure B.14: 10 μm by 10 μm scan of Bacterial cellulose functionalised with 250μg/mL BslA without CBM.

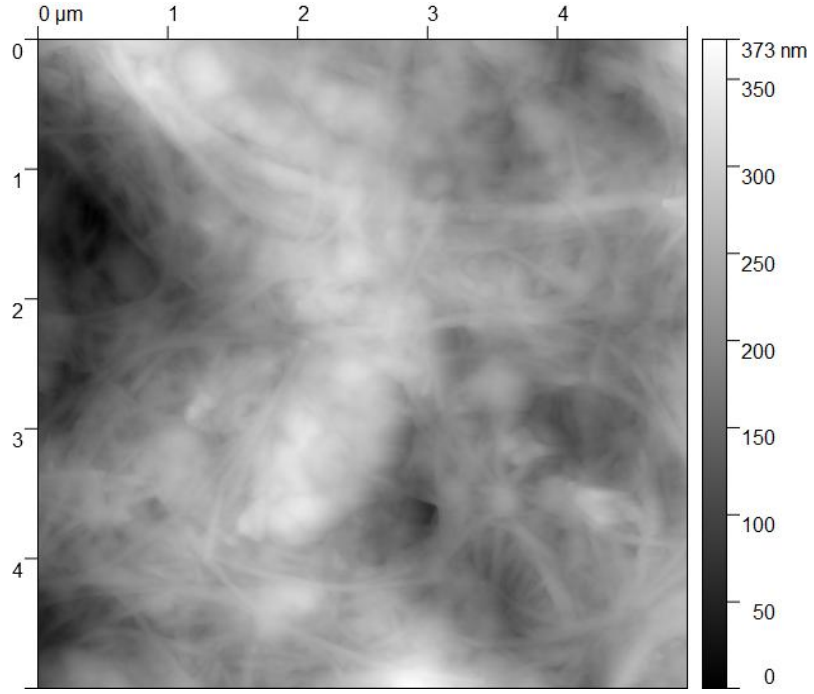

Figure B.15: 5 μm by 5 μm scan of Bacterial cellulose functionalised with 500μg/mL BslA without CBM.

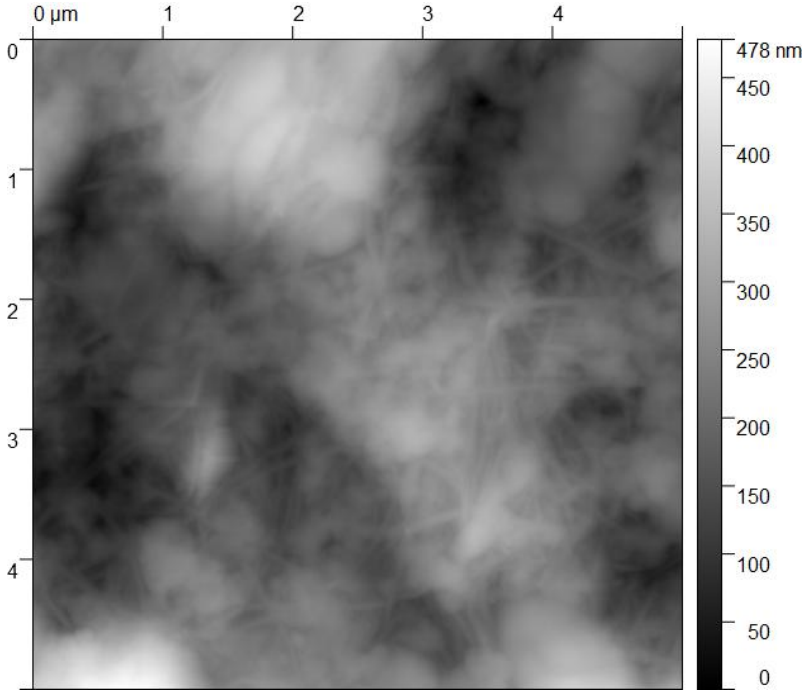

Figure B.16: 5 μm by 5 μm scan of Bacterial cellulose functionalised with 500μg/mL BslA without CBM.

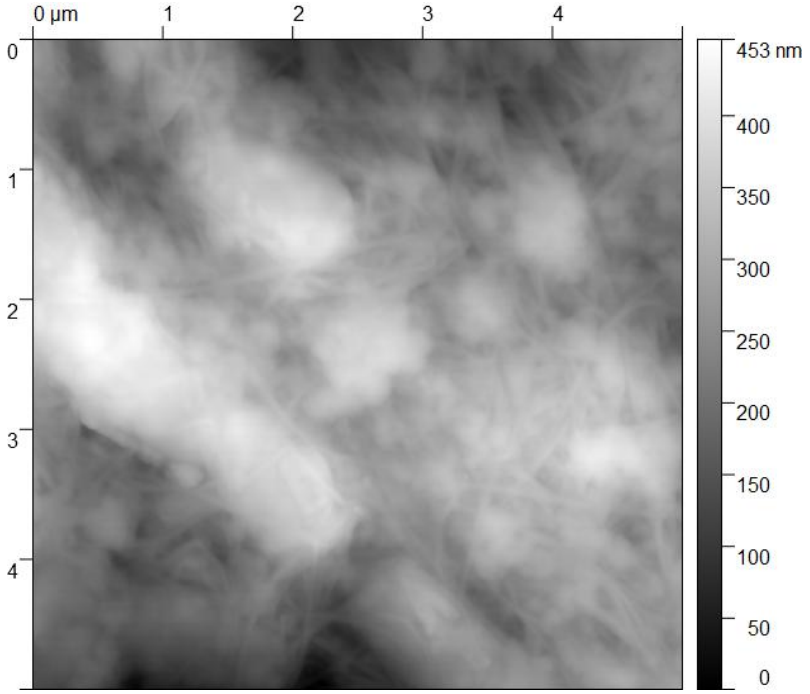

Figure B.17: 5 μm by 5 μm scan of Bacterial cellulose functionalised with 500μg/mL BslA without CBM.

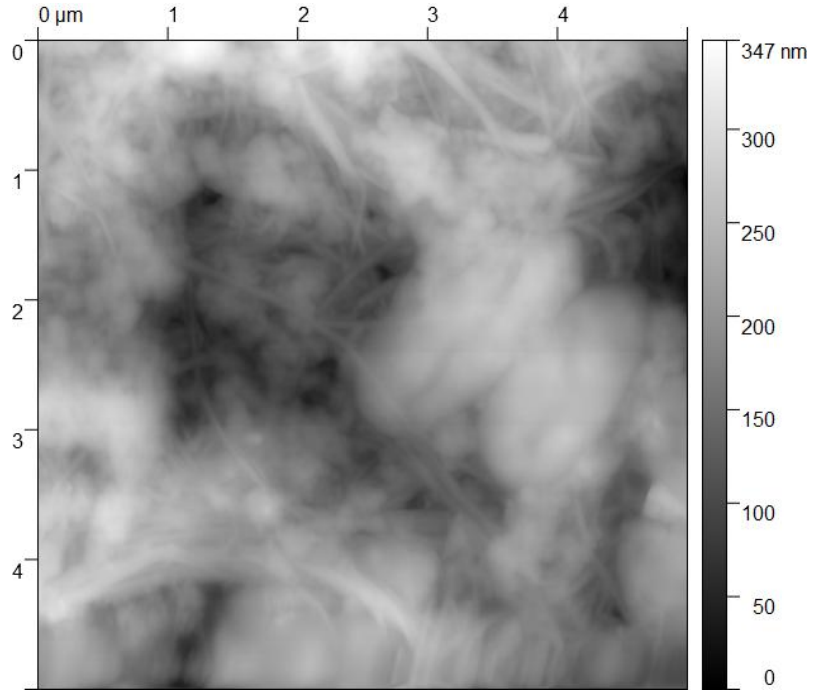

Figure B.18: 5 μm by 5 μm scan of Bacterial cellulose functionalised with 500μg/mL BslA without CBM.

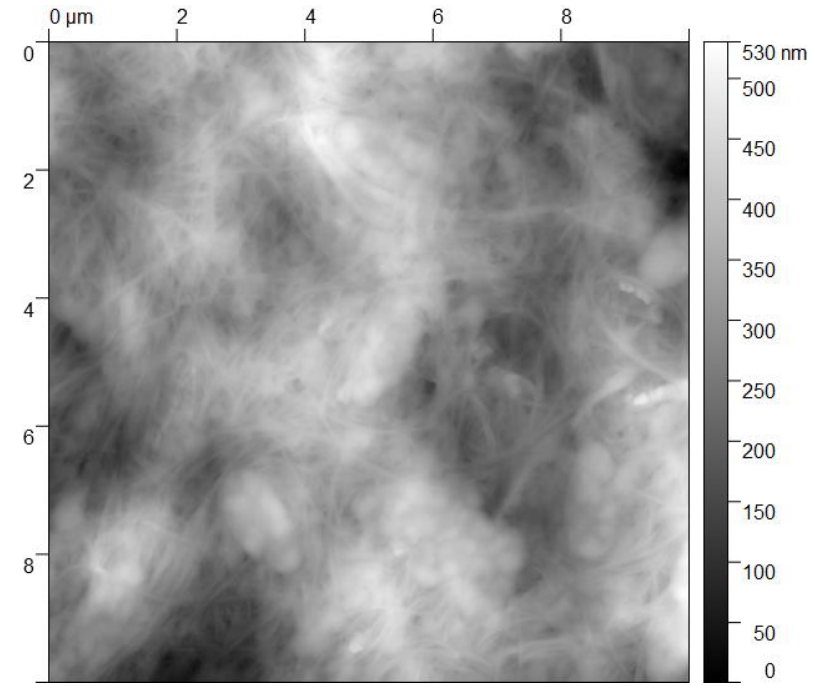

Figure B.19: 10 μm by 10 μm scan of Bacterial cellulose functionalised with 500μg/mL BslA without CBM.

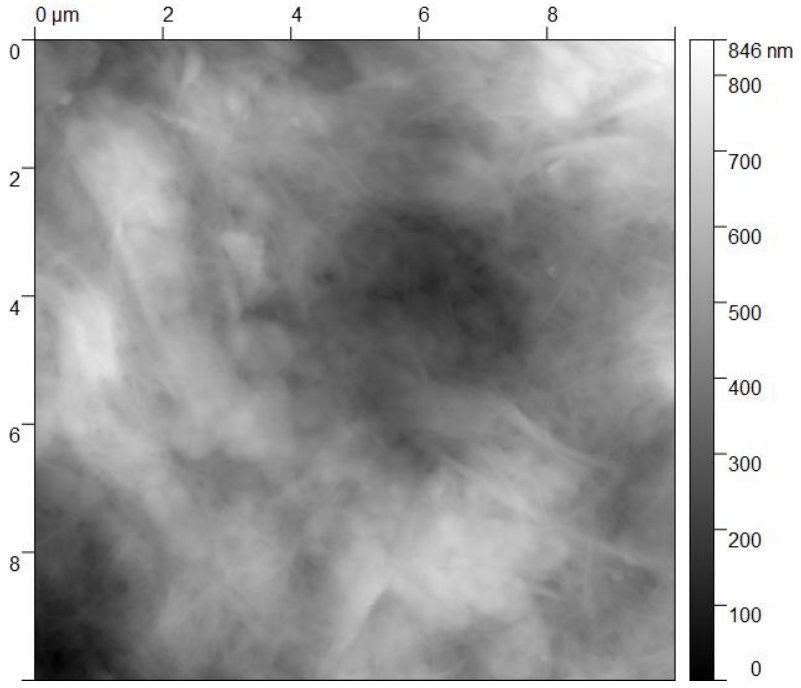

Figure B.20: 10 μm by 10 μm scan of Bacterial cellulose functionalised with 500μg/mL BslA without CBM.

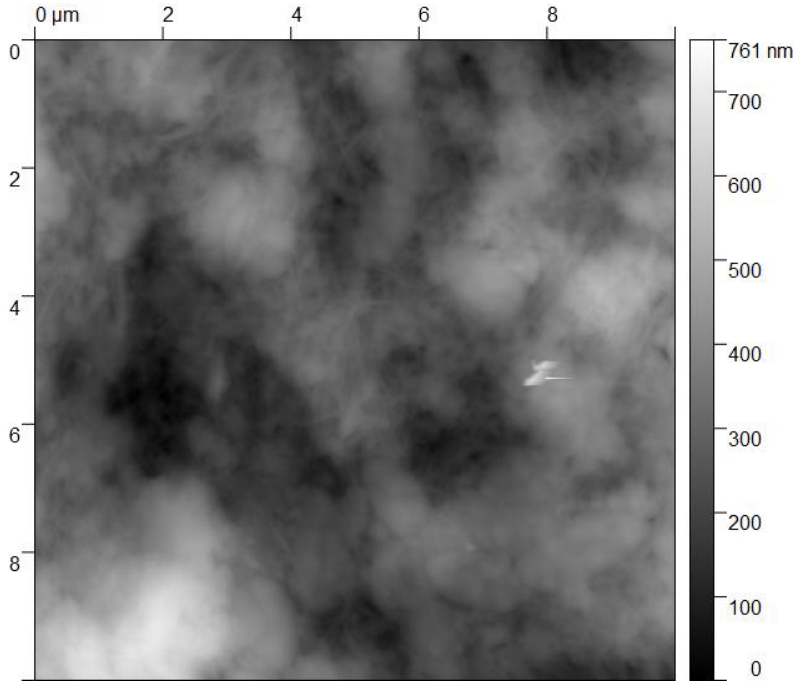

Figure B.21: 10 μm by 10 μm scan of Bacterial cellulose functionalised with 500μg/mL BslA without CBM.

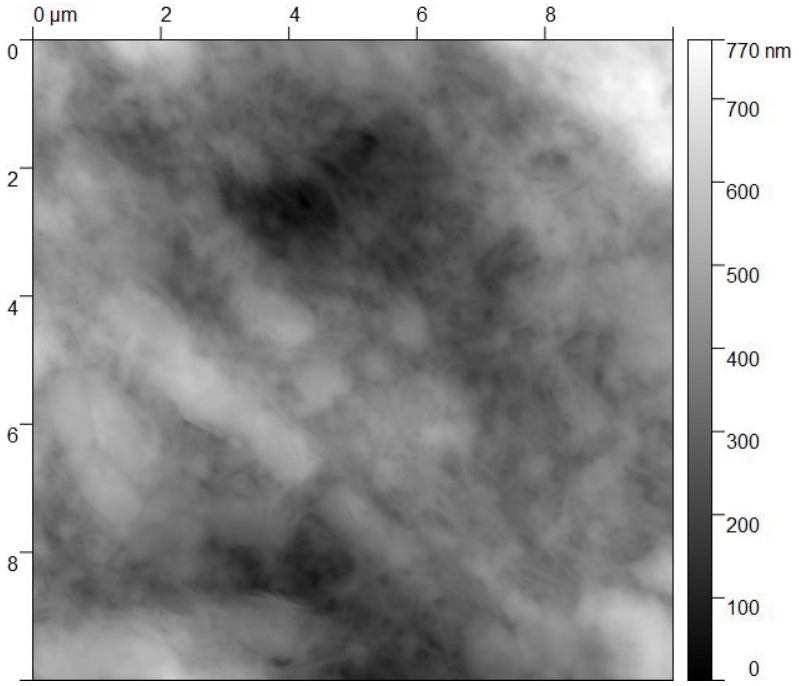

Figure B.22: 10 μm by 10 μm scan of Bacterial cellulose functionalised with 500μg/mL BslA without CBM.

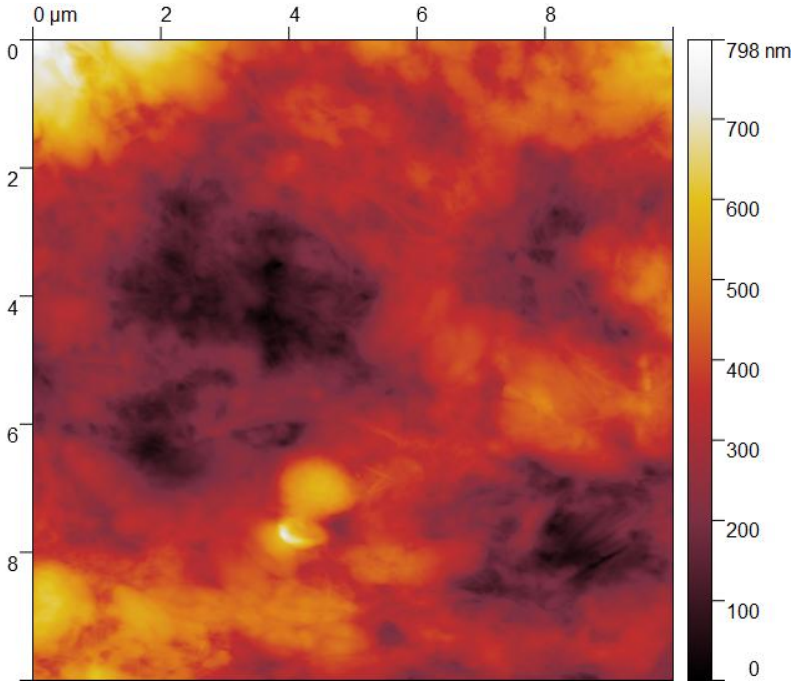

Figure B.23: 10 μm by 10 μm scan of Bacterial cellulose functionalised with 500μg/mL BslA without CBM.

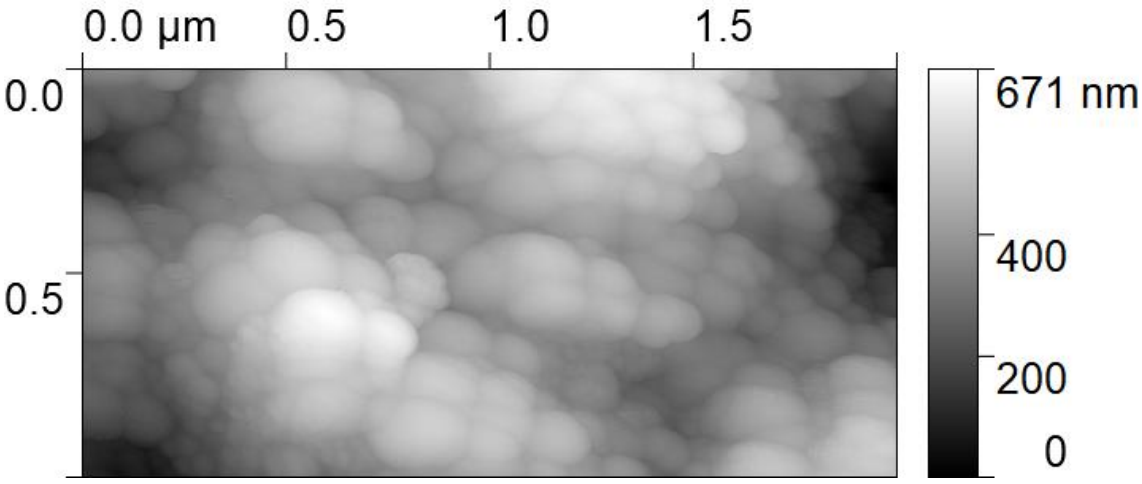

Figure B.24: Topography of 40nm silica micro-particles taken over an area of; a) 2μm by 1μm and b) 10μm by 5μm.

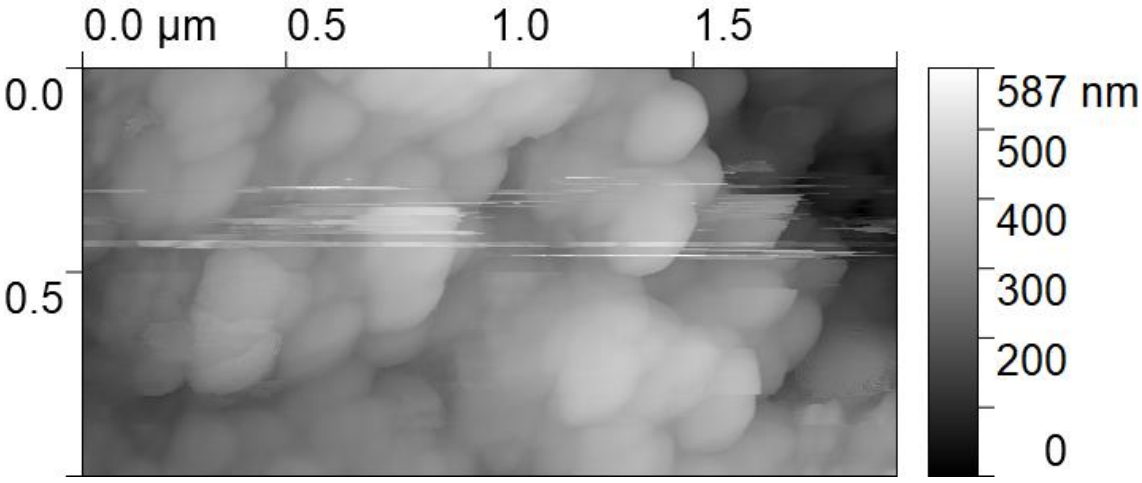

Figure B.25: Topography of 20nm silica micro-particles images taken over an area of; a) 2μm by 1μm and b) 10μm by 5μm.

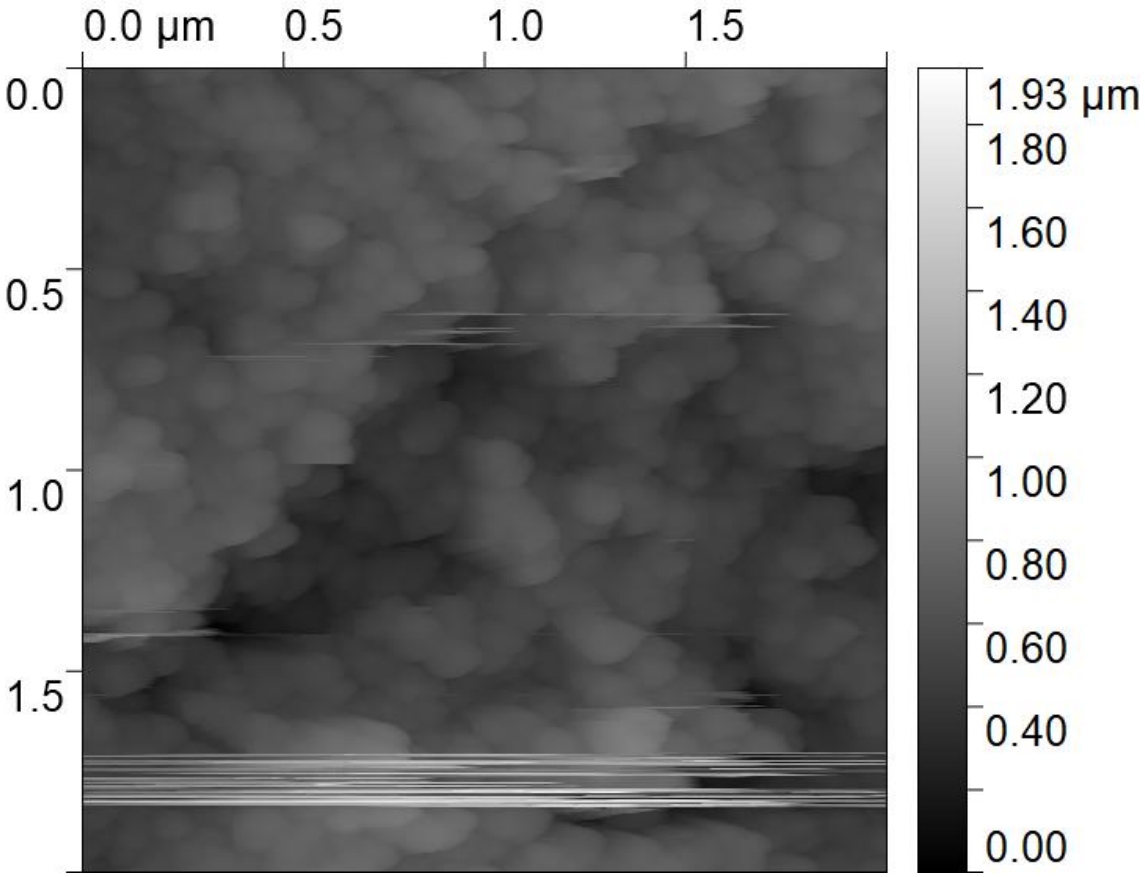

(a)

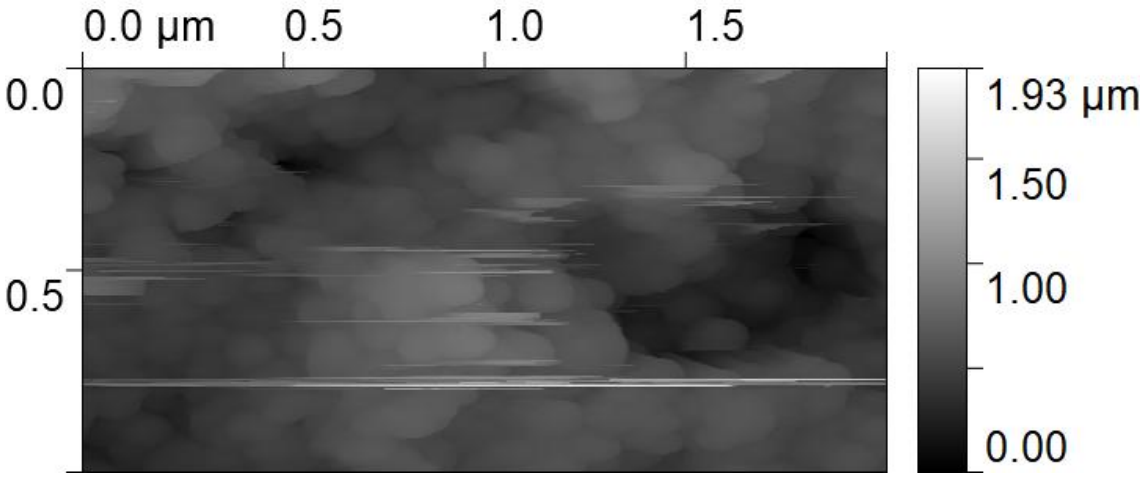

(b)

Figure B.26: Topographic of 4.5μm micro-particles with 20nm nanoparticles on the surface of the micro-particles silica images taken over an area of; a) 2μm by 2μm and b) 2μm by 1μm

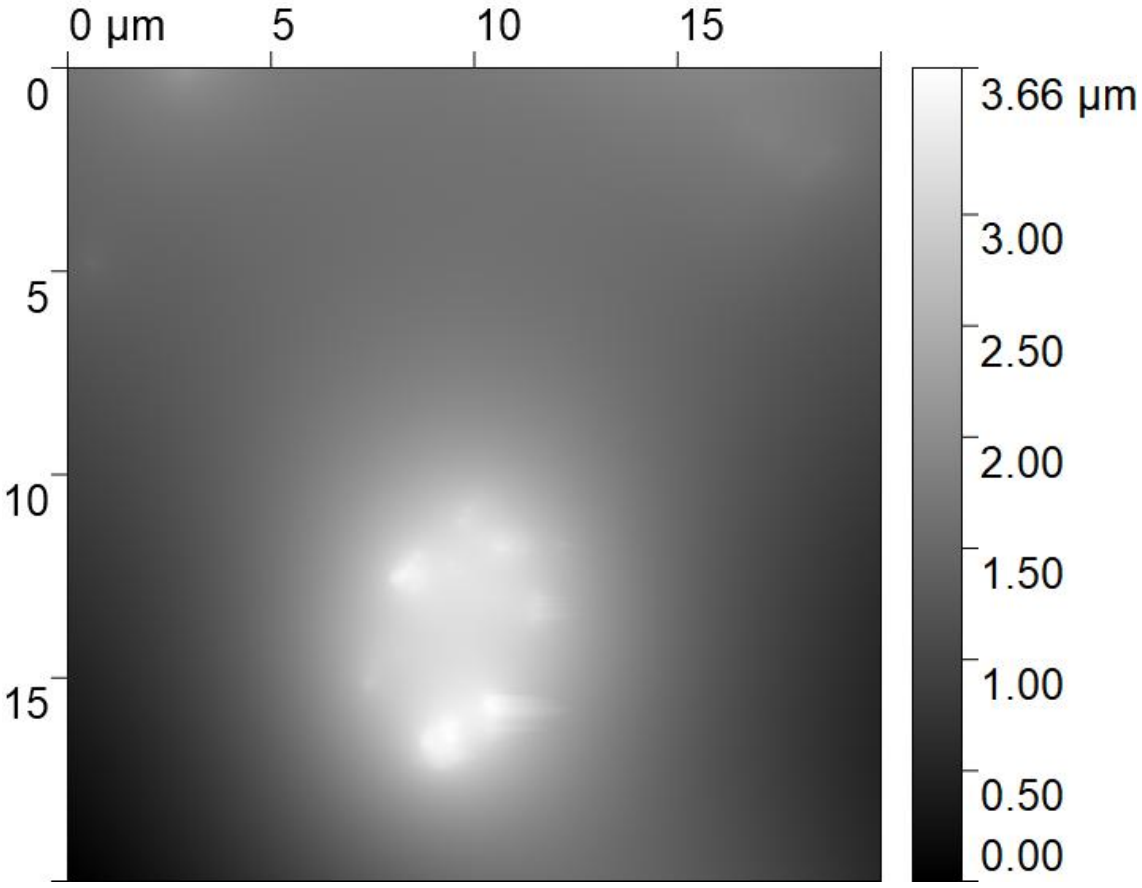

Figure B.27: Scan of a 40/60 mix of Silica micro-particles with a PDMS covering, with scan size of 20μm by 20μm

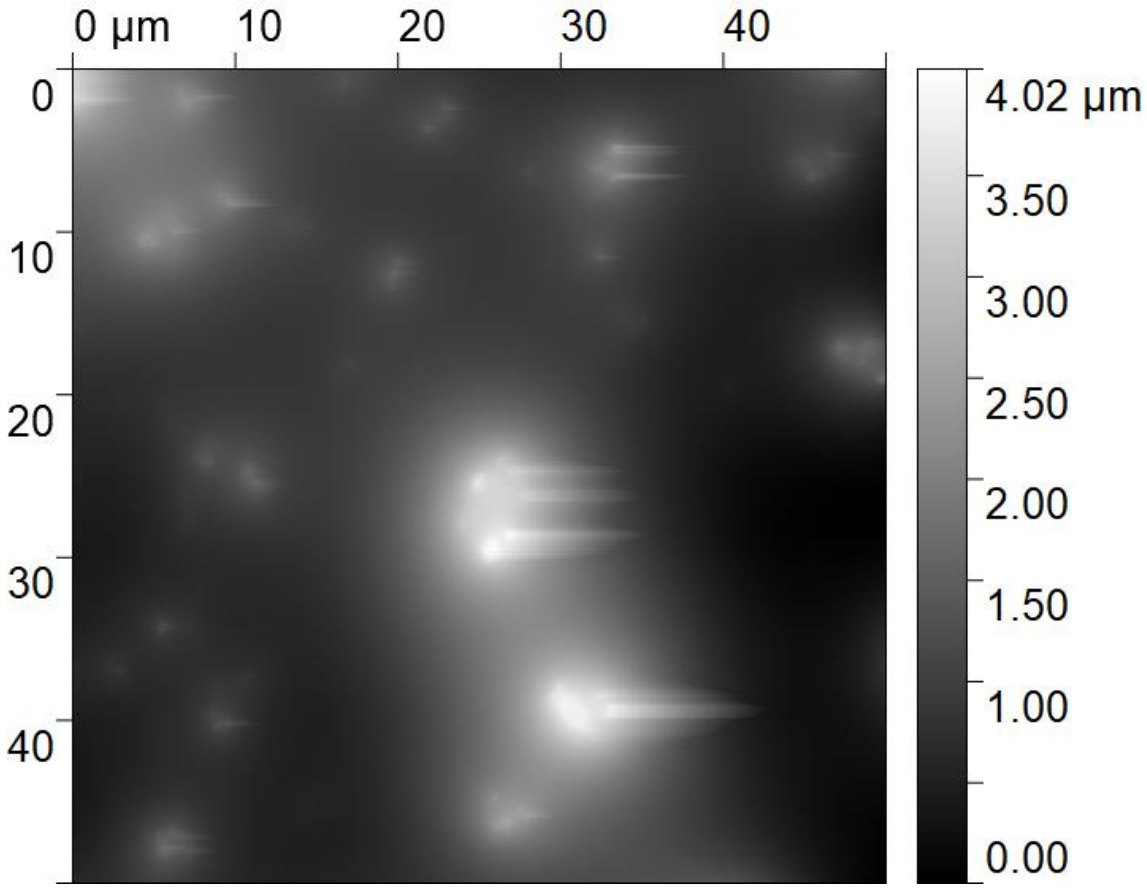

(a)

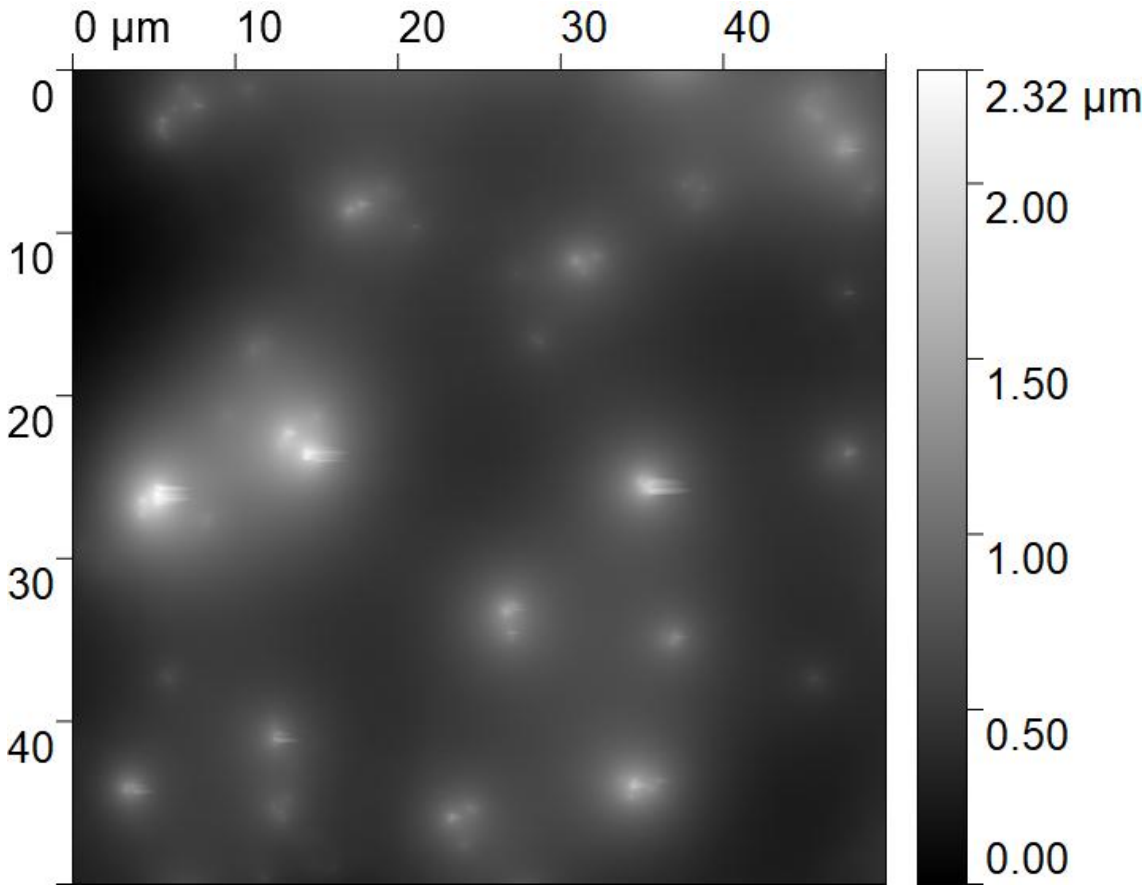

(b)

Figure B.28: Scan of a 60/40 mix of Silica micro-particles with a PDMS covering, with scan sizes of; a) 50μm by 50μm b) 50μm by 50μm.

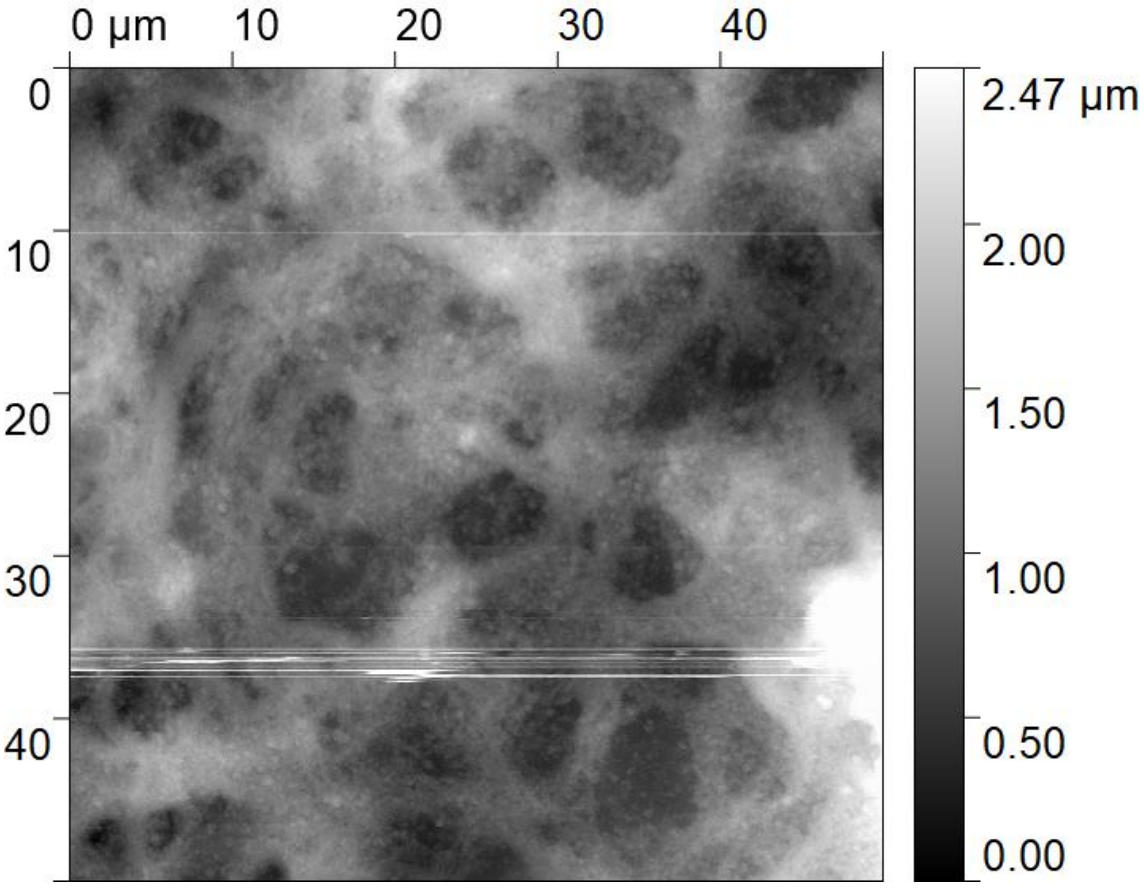

Figure B.29: Scan of 4.5μm silica micro-particles coated with PDMS and 7nm silica nano-particles over areas of 50μm by 50μm

References

Agostini, M. and Collins, D. (2018), 'Surface-Acoustic-Wave (SAW)-Driven Device for Dynamic Cell Cultures'.

Alibert, C., Goud, B. and Manneville, J. B. (2017), 'Are cancer cells really softer than normal cells?', *Biology of the Cell* **109**(5), 167–189.

Bainbridge, P. (2013), 'Wound healing and the role of fibroblasts', *Journal of wound care* **22**(8), 407–412.

Bélanger, M. C. and Marois, Y. (2001), 'Hemocompatibility, biocompatibility, inflammatory and in vivo studies of primary reference materials low-density polyethylene and polydimethylsiloxane: A review', *Journal of Biomedical Materials Research* **58**(5), 467–477.

Binnig, G., Quate, C. F. and Gerber, C. (1986), 'Atomic force microscope', *Physical Review Letters* **56**(9), 930–933.

Biroun, M. H., Li, J., Tao, R., Rahmati, M., McHale, G., Dong, L., Jangi, M., Torun, H. and Fu, Y. Q. (2020*a*), 'Acoustic waves for active reduction of contact time in droplet impact', *Physical Review Applied* **14**(2), 024029.

Biroun, M. H., Li, J., Tao, R., Rahmati, M., McHale, G., Dong, L., Jangi, M., Torun, H. and Fu, Y. Q. (2020*b*), 'Acoustic waves for active reduction of contact time in droplet impact', *Physical Review Applied* **14**(2), 024029.

Bradford, M. M. (1976), 'A rapid and sensitive method for the quantitation of microgram quantities of protein utilizing the principle of protein-dye binding', *Analytical Biochemistry* **72**(1-2), 248–254.

Brown, A. J. (1886), 'XIX.—The chemical action of pure cultivations of bacterium aceti', *Journal of the Chemical Society, Transactions* **49**(0), 172–187.

Browning, G. (2022), 'num2clip: copy numerical arrays to clipboard - File Exchange - MATLAB Central'.
URL: https://www.mathworks.com/matlabcentral/fileexchange/8472-num2clip-copy-numerical-arrays-to-clipboard

Budhiono, A., Rosidi, B., Taher, H. and Iguchi, M. (1999), 'Kinetic aspects of bacterial cellulose formation in nata-de-coco culture system', *Carbohydrate Polymers* **40**(2), 137–143.

Chang, L. W., Deng, W. P., Yeong, E. K., Wu, C. Y. and Yeh, S. W. (2008), 'Pressure effects on the growth of human scar fibroblasts', *Journal of Burn Care and Research* **29**(5), 835–841.

Chawla, P. R., Bajaj, I. B., Survase, S. A. and Singhal, R. S. (2009), 'Microbial cellulose: Fermentative production and applications', *Food Technology and Biotechnology* **47**(2), 107–124.

Chen, C., Bai, X., Ding, Y. and Lee, I. S. (2019), 'Electrical stimulation as a novel tool for regulating cell behavior in tissue engineering', *Biomaterials Research* **23**(1), 1–12.

Cherng, J. H., Chou, S. C., Chen, C. L., Wang, Y. W., Chang, S. J., Fan, G. Y., Leung, F. S. and Meng, E. (2021), 'Bacterial Cellulose as a Potential Bio-Scaffold for Effective Re-Epithelialization Therapy', *Pharmaceutics* **13**(10).

Cleveland, J. P., Manne, S., Bocek, D. and Hansma, P. K. (1993), 'A nondestructive method for determining the spring constant of cantilevers for scanning force microscopy', *Review of Scientific Instruments* **64**(2), 403–405.

Collins, D. J., Morahan, B., Garcia-Bustos, J., Doerig, C., Plebanski, M. and Neild, A. (2015), 'Two-dimensional single-cell patterning with one cell per well driven by surface acoustic waves', *Nature Communications 2015 6:1* **6**(1), 1–11.

Cross, S. E., Jin, Y. S., Rao, J. and Gimzewski, J. K. (2007), 'Nanomechanical analysis of cells from cancer patients', *Nature Nanotechnology* **2**(12), 780–783.

Cross, S. E., Jin, Y. S., Tondre, J., Wong, R., Rao, J. Y. and Gimzewski, J. K. (2008), 'AFM-based analysis of human metastatic cancer cells', *Nanotechnology* .

Da Silva, C. M., Bottene, M. K., De Oliveira Barud, H. G., Da Silva Barud, H., Ligabue, R. A. and Jahno, V. D. (2015), 'Wettability and Morphological Characterization of a Polymeric Bacterial Cellulose / corn Starch Membrane', *Materials Research* **18**, 109–113.

Dawson, F., Yew, W. C., Orme, B., Markwell, C., Ledesma-Aguilar, R., Perry, J. J., Shortman, I. M., Smith, D., Torun, H., Wells, G. and Unthank, M. G. (2022), 'Self-Assembled, Hierarchical Structured Surfaces for Applications in (Super)hydrophobic Antiviral Coatings', *Langmuir* .

Derjaguin, B. V., Muller, V. M. and Toporov, Y. P. (1975), 'Effect of contact deformations on the adhesion of particles', *Journal of Colloid And Interface Science* **53**(2), 314–326.

Ding, X., Lin, S. C. S., Lapsley, M. I., Li, S., Guo, X., Chan, C. Y., Chiang, I. K., Wang, L., McCoy, J. P. and Huang, T. J. (2012), 'Standing surface acoustic wave (SSAW) based multichannel cell sorting', *Lab on a Chip* **12**(21), 4228–4231.

Fu, Y. Q., Luo, J. K., Du, X. Y., Flewitt, A. J., Li, Y., Markx, G. H., Walton, A. J. and Milne, W. I. (2010), 'Sensors and Actuators B : Chemical Recent developments on ZnO films for acoustic wave based bio-sensing and microfluidic applications : a review', **143**, 606–619.

Fu, Y. Q., Luo, J. K., Nguyen, N. T., Walton, A. J., Flewitt, A. J., Zu, X. T., Li, Y., McHale, G., Matthews, A., Iborra, E., Du, H. and Milne, W. I. (2017), 'Advances in piezoelectric thin films for acoustic biosensors, acoustofluidics and lab-on-chip applications'.

Garcia, P. D. and Garcia, R. (2018), 'Determination of the viscoelastic properties of a single cell cultured on a rigid support by force microscopy', *Nanoscale* **10**(42), 19799–19809.

Gates, R. S. and Reitsma, M. G. (2007), 'Precise atomic force microscope cantilever spring constant calibration using a reference cantilever array', *Review of Scientific Instruments* **78**(8), 086101.

Gil-Redondo, J. C., Weber, A., Zbiral, B., d.M. Vivanco, M. and Toca-Herrera, J. L. (2022), 'Substrate stiffness modulates the viscoelastic properties of MCF-7 cells', *Journal of the Mechanical Behavior of Biomedical Materials* **125**, 104979.

Gilmour, K. A., Aljannat, M., Markwell, C., James, P., Scott, J., Jiang, Y., Torun, H., Dade-Robertson, M. and Zhang, M. (2023), 'Biofilm inspired fabrication of functional bacterial cellulose through ex-situ and in-situ approaches', *Carbohydrate Polymers* **304**, 120482.

Gorgieva, S. and Trček, J. (2019), 'Bacterial Cellulose: Production, Modification and Perspectives in Biomedical Applications', *Nanomaterials* **9**(10).

Guan, D., Charlaix, E., Qi, R. Z. and Tong, P. (2017), 'Noncontact Viscoelastic Imaging of Living Cells Using a Long-Needle Atomic Force Microscope with Dual-Frequency Modulation', *Physical Review Applied* **8**(4), 044010.

Guttenberg, Z., Müller, H., Habermüller, H., Geisbauer, A., Pipper, J., Felbel, J., Kielpinski, M., Scriba, J. and Wixforth, A. (2005), 'Planar chip device for PCR and hybridization with surface acoustic wave pump', *Lab on a Chip* **5**(3), 308–317.

Hansma, P. K., Cleveland, J. P., Radmacher, M., Walters, D. A., Hillner, P. E., Bezanilla, M., Fritz, M., Vie, D., Hansma, H. G., Prater, C. B., Massie, J., Fukunaga, L., Gurley, J. and Elings, V. (1994), 'Tapping mode atomic force microscopy in liquids', *Applied Physics Letters* **64**(13), 1738–1740.

Hartmann, U. (1999), 'MAGNETIC FORCE MICROSCOPY', *Annual Review of Materials Science* **29**(1), 53–87.

Hertz, H. (1896), *Miscellaneous Papers*, Macmillan and Co., LTD.

Hsieh, Y. L. (2007), 'Chemical structure and properties of cotton', *Cotton: Science and Technology* pp. 3–34.

Hughes, M. L. and Dougan, L. (2016), 'The physics of pulling polyproteins: A review of single molecule force spectroscopy using the AFM to study protein unfolding', *Reports on Progress in Physics* **79**(7), 076601.

Hutter, J. L. and Bechhoefer, J. (1993), 'Calibration of atomic-force microscope tips', *Review of Scientific Instruments* **64**(7), 1868–1873.

Janovjak, H., Struckmeier, J. and Müller, D. J. (2004), 'Hydrodynamic effects in fast AFM single-molecule force measurements', *European Biophysics Journal 2004 34:1* **34**(1), 91–96.

Johnson, K., Kendall, K. and Roberts, A. (1971), 'Surface Energy and the Contact of Elastic Solids', *Proceedings of the Royal Society of London A: Mathematical, Physical and Engineering Sciences* **324**(1558), 301–313.

Kendall, R. T. and Feghali-Bostwick, C. A. (2014), 'Fibroblasts in fibrosis: Novel roles and mediators', *Frontiers in Pharmacology* **5 MAY**, 123.

Kim, S., Nam, H., Cha, B., Park, J., Sung, H. J. and Jeon, J. S. (2022), 'Acoustofluidic Stimulation of Functional Immune Cells in a Microreactor', *Advanced Science* p. 2105809.

Kordas, A., Papadakis, G., Milioni, D., Champ, J., Descroix, S. and Gizeli, E. (2016), 'Rapid Salmonella detection using an acoustic wave device combined with the RCA isothermal DNA amplification method', *Sensing and Bio-Sensing Research* **11**(1), 121–127.

Krieg, M., Fläschner, G., Alsteens, D., Gaub, B. M., Roos, W. H., Wuite, G. J. L., Gaub, H. E., Gerber, C., Dufrêne, Y. F. and Müller, D. J. (2018), 'Atomic force microscopy-based mechanobiology', *Nature Reviews Physics* **1**(1), 41–57.

Krishnamurthy, M., Lobo, N. P. and Samanta, D. (2020), 'Improved Hydrophobicity of a Bacterial Cellulose Surface: Click Chemistry in Action', *ACS Biomaterials Science and Engineering* **6**(2), 879–888.

Kuang, R., Wang, Z., Xu, Q., Liu, S. and Zhang, W. (2015), 'Influence of mechanical stimulation on human dermal fibroblasts derived from different body sites.', *International journal of clinical and experimental medicine* **8**(5), 7641–7647.

Kubiczkova, L., Sedlarikova, L., Hajek, R. and Sevcikova, S. (2012), 'TGF-β - an excellent servant but a bad master', *Journal of Translational Medicine* **10**(1), 1–24.

Laavanya, D., Shirkole, S. and Balasubramanian, P. (2021), 'Current challenges, applications and future perspectives of SCOBY cellulose of Kombucha fermentation', *Journal of Cleaner Production* **295**, 126454.

Li, J., Xu, N., Dong, L., Li, J., Biroun, M. H., Tao, R., Torun, H., Xu, N., Rahmati, M., Li, Y., Fu, Y., Tao, R., Fu, C., Luo, J., Wang, Y., Xie, J. and Gibson, D. (2020), 'Wide range of droplet jetting angles by thin-film based surface acoustic waves', *Journal of Physics D: Applied Physics* **53**(35), 355402.

Liebner, F., Pircher, N. and Rosenau, T. (2016), 'Bacterial NanoCellulose Aerogels', *Bacterial Nanocellulose: From Biotechnology to Bio-Economy* pp. 73–108.

Lyford, T. J., Millard, P. J. and Da Cunha, M. P. (2012), Cell lysisa using surface acoustic wave devices for sensor applications, *in* 'IEEE International Ultrasonics Symposium, IUS', pp. 1216–1219.

Malek, A. M., Gibbons, G. H., Dzau, V. J. and Izumo, S. (1993), 'Fluid shear stress differentially modulates expression of genes encoding basic fibroblast growth factor and platelet-derived growth factor B chain in vascular endothelium', *Journal of Clinical Investigation* **92**(4), 2013–2021.

Maramizonouz, S., Jia, C., Rahmati, M., Zheng, T., Liu, Q., Torun, H., Wu, Q. and Fu, Y. Q. (2022), 'Acoustofluidic Patterning inside Capillary Tubes Using Standing Surface Acoustic Waves', *International Journal of Mechanical Sciences* **214**, 106893.

Martin, P. (1997), Wound healing - Aiming for perfect skin regeneration, Technical Report 5309.

Meng, E., Chen, C. L., Liu, C. C., Liu, C. C., Chang, S. J., Cherng, J. H., Wang, H. H. and Wu, S. T. (2019), 'Bioapplications of Bacterial Cellulose Polymers Conjugated with Resveratrol for Epithelial Defect Regeneration', *Polymers* **11**(6).

Miranda, M. Z., Bialik, J. F., Speight, P., Dan, Q., Yeung, T., Szászi, K., Pedersen, S. F. and Kapus, A. (2017), 'TGF-β1 regulates the expression and transcriptional activity of TAZ protein via a Smad3-independent, myocardin-related transcription factor-mediated mechanism', *The Journal of Biological Chemistry* **292**(36), 14902.

Mohammed, D., Versaevel, M., Bruyère, C., Alaimo, L., Luciano, M., Vercruysse, E., Procès, A. and Gabriele, S. (2019), 'Innovative tools for mechanobiology: Unraveling outside-in and inside-out mechanotransduction'.

Murrell, M. P., Welland, M. E., O'Shea, S. J., Wong, T. M., Barnes, J. R., McKinnon, A. W., Heyns, M. and Verhaverbeke, S. (1998), 'Spatially resolved electrical measurements of SiO2 gate oxides using atomic force microscopy', *Applied Physics Letters* **62**(7), 786.

Noy, A. (2011), 'Force spectroscopy 101: How to design, perform, and analyze an AFM-based single molecule force spectroscopy experiment', *Current Opinion in Chemical Biology* **15**(5), 710–718.

Ratcliff, G. C., Erie, D. A. and Superfine, R. (1998), 'Photothermal modulation for oscillating mode atomic force microscopy in solution', *Applied Physics Letters* **72**(15), 1911–1913.

Rayleigh, J. (1885), 'On waves propagated along the plane surface of an elastic solid', *Proceedings of the London Mathematical Society* **s1-17**(1), 4–11.

Reindl, L., Shrena, I., Kenshil, S. and Peter, R. (2003), 'Wireless Measurement of Temperature Using Surface Acoustic Waves Sensors', *Proceedings of the Annual IEEE International Frequency Control Symposium* pp. 935–941.

Reinke, J. M. and Sorg, H. (2012), 'Wound Repair and Regeneration', *European Surgical Research* **49**(1), 35–43.

Rianna, C., Radmacher, M. and Kumar, S. (2020), 'Direct evidence that tumor cells soften when navigating confined spaces', *Molecular Biology of the Cell* **31**(16), 1726–1734.

Rico, F., Roca-Cusachs, P., Gavara, N., Farré, R., Rotger, M. and Navajas, D. (2005), 'Probing mechanical properties of living cells by atomic force microscopy with blunted pyramidal cantilever tips', *Physical Review E - Statistical, Nonlinear, and Soft Matter Physics* **72**(2), 1–10.

Rowell, R. M., Pettersen, R. and Tshabalala, M. A. (2012), 'Cell Wall Chemistry', *Handbook of Wood Chemistry and Wood Composites, Second Edition* pp. 33–72.

Sader, J. E., Larson, I., Mulvaney, P. and White, L. R. (1998), 'Method for the calibration of atomic force microscope cantilevers', *Review of Scientific Instruments* **66**(7), 3789.

Salehi-Reyhani, A., Gesellchen, F., Mampallil, D., Wilson, R., Reboud, J., Ces, O., Willison, K. R., Cooper, J. M. and Klug, D. R. (2015), 'Chemical-Free Lysis and Fractionation of Cells by Use of Surface Acoustic Waves for Sensitive Protein Assays', *Analytical Chemistry* **87**(4), 2161–2169.

Schwartz, M. A. (2010), 'Integrins and extracellular matrix in mechanotransduction', *Cold Spring Harbor perspectives in biology* **2**(12).

Shi, J., Ahmed, D., Mao, X., Lin, S. C. S., Lawit, A. and Huang, T. J. (2009), 'Acoustic tweezers: patterning cells and microparticles using standing surface acoustic waves (SSAW)', *Lab on a Chip* **9**(20), 2890–2895.

Sorrell, J. M. and Caplan, A. I. (2004), 'Fibroblast heterogeneity: More than skin deep'.

Strange, A. P., Aguayo, S., Ahmed, T., Mordan, N., Stratton, R., Porter, S. R., Parekh, S. and Bozec, L. (2017), 'Quantitative nanohistological investigation of scleroderma: An atomic force microscopy-based approach to disease characterization', *International Journal of Nanomedicine* **12**, 411–420.

te Riet, J., Katan, A. J., Rankl, C., Stahl, S. W., van Buul, A. M., Phang, I. Y., Gomez-Casado, A., Schön, P., Gerritsen, J. W., Cambi, A., Rowan, A. E., Vancso, G. J., Jonkheijm, P., Huskens, J., Oosterkamp, T. H., Gaub, H., Hinterdorfer, P., Figdor, C. G. and Speller, S. (2011), 'Inter-laboratory round robin on cantilever calibration for AFM force spectroscopy', *Ultramicroscopy* **111**(12), 1659–1669.

Torun, H., Agrawal, P., Markwell, C., Fu, Y., Todryk, S. and Moschos, S. A. (2023), 'Engineering Approaches for Cellular Therapeutics and Diagnostics', *Emerging Drug Delivery and Biomedical Engineering Technologies* pp. 157–169.

Vernon, J., Canyelles-Pericas, P., Torun, H., Binns, R., Ng, W. P. and Fu, Y. Q. (2021), Apnoea-Pi: Sleep disorder monitoring with open-source electronics and acoustics, *in* '2021 26th International Conference on Automation and Computing: System Intelligence through Automation and Computing, ICAC 2021', Institute of Electrical and Electronics Engineers Inc.

Vernon, J., Canyelles-Pericas, P., Torun, H., Dai, X., Ng, W. P., Binns, R., Busawon, K. and Fu, Y. Q. (2022), 'Acousto-Pi: An Opto-Acoustofluidic System Using Surface Acoustic Waves Controlled with Open-Source Electronics for Integrated In-Field Diagnostics', *IEEE Transactions on Ultrasonics, Ferroelectrics, and Frequency Control* **69**(1), 411–422.

Wixforth, A. (2003), 'Acoustically driven planar microfluidics', *Superlattices and Microstructures* **33**(5-6), 389–396.

Wu, P.-H., Aroush, D. R.-B., Asnacios, A., Chen, W.-C., Dokukin, M. E., Doss, B. L., Durand-Smet, P., Ekpenyong, A., Guck, J., Guz, N. V., Janmey, P. A., Lee, J. S. H., Moore, N. M.,

Ott, A., Poh, Y.-C., Ros, R., Sander, M., Sokolov, I., Staunton, J. R., Wang, N., Whyte, G. and Wirtz, D. (2018), 'A comparison of methods to assess cell mechanical properties', *Nature Methods* **15**(7), 491–498.

Xiang, Z., Jin, X., Liu, Q., Chen, Y., Li, J. and Lu, F. (2017), "', *Cellulose 2017 24:11* **24**(11), 5147–5156.

Xu, G., Gunson, R. N., Cooper, J. M. and Reboud, J. (2015), 'Rapid ultrasonic isothermal amplification of DNA with multiplexed melting analysis – applications in the clinical diagnosis of sexually transmitted diseases', *Chemical Communications* **51**(13), 2589–2592.

Xu, S. and Arnsdorf, M. F. (1995), 'Electrostatic force microscope for probing surface charges in aqueous solutions', *Proceedings of the National Academy of Sciences* **92**(22), 10384–10388.

Zahertar, S., Torun, H., Sun, C., Markwell, C., Dong, Y., Yang, X. and Fu, Y. (2022), 'Flexible Platform of Acoustofluidics and Metamaterials with Decoupled Resonant Frequencies', *Sensors 2022, Vol. 22, Page 4344* **22**(12), 4344.